Rock magnetic properties of uncultivated magnetotactic bacteria and paleo-redox changes across the Paleocene-Eocene boundary, New Jersey Coastal Plain

A dissertation submitted in partial fulfillment of the requirements for the degree of

Doctor of Philosophy

to the Macquarie University, Faculty of Science

Department of Environment and Geography – Environmental Science

by

Amy P. Chen

B.S., M.S., University of Minnesota, 2008

August, 2014

Summary

Magnetotactic bacteria (MTB) can biosynthesize ferrimagnetic magnetite (Fe_3O_4) and/or greigite (Fe_3S_4) nanocrystals. Their ubiquitous presence in oxygen-stratified environments makes them useful redox indicators, in addition to being major players in the biogeochemical cycling of iron and other elements. Furthermore, since the MTB magnetite and/or greigite organelles, or magnetosomes, are within the magnetic stable single-domain (SSD) size range, they are candidate carriers of stable remanent magnetization. As such, the detection of fossilized magnetosomes (magnetofossils) is of special interest. Here, at least seven uncultivated MTB morphotypes, including magnetite producers, magnetite and greigite co-producers, and greigite-only producers were collected from the chemically stratified water column of Pettaquamscutt River Estuary, Rhode Island, U.S.A. In stark contrast to putative Neogene greigite magnetofossil records, the anhysteretic remanent magnetization (ARM) coercivity spectra for greigite producing MTB are fundamentally left-skewed with a lower median, and are strikingly similar to magnetite producing MTB. The ferromagnetic resonance (FMR) spectra of uncultivated MTB are characterized by a wider empirical parameter range than cultured single-chain magnetite magnetosomes, which has important implications for magnetofossil detection by FMR. The MTB population turnover rate, once every 28.3 days, is determined for the first time in the investigated estuary. The associated magnetosome iron flux, 15.3 to 18.2 μg Fe cm^{-2} yr^{-1}, is nearly half of the reduced Fe flux in the open Black Sea. The propensity of magnetite and greigite magnetosomes to acquire gyroremanent magnetization (both static and at a high rotation rate of 95 r.p.s.) has been assessed. Compared to framboidal greigite particles that can acquire a strong gyroremanence, magnetosomes acquire significantly less. Lastly, the above newly delineated magnetofossil characteristics are used to probe the unusually magnetic Marlboro Clay at the New Jersey Coastal Plain dating to the Paleocene-Eocene boundary. Analyses of ARM coercivity spectra suggest that between 22-37% of the ARM signal can be attributed to magnetofossils, while semi-quantitative analytical microscopy as well as rotational remanent magnetization (RRM) suggest framboidal greigite as a heretofore overlooked magnetic signal carrier. The redox significance of magnetofossils is assessed by independent inorganic geochemical proxies (trace metal and iron species) as well as lipid biomarkers (gammacerane index and pristane/phytane ratio). Overall, these proxies suggest a transition toward a more reducing condition at this continental margin setting at the onset of abrupt warming with a concomitant negative carbon isotopic excursion.

I hereby certify that the work presented in this thesis has not been submitted for a higher degree to any other university or institution.

Amy P. Chen

Acknowledgements

I thank my principal supervisor, Paul Hesse, and associate supervisor, Simon George, for their patience and insistence on beating an independent researcher out of me. They provided me with the freedom and support to go after my ideas. Paul in particular took a chance on someone who he has never met all the way from the other hemisphere 3.5 years ago. I was fortunate to learn from all of my collaborators and I thank them for not turning me away when I knocked on their doors. Bruce Moskowitz has continued to be an extraordinary mentor who provides invaluable guidance and advice, both on technical aspects and life in general. Veronica Berounsky showed me the beautiful Pettaquamscutt River Estuary and provided integral assistance in sampling without which I would not have been able to carry out the work presented in this thesis. I am grateful for the opportunity to perform experiments using the magnificent RRM machine and for David Potter's willingness to share his institutional knowledge on gyromagnetism. I will remember my time working in the terrific Microscopy Unit in Macquarie University led by Debra Birch and Nicole Vella, neither has ever hesitated to devise a strategy for what I wanted to try even when completely out of the norm. I thank Mark Blackford and Greg Lumpkin for being eminently helpful with 'bug stuff.' There are too many more names to list here, but I am grateful for the discussion, inspiration, and assistance from everyone in the acknowledgement at the end of each manuscript.

Friends and families have provided unwavering encouragement and support during graduate school. Mun, who trod the East Coast with me in search of MTB during the critical summer of 2012, has been a constant source of love and strength. By asking the right probing questions, he got me out of thinking rut on numerous occasions and taught me to look at problems from the perspective of a great experimental physicist. I thank my family in Taiwan, R.O.C., Jaspar, the Barry family, Tina, Becky, and Erika for never giving up on me despite being thousands of kilometers away for years. I thank Kat for being the thoughtful and optimistic person that she is. Many friendly faces on the 5th floor of Macquarie University library have made the excruciating thesis writing process almost tolerable. Current and former hard working inhabitants of E7A 7th and 8th floor have made me feel less lonely on late nights and weekends. I thank my fellow Macquarie University Community Garden Club members and yoga teachers for keeping me sane, and Bike North members for the many

memorable cycling adventures in/around Sydney as well as for patching me up after an epic fall. Finally, I thank Nicole and Monica for being there for me when it counts.

I gratefully acknowledge financial support from iPRS, HDR fund, and PGRF from Macquarie University, the Post-cruise Special Analytical Funding from the Australian-New Zealand IODP Consortium, IRM visiting fellowship, and a dissertation fellowship from Middle Tennessee State University.

This dissertation is dedicated to the courageous, strong, and capable women who paved the way before me.

Contents

List of Figures

List of Tables

Chapter 1

Introduction

Magnetotactic bacteria (MTB) are microbial 'engineers' of exquisite iron oxide (Fe_3O_4) and iron sulphide (Fe_3S_4) nanocrystals, known as *magnetosomes*. Since the independent discovery of these microorganisms more than fifty years ago by Salvatore Bellini [2009] and Richard P. Blakemore [1975], there now exists an extensive body of works on the remarkably diverse cell shape (or morphotype), metabolism, magnetosome and flagella morphology and arrangement, non-magnetosome intracellular globule composition, and phylogeny in this collection of prokaryotes within the *Proteobacteria*, *Nitrospirae*, and *PVC* phylum [Lefèvre and Bazylinski, 2013]. What is much less well understood in MTB geomicrobiology is the extent by which these microbes participate in the biogeochemical cycling of iron, among other major elements, in nature. Their importance in this regard has long been postulated on the basis of their sheer ubiquity, having been found on all continents in habitats ranging from circumneutral freshwater to alkaline hypersaline sediment and water columns, and the fact that the synthesis of magnetosomes are only possible when iron is bio-sequestered from the environment [K. Konhauser, 1998; Bazylinski and Frankel, 2004; S. Simmons, 2006; Lefèvre and Bazylinski, 2013]. However, the quantification on how much MTB contribute to the iron cycle has not been forthcoming due to the lack of knowledge regarding MTB population turnover rate in particular, and the actual abundance of MTB and their relationship with protists that probably graze on them in general. This dissertation sets out to explore the role MTB play in the biogeochemical cycling of iron in an accessible estuarine system that can serve as an analogue and/or an entry-point to understand less- or in-accessible larger chemically stratified ocean basins, *e.g.* the Black Sea, during many past Ocean Anoxic Events, using rock magnetic tools.

A conscious decision was made at the beginning to investigate MTB from a chemically stratified water column of a natural estuary for several reasons. The stratified water column in such an estuarine system comes with two opposing gradients of dissolved oxygen and hydrogen sulfide, the latter produced by the anaerobic sulphate reducing bacteria [Bazylinski and Moskowitz, 1997]. Such an aquatic environment provides a variety of natural niches (microaerobic and sulfide-free, anaerobic to anaerobic with sulfide, *etc.*) for hosting diverse and layered MTB communities conducive to their isolation. Of particular interest, for example, are large, slow-moving MTB rods that produce greigite (Fe_3S_4) consistently found

in the sulphidic hypolimnion just below the oxic-anoxic-interface (OAI) [Bazylinski *et al*., 1995; Simmons *et al*., 2004]. This is desirable because it is not currently possible to reliably grow greigite-producing MTB in the laboratory in pure culture [Lefèvre and Bazylinski, 2013]. As such, many of their magnetic properties have remained elusive and evaluations of the applicability of fossilized magnetosomes detection methods developed on cultured magnetite (Fe_3O_4) producing MTB impossible. Furthermore, as the MTB occur in high abundance ($10^5 – 10^4$ cells mL^{-1} ; Bazylinski *et al*., 1995; S. Simmons, 2006) in the stratified water column and not in the anoxic sediment at these localities (at least seasonally and when the water column is not completely overturned), water column samples containing live MTB are not yet complicated by diagenesis. In fact, by comparing the expected magnetosome flux from the water column and that from the surface sediment, I attempted to evaluate the preservation potential of both magnetite and greigite magnetosomes in Chapter 2.

As a whole, Chapter 2 details my investigations of MTB in the stratified and euxinic Upper Pond, Pettaquamscutt River Estuary (Narragansett, Rhode Island, USA). Having failed to locate a suitable field site containing high enough MTB cell density in the water column around New South Wales, Australia after surveying four separate localities (Coffs Harbour, Manly Lagoon, Calabash Bay, and Lake Conjola), I went instead to New England, United States where much of the early MTB work was carried out (*e.g.* R. Blakemore, 1975; Heywood *et al*. 1990; DeLong *et al*. 1993; Bazylinski *et al*., 1995; S. Simmons, 2006). The pioneering work of Bazylinski *et al*. [1995] in Pettaquamscutt River Estuary documented MTB that could produce *both* magnetite and greigite, which made this an appealing sampling site in addition to having wider chemocline (~3 m) than the only other stratified estuarine water column ever sampled for rock magnetic investigation by Moskowitz *et al*. [2008] in Salt Pond, Woods Hole, Massachusetts, USA (chemocline width ~1.2 m). I showed that the coercivity distribution of magnetite and greigite producing MTB are surprisingly similar, though their ferromagnetic resonance (FMR) spectra do not look like those measured from intact cultured magnetite MTB. From an installed sediment trap, I also calculated MTB population turnover rate for the first time and estimated the MTB contribution to the reduced iron flux out of the chemocline.

Having acquired a set of samples containing wild magnetite and greigite MTB from Upper Pond, I set out to measure gyro- and rotational remanent magnetization (GRM and RRM, respectively). In recent years RRM and GRM are almost always synonymous with greigite [*e.g*. Hu *et al*. 1998, 2002; Fu *et al*. 2008; Kirschvink et al. 2008; Fabian and Frederichs, 2011; Reinholdsson *et al*. 2013], since sediment samples containing single-

domain (SD) greigite have been shown to acquire strong gyromagnetic remanences [I. Snowball, 1997; Stephenson and Snowball, 2001]. However, the mechanism by which SD greigite can acquire such a strong gyromagnetic remanence has never been fully understood, and the transverse remanent magnetization at the root of both RRM and GRM was originally associated with single-domain magnetite and maghemite particles at the inception [e.g. Stephenson 1980, 1981; Potter and Stephenson, 1986]. In Chapter 3 I present results from GRM and RRM measurements made on uncultivated MTB from Upper Pond as well as on another greigite-producing MTB, the multicellular magnetic prokaryotes (MMPs), enriched from the Little Sippewissett salt marsh. As it turned out, magnetosomes do not acquire nearly as large GRM and RRM as greigite framboids formed authigenically, likely because of the fewer stable remanent magnetization states afforded by the particle chain architecture as postulated by Potter and Stephenson [2006], the lack of strong interparticle dipolar interaction, both positive and negative, in more than one direction, and/or the presence of crystal structural defects often associatd with greigite magneosomes.

In Chapter 4, the focus was shifted toward the application of uncultivated MTB rock magnetic properties newly delineated above. An interesting case study is presented in which the unusually magnetic Paleocene-Eocene Marlboro Clay on the New Jersey Coastal Plain is reevaluated by analytical microscopy, anhysteretic remanent magnetization (ARM) spectra, and RRM. From these analyses, greigite clusters/framboids are proposed as major carriers of magnetic signal for the Marlboro Clay for the first time, while 22-37% of the total ARM can be attributed to magnetofossils.

References

Bazylinski, D.A., Frankel, R.B., Heywood, B.R., Mann, S., King, J.W., Donaghay, P.L., Hanson, A.K., 1995. Controlled Biomineralization of Magnetite (Fe_3O_4) and Greigite (Fe3S4) in a Magnetotactic Bacterium. Appl. Environ. Microb. 61, 3232–3239.

Bazylinski, D.A., Moskowitz, B.M., 1997. Microbial biomineralization of magnetic iron minerals: microbiology, magnetism and environmental significance, in: Reviews in Mineralogy. pp. 181–223.

Bazylinski, D.A., Frankel, R.B., 2004. Magnetosome formation in prokaryotes. Nat. Rev. Microb. 2, 217–230. doi:10.1038/nrmicro842

Bellini, S., 2009. On a unique behavior of freshwater bacteria. Chin. J. Oceanol. Limnol. 27, 3–5. doi:10.1007/s00343-009-0003-5

Bellini, S., 2009. Further studies on “magnetosensitive bacteria”. Chin. J. Oceanol. Limnol. 27, 6–12. doi:10.1007/s00343-009-0006-2

Blakemore, R., 1975. Magnetotactic bacteria. Science 190, 377–379. doi:10.1126/science.170679

Fabian, K., Frederichs, T., 2011. Quantifying gyroremanent magnetization in greigite-bearing sediments, in: Geophysical Research Abstracts. Presented at the EGU General Assembly.

Fu, Y., von Dobeneck, T., Franke, C., Heslop, D., Kasten, S., 2008. Rock magnetic identification and geochemical process models of greigite formation in Quaternary marine sediments from the Gulf of Mexico (IODP Hole U1319A). Earth Planet. Sci. Lett. 275, 233–245. doi:10.1016/j.epsl.2008.07.034

Heywood, B.R., Bazylinski, D.A., Garratt-Reed, A., Mann, S., Frankel, R.B., 1990. Controlled biosynthesis of greigite (Fe3S4) in magnetotactic bacteria. Naturwissenschaften 77, 536–538. doi:10.1007/BF01139266

Hu, S., Appel, E., Hoffmann, V., Schmahl, W.W., Wang, S., 1998. Gyromagnetic remanence acquired by greigite (Fe3S4) during static three-axis alternating field demagnetization: GRM acquired by greigite. Geophys. J. Int. 134, 831–842. doi:10.1046/j.1365-246x.1998.00627.x

Hu, S., Stephenson, A., Appel, E., 2002. A study of gyroremanent magnetisation (GRM) and rotational remanent magnetisation (RRM) carried by greigite from lake sediments. Geophys. J. Int. 151, 469–474. doi:10.1046/j.1365-246X.2002.01793.x

Kirschvink, J.L., Kopp, R.E., Raub, T.D., Baumgartner, C.T., Holt, J.W., 2008. Rapid, precise, and high-sensitivity acquisition of paleomagnetic and rock-magnetic data: Development of a low-noise automatic sample changing system for superconducting rock magnetometers: AUTOMATIC SAMPLE CHANGING SYSTEM. Geochemistry, Geophysics, Geosystems 9, n/a–n/a. doi:10.1029/2007GC001856

Konhauser, K.O., 1998. Diversity of bacterial iron mineralization. Earth Sci. Rev. 43, 91–121.

Lefèvre, C.T., Bazylinski, D.A., 2013. Ecology, Diversity, and Evolution of Magnetotactic Bacteria. Microbiol. Mol. Biol. Rev. 77, 497–526. doi:10.1128/MMBR.00021-13

Mann, S., Sparks, N.H.C., Frankel, R.B., Bazylinski, D.A., Jannasch, H.W., 1990. Biomineralization of ferrimagnetic greigite (Fe3S4) and iron pyrite (FeS2) in a magnetotactic bacterium. Nature 343, 258–261. doi:10.1038/343258a0

Moskowitz, B.M., Bazylinski, D.A., Egli, R., Frankel, R.B., Edwards, K.J., 2008. Magnetic properties of marine magnetotactic bacteria in a seasonally stratified coastal pond (Salt Pond, MA, USA). Geophys. J. Int. 174, 75–92. doi:10.1111/j.1365-246X.2008.03789.x

Potter, D.K., Stephenson, A., 1986. The detection of fine particles of magnetite using anhysteretic and rotational remanent magnetizations. Geophys. J. Int. 87, 569–582. doi:10.1111/j.1365-246X.1986.tb06638.x

Potter, D.K., Stephenson, A., 2006. The stable orientations of the net magnetic moment within single-domain particles: Experimental evidence for a range of stable states and implications for rock magnetism and palaeomagnetism. Phys. Earth Planet. In. 154, 337–349. doi:10.1016/j.pepi.2005.06.018

Reinholdsson, M., Snowball, I., Zillén, L., Lenz, C., Conley, D.J., 2013. Magnetic enhancement of Baltic Sea sapropels by greigite magnetofossils. Earth Planet. Sci. Lett. 366, 137–150. doi:10.1016/j.epsl.2013.01.029

Simmons, S.L., Sievert, S.M., Frankel, R.B., Bazylinski, D.A., Edwards, K.J., 2004. Spatiotemporal Distribution of Marine Magnetotactic Bacteria in a Seasonally Stratified Coastal Salt Pond. Appl. Environ. Microb. 70, 6230–6239. doi:10.1128/AEM.70.10.6230-6239.2004

Simmons, S.L., 2006. Geobiology of Marine Magnetotactic Bacteria (Ph.D. dissertation). Massachusetts Institute of Technology and the Woods Hole Oceanographic Institution.

Snowball, I.F., 1997. The detection of single-domain greigite (Fe_3S_4) using rotational remanent magnetization (RRM) and the effective gyro field (Bg): mineral magnetic and palaeomagnetic applications. Geophys. J. Int. 130, 704–716. doi:10.1111/j.1365-246X.1997.tb01865.x

Stephenson, A., 1980. A gyroremanent magnetisation in anisotropic magnetic material. Nature 284, 49–51. doi:10.1038/284049a0

Stephenson, A., 1981. Gyromagnetic remanence and anisotropy in single-domain particles, rocks, and magnetic recording tape. Philos. Mag. Part B 44, 635–664. doi:10.1080/01418638108223770

Stephenson, A., Snowball, I.F., 2001. A large gyromagnetic effect in greigite. Geophys. J. Int. 145, 570–575. doi:10.1046/j.0956-540x.2001.01434.x

Chapter 2

Magnetic properties of uncultivated magnetotactic bacteria and their contribution to a stratified estuary iron cycle

Disclaimer

An examiner of the thesis (post publication of the manuscript) asked for an explanation as to why MTB was not collected in Australia. While this would have been ideal, the localities I sampled around NSW (see Ch. 1) did not have a high enough MTB count in the water column. Given the available time and in order to avoid non-MTB magnetic components in sediment that would complicate the interpretation, I went instead to East coast USA. This, however, does not mean that MTB do not exist in Australia, see *e.g.* A. Taylor (2002).

The second interesting question was raised regarding the vertical resolution of the measured magnetic parameters. By retrieving water from the estuary, I was necessarily causing a disturbance and a displacement in the water column. To minimize it, I used an L-shaped aluminum bracket taped to the intake of a Geotech pump as described in the Methods. In theory, this should be better than taking the water without the bracket, however, it is difficult (if not impossible) to verify in this type of dynamic settings. I have some reassurance that the MTB collected correspond to discrete depth intervals, even if there exist some mixing: when I compared the hanging-drop observations of samples collected in top-down (*i.e.* collection starts at shallow depth and ends at deeper depth) versus bottom-up approach, the MTB morphological trends are remarkably similar. Moreover, because there is a clear 'switch' to the large rod MTB morphology at 6 m, the mixing interval is unlikely greater than the 20 – 30 cm sampling interval.

Another question came up about the motivation behind the filtration strategy. The motivation behind sequentially filtering with different pore sizes was the need to filter large quantities of water in order to meet the magnetometer sensitivity. By extensive trial, I found that using one 0.22 μm 47 mm-diameter filter to process more than 100-200 mL water resulted in the clogging of pore space so severely that it was not possible to filter a large

enough quantity of water in reasonable time to avoid alteration, nor to meet the rock magnetometer sensitivity. I tried also to use CellTrap™ (bundled 0.2 μm hollow fiber membrane filters) but was not able to filter more than 100 mL.

Taylor, A.P., 2002. Magnetotactic bacteria and their biominerals (Ph.D. dissertation). University of Queensland.

A.P. Chen[1], V.M. Berounsky[2], M.K. Chan[3], M.G. Blackford[4], C. Cady[5†], B.M. Moskowitz[6], P. Kraal[7], E.A. Lima[8], R.E. Kopp[9], G.R. Lumpkin[4], B.P. Weiss[8], P. Hesse[1], N.G.F. Vella[10]

Author affiliations

[1] Department of Environment & Geography, Macquarie University, North Ryde, NSW 2109, Australia

[2] Graduate School of Oceanography, University of Rhode Island, Narragansett, RI 02882, USA

[3] School of Physics & Astronomy, University of Minnesota, Minneapolis, MN 55455, USA

[4]Australian Nuclear Science and Technology Organisation, Lucas Heights, NSW 2234, Australia

[5] Department of Chemistry, Rutgers, The State University of New Jersey, New Brunswick, NJ 08901, USA

[6] Department of Earth Sciences & Institute for Rock Magnetism, University of Minnesota, Minneapolis, MN 55455, USA

[7] Department of Earth Sciences-Geochemistry, Utrecht University, Utrecht 3584, The Netherlands

[8] Department of Earth, Atmospheric, and Planetary Sciences, Massachusetts Institute of Technology, Cambridge, MA 02139, USA

[9] Department of Earth & Planetary Sciences and Rutgers Energy Institute, Rutgers University, Piscataway, NJ 08854, USA

[10] Microscopy Unit, Faculty of Science, Macquarie University, North Ryde, NSW 2109, Australia

† Present address: Department of Chemistry, University of Connecticut, Storrs, CT 06269, USA

Correspondence should be addressed to A.P.C. (email: AmyPChen012s@gmail.com).

Author contributions

A.P.C. initiated the project, collected the samples, conducted the measurements, provided the interpretations, and drafted the manuscript. V.M.B. advised and performed sample collection. M.K.C. assisted in water column sample collection, hanging-drop assay, magnetometry measurements and interpretations. M.G.B. and G.R.L. advised on and collected the EDS data. P.K. assisted in the interpretation of the MTB Fe flux results and their implications. C.C. and R.E.K. advised on and assisted in FMR data collection. E.A.L. and B.P.W. advised on and assisted in magnetometry measurements. B.M.M. and P.H. advised throughout. N.G.F.V. assisted in TEM sample preparation and image collection. Everyone participated in discussion and manuscript revision.

Accepted for publication in *Nature Communications*.

2.1 Introduction

Of the two nanocrystal (magnetosomes) compositions biosynthesized by magnetotactic bacteria (MTB), the magnetic properties of magnetite magnetosomes have been extensively studied using widely available cultures while those of greigite magnetosomes remain poorly known. Here we have collected uncultivated magnetite- and greigite-producing MTB to determine their magnetic coercivity distribution and ferromagnetic resonance (FMR) spectra, and to assess the MTB-associated iron flux. We find that, compared to magnetite-producing MTB cultures, FMR spectra of uncultivated MTB are characterized by a wider empirical parameter range, thus complicating the use of FMR for fossilized magnetosome (magnetofossil) detection. Furthermore, in stark contrast to putative Neogene greigite magnetofossil records, the coercivity distributions for greigite-producing MTB are fundamentally left-skewed with a lower median. Lastly, a comparison between the MTB-associated iron flux in the investigated estuary and the pyritic-Fe flux in the Black Sea suggests MTB play an important, but heretofore overlooked role in the euxinic marine system iron cycle.

Since the discovery of MTB fifty years ago[1,2], these microorganisms have continued to captivate the attention of geoscientists with their remarkable diversity, metabolic flexibility, magnetism, and ubiquity. The observation that chemically stratified euxinic basins host thriving populations of MTB[3-7] has led to the proposition that magnetosomes are an important component of the euxinic system iron cycle and can serve as biomarkers of past

ocean redox shifts[8-9]. The suggestion that MTB play an important role in the iron cycle stems from the fact that iron must be sequestered from the surrounding environment in order for them to biosynthesize their iron-rich organelle[6,10]. Some of the magnetosome-bound iron can be released back into the environment via ingestion and subsequent digestion of MTB by protozoans[10,11] or by dissolution with or without assistance by the iron-chelating siderophores MTB produce themselves[8,10,12-13], while the rest can be incorporated as intact magnetosomes into the sedimentary matrix. As for their relevance as a redox proxy, there are at least two possible scenarios. First, as MTB population size tends to scale with the width of the chemocline[14], sedimentary magnetofossil concentration can reflect changes in chemocline width in response to deoxygenation and recovery. Second, because greigite-producing MTB require sulfur for magnetosome biosynthesis[8], their occurrences are likely correlated with the many episodic euxinia experienced by the Earth's ocean in the geological past[15]. As such, the presence of greigite (Fe_3S_4) magnetofossils in geological records has been suggested as an indicator of euxinia[8,9,16,17].

Ascertaining the role MTB play in stratified euxinic systems' iron cycle requires knowledge of the amount and rate of magnetosome-bound iron that can be exported out of the oxic-anoxic interface (OAI), where high abundance of live MTB are found in such chemically stratified environments. The former has been estimated for one meromictic coastal salt pond[6,7], but a quantitative assessment of the latter has not been forthcoming. Furthermore, in order for magnetofossils to serve as a marker of paleo-redox conditions, there must be accurate ways of detecting them in the geological records and an understanding of how diagenesis affects their concentration in sediments. Magnetofossil detection methods employing magnetic property measurements in use today are largely based on characterizations of MTB isolated in pure culture known to produce linear chains of magnetite (Fe_3O_4) magnetosomes[18-26]. Mechanistically these methods are founded on the low-temperature crystallographic transition specific to single-magnetic-domain (SD) magnetite[18], pronounced uniaxial magnetic anisotropy that arises from the magnetosome chain architecture[20-28], and the uniformity in magnetosome size[19]. Characterized MTB cultures, however, are not representative of the diverse and naturally-occurring magnetosome geometry, crystallography, and mineralogy that can ultimately be preserved in the geological records. For example, the only greigite-producing MTB recently cultivated in the laboratory, strain BW-1, biosynthesizes either single or double chains of magnetite and/or greigite depending on hydrogen sulfide concentration and/or redox potential in the growth medium[29]. BW-1 represents just one of the two known greigite-producing MTB morphotypes and has

never been characterized by any of the magnetofossil detection methods in use today. There is also a lack of magnetic characterization on similar but uncultivated greigite-producing MTB large rods, as well as the other known greigite-producing MTB, multicellular magnetotactic prokaryote (MMP), all of which commonly produce disaggregated magnetosome clusters and bundles[3,4,30-34]. Non-chain magnetosome geometry is not restricted to greigite-producing MTB, as there have been numerous reports of uncultivated magnetite-producing MTB that do not form simple single chains[35] and whose magnetic properties remain largely unknown. As such, there are major open questions concerning the applicability of existing methods for detecting greigite magnetofossils and magnetofossils not arranged in simple single-chain.

Here we have collected uncultivated live MTB that have not yet been subjected to diagenesis from the stratified water column of Upper Pond, Pettaquamscutt River Estuary, Rhode Island, U.S.A. We report the first FMR and coercivity distribution characterizations on collections of uncultivated MTB that produce magnetite, co-produce greigite and magnetite, and only greigite. We show that uncultivated MTB are characterized by a wider range of FMR empirical spectral parameters compared to the five cultured magnetite-producing MTB strains that have been characterized to-date[20-22,25,26,37]. We also show that, compared to putative Neogene greigite magnetofossil bearing sedimentary rocks[16,38], the coercivity distributions of uncultivated MTB that produce magnetite, magnetite and greigite, or greigite only, are fundamentally left-skewed with a lower median. We consider the implications these new FMR and coercivity distribution results have on magnetofossil detection and quantification. We conclude by determining the MTB population turnover rate in Upper Pond and discuss the role MTB play in the euxinic system iron cycle.

2.2 Results

2.2.1 Layered MTB population in the water column. We collected uncultivated MTB as a function of water depth, *d*, from the Upper Pond, Pettaquamscutt River Estuary (Fig. 1). The Upper Pond (maximum depth 13.5 m, surface area 0.29 km^2) is one of two brackish basins, separated from one another by shallow sills, located in North Kingstown, Rhode Island, USA[39]. Except for the complete water column overturn that occurs every 5 to 10 years[39], the water column stratification in Upper Pond is maintained year-round mainly by the salinity contrast between its two water sources: the Gilbert Stuart Stream and the Rhode Island Sound[39]. The bottom water of both basins in the Pettaquamscutt River Estuary is depleted in dissolved oxygen (*DO*), due to aerobic heterotrophic respiration and the limited atmospheric

oxygen downward diffusion, and enriched in hydrogen sulfide (H_2S) generated by anaerobic microbial sulfate reduction[4,39,40]. In two previous studies carried out in the Lower Pond[3,4], the other brackish basin in the Pettaquamscutt River Estuary located ~1 km south of our sampling site, the highest number of live MTB were found around the oxic-anoxic-interface (OAI). Among at least seven MTB morphotypes observed in the Lower Pond[3,4], a vibrio (MV-2) and a coccus (MC-1) MTB strain were isolated in axenic culture, both of which are producers of single-chain magnetite magnetosomes[41-43]. The other observed MTB morphotypes have not been cultivated, including one that simultaneously produces magnetite and greigite magnetosomes[3,4]. The MTB population in the Lower Pond water column has a layered structure: magnetite producers are found in the microaerobic to anaerobic depth, greigite producers are found in the anaerobic and sulfidic depth, and the magnetite and greigite co-producers are found below the magnetite producers but above the greigite producers[4].

DO and *Eh* measurements (Methods) show that on the day of our sampling the water column of Upper Pond was stratified with a well-developed OAI at *d*=5.2 m and support the presence of H_2S below *d*=5.0 m (Fig. 2a). The sulfide concentration in Upper Pond has been measured directly in the past[39,40]. In the interval *d*=3.9- 7.0 m, we observe abundant live MTB, as well as some magnetically-responsive protists, directly by the hanging-drop assay (Fig. 2b-d; Methods). The assay shows a decrease in the MTB diversity and a change in MTB morphotype distribution with increasing water depth in agreement with an established MTB population structural model for euxinic basins[8]: whereas fast-swimming cocci, barbell-shaped cells, small rods, and vibroids are common in shallower microaerobic to anaerobic depths, slow-moving large rods dominate in deeper anaerobic and sulfidic depths (Fig. 2b). According to this MTB population structural model, magnetite producers inhabit the microaerobic to anaerobic zone whereas greigite producers dwell in the sulfidic hypolimnion, which is compatible with the microscopy findings of Bazylinski *et al.*[4] from the Lower Pond. This distribution of MTB is thought to be governed by the thermodynamic stability of magnetite vs greigite with respect to the *DO* and H_2S gradient[8].

Measurements of ferrimagnetic particle concentration-dependent parameters from filters containing water column particulates >0.22 μm present a broad peak bracketing the interval *d*=3.9-7.0 m (Fig. 2e; Supplementary Fig. 12, 18). Together with the negligible magnetic background from *d*=0-3.9 m (Fig. 2e; Supplementary Fig. 12, 18), where no live MTB were present as determined by the hanging-drop assay, we deduce that MTB are the principal carriers of the magnetic signal around the OAI. Using our hanging-drop assay results, the established MTB population structural model for euxinic basins described above[8],

and the findings of Bazylinski *et al.*[4] from the nearby Lower Pond, we divide the Upper Pond water column into three broad MTB zones: (1) d=3.9-5.0 m, containing diverse morphotypes of magnetite-producing MTB; (2) d=5.0-6.0 m, containing MTB producing both magnetite and greigite; and (3) d>6.0 m, containing greigite-producing MTB. We validated our demarcation by performing analytical microscopy on MTB from d=5.8 m and d=6.2 m (Fig. 3; Methods) and found excellent agreement. A bimodal distribution of *Fe/S* atomic ratios from energy dispersive x-ray characterizes magnetosomes (number of analyzed magnetosomes, n=38) in MTB from d=5.8 m, whereas *Fe/S* atomic ratios for those in MTB from d=6.2 m (n=33) are uniformly low (Fig. 3c). The high and low *Fe/S* atomic ratio particles are indicative of magnetite and greigite, respectively. The majority of magnetosomes with low *Fe/S* atomic ratio in the bacterium from d=5.8 m and all of the magnetosomes in the bacterium from d=6.2 m are approximately square to rectangular in shape (in 2D projection) and have non-uniform contrast (Supplementary Fig. 1). The greigite magnetosomes identified in the study of Bazylinski *et al.* [4] from Lower Pond were associated with rectangular morphology. Non-uniform contrast is a common feature of greigite magnetosomes[30-33]. These features are thought to reflect either irregular particle surfaces or structural defects, with the latter hypothesized to have resulted from the transformation of mackinawite or cubic FeS to greigite[30].

2.2.2 Ferromagnetic resonance. FMR spectroscopy is a non-destructive magnetofossil detection method that is sensitive to the net magnetic anisotropy resulting from factors such as particle size, shape, arrangement, composition, and magnetostatic interactions. Its utility in magnetofossil detection is based on the observation that FMR spectra of intact magnetite single-chain from cultured MTB exhibit a number of distinguishing properties: multiple low-field absorption peaks in the derivative spectra and extracted empirical parameters from the integrated spectra that fall within a small range of values[20-22,24,25,37] demarcated by the dashed lines in Fig. 4a-b: effective g-factor g_{eff}<2.12, asymmetry ratio A<1, and α<0.25. When the chains are randomly oriented and far apart, the low-field absorption peaks are related to resonance conditions satisfied by chains oriented parallel and perpendicular to the external field due to the positive uniaxial anisotropy[21,28]. The position of these peaks depends on the length of the chain: the longer the chains, the further apart the peaks become[20,44]. Both the $g_{eff} \leq 2.12$ (intrinsic g-factor for magnetite) and the low-field extended absorption, reflected in A<1, are also the result of the chain architecture[21,28]. The empirical parameter α combines measures of spectral asymmetry with the width of the absorption spectrum to estimate

specimen heterogeneity. Intact magnetite single-chain magnetosomes from MTB cultures have α<0.25 [21,22,24].

We characterize filters containing collections of uncultivated MTB from the Upper Pond water column by room-temperature FMR spectra using a Bruker EPR spectrometer operating at X-band (Methods). MTB in the Upper Pond water column as a whole are characterized by a wider range of empirical FMR parameters (0.80<A<1.31, 1.94<g_{eff}<2.17, 0.28<α< 0.34) than intact cultured magnetite MTB (Fig. 4a-b, Supplementary Table 6). In zone 1 where magnetite-producing MTB dominate we observe multiple low-field absorption peaks (Fig. 4c). The small cocci and barbell-shaped MTB cells in this zone produce short magnetosome chains (Fig. 2b, f), which explains the close peak positions. However, Fig. 4c shows that such peaks are absent from samples in zone 3 where greigite-producing large rods dwell in the stratified water column. Direct TEM observation from a greigite-producing MTB from d=6.2 m shows that the magnetosomes are close to one another and not organized in a single chain within the cell (Fig. 3b; Supplementary Fig. 1b). As such, we attribute the lack of multiple low-field peaks for spectra in zone 3 to magnetostatic interactions between magnetosomes. This interpretation is consistent with the reduced remanence ratios (χ_{ARM}/IRM) of 1.3-1.6 m m/A (Supplementary Fig. 6) and non-negligible first-order-reversal-curve (FORC) contribution in the H_u >0 space (Fig. 5, Supplementary Fig. 14) that characterize zone 3 filters. MTB with isolated single chains typically have χ_{ARM}/IRM=2.5–3.5 m m/A[18,21] and negligible FORC contribution in the H_u >0 space[26]. Magnetostatic interaction is known to produce FMR spectral broadening[22,44,45], reduced the χ_{ARM}/IRM ratio[22,46], and increase FORC contribution in the H_u >0 space[47].

2.2.3 Coercivity distribution. Magnetic coercivity distribution un-mixing is another widely employed method for determining the amount of biogenic magnetic particles in natural sediments. Previously, magnetization curves measured from 26 sediment samples having different provenances have been decomposed into multiple coercivity distribution components. Two particular coercivity distribution components characterized by small dispersion parameters were hypothesized to represent magnetofossils[19] (Fig. 6a): the so-called BS-BM (median coercivity 43.3±1.1 mT, dispersion factor 0.191±0.023), and BH-BI (median coercivity 68.9±1.1 mT, dispersion factor 0.122±0.037). We measured detailed anhysteretic remanent magnetization (*ARM*) demagnetization curves on filters containing collections of uncultivated MTB from the Upper Pond water column and modeled their coercivity spectra (Methods). The coercivity distribution spectra of uncultivated MTB at different depths in the Upper Pond have remarkably similar shapes (Fig. 6a). The majority are characterized by left-

skewed generalized Gaussian coercivity distributions with median 33.9±1.1 mT and dispersion factor 0.20±0.03 (Supplementary Table S4). This result is significant for three reasons. First, prior associations of BS-BM and BH-BI with magnetofossils remains speculative because numerical inversion of magnetization curves through which they were originally conceived[19] and continuously presumed[16,48-51] has non-unique solutions. Additionally, the coercivity distributions (characterized by skewness, median coercivity, and dispersion factor) of diverse MTB types found in nature are poorly constrained. The similarity of the Upper Pond uncultivated MTB coercivity distributions to that of BS-BM strongly suggests the latter is closely related to magnetosomes. Second, the small dispersion parameters of both BS-BM and BH-BI are thought to reflect the tightly genetically-controlled MTB biomineralization process in producing uniformly sized particles and therefore distinguishing them from non-biogenic magnetic particles[19]. Our results on collections of uncultivated MTB confirm this assertion, at least for the BS-BM component. Third, the skewed coercivity distributions that characterize uncultivated MTB point to the importance of modeling them as such, rather than symmetric distributions, so as to avoid the addition of coercivity distribution components that are not physically meaningful when quantifying the amount of magnetofossils. Both approaches are widely used[19,50-53].

2.3 Discussion

The natural variability in FMR spectra displayed by uncultivated MTB explains why magnetofossil-bearing sediment samples, including the surface sediment from Upper Pond (containing ~77% magnetofossils, see Supplementary Fig.10), do not always have spectral parameters that fall within the range defined by intact culture of magnetite-producing MTB characterized to-date. Curiously, FMR spectra from several water column filter samples present double minima in the derivative spectra on the high-field side (Fig. 4c). This feature has been reported for titanomagnetite (TM10)[44] but never before observed in uncultivated MTB even though such a feature is intrinsic to chains of magnetosomes with mixed uniaxial and magnetocrystalline anisotropy[28,44]. An overall lack of low-field absorption peaks and uniformly high-field extended asymmetry (A>1) characterize spectra from greigite-producing MTB in zone 3 (Fig. 4c). Such an asymmetry can be expected for systems dominated by a negative cubic magnetocrystalline anisotropy (<111> easy axis), which has been suggested as a probable case for greigite with aspect ratio >~0.75 (if elongated along <111>)[54]. In terms of magnetofossil detection, while the low-field absorption peaks remain a useful FMR trait in recognizing magnetite-producing MTB, our results from the water column, sediment trap, and the surface sediment suggest that deviations of FMR empirical parameters from those of

intact magnetite-producing MTB cultures characterized to date should not be inevitably taken to signify lower magnetofossil concentrations nor diagenetic alteration of MTB chains.

The Upper Pond water column coercivity distribution findings presented in this study establish an unequivocal link between coercivity component BS-BM and MTB without complication from co-occurring magnetic mineral phases in typical sedimentary mixture or diagenetic alteration. The lack of the other supposed magnetofossil coercivity component, BH-BI, in the collection of uncultivated MTB from the Upper Pond can be understood by examining the particle size distribution determined from 377 magnetosomes imaged from 21 MTB cells (*e.g.* Fig. 2f) between *d*=5.0-6.2 m (Fig. 6b). The magnetosomes are within the single-magnetic-domain size range[55,56], their width and length distributions are roughly Gaussian in shape (Supplementary Fig. 20a, b), but their aspect ratios range from 0.4 to 1.0 and skewed toward equidimensional particles (Supplementary Fig. 20c). Putative magnetosomes with aspect ratio <0.4 have been reported in the literature[55] (Fig. 6b). There are also many known contemporary MTB strains that produce magnetite magnetosomes with aspect ratio <0.4, including all of the strains in the *Nitrospirae* phylum[35]. Moreover, coercivity component BH-BI have been detected in sediment samples containing putative elongated magnetite magnetosomes[50,51]. These magnetosomes have enhanced shape anisotropy and therefore a higher coercivity[57,58]. As such, we hypothesize that it is the absence of higher aspect ratio magnetosomes in Upper Pond that explains the absence of BH-BI.

Coercivity distribution results from samples containing greigite magnetosomes in this study are in general agreement with pulse-field experiments on individual greigite MTB[57,59] and bulk coercivity of mixtures of greigite and magnetite MTB[7] (Fig. 6a). While coercivity distributions were not determined from these previous studies, the range of coercivities measured to date from all known greigite MTB, 20-35 mT, is just slightly higher than the coercivity of ~13 mT[17] of contemporary sediment containing putative greigite magnetofossil. In contrast, these values are consistently much smaller than the ~78 mT median coercivity measured from Neogene sediments inferred to contain greigite magnetofossils[16,38] (Fig. 6a). As the range of aspect ratios of magnetic particles extracted from these Neogene sediments is similar to that of uncultivated magnetosomes from Upper Pond (Fig. 6b), perhaps greigite magnetofossils are not the carrier of high coercivity magnetic signals in these sediments. Instead, the narrow dispersion of this high coercivity component, resembling that of BH-BI and attributed to controlled biomineralization[16], could be the consequence of another natural process that also produce uniformly sized greigite particles: for example, authigenic greigite

framboids (clusters) formation via sulfate reduction[60]. Another possibility is that an unidentified post-depositional chemical alteration mechanism could increase greigite magnetosome coercivity. In either case, enhanced inter-particle interaction is involved. This is evident from the downward shifted central peak and the large FORC function width along the H_u-axis measured from the Pliocene sediments claimed to host the oldest known greigite magnetofossils[16]. In contrast, the FORC diagram measured from MTB inhabiting *d*=6.6 m in Upper Pond (Fig. 5, Supplementary Fig. 14) has a non-negligible contribution in the $H_u>0$ range expected from the non-single chain arrangement of greigite magnetosomes (Fig. 3b; Supplementary Fig. 1b), but does not show a shift of the central peak. Similarly, no central peak shift was observed in FORC diagram from contemporary sediments from the Baltic Sea containing putative greigite magnetofossils[17]. Our study points to confounding interpretations of BH-BI, either signifying greigite framboids, diagenetic alteration of greigite magnetosomes, or high aspect ratio magnetosome/magnetofossils.

Through the use of an installed sediment trap, dead MTB exported out of the chemocline were collected over time. This, in conjunction with the water column ferrimagnetic particle concentration-dependent parameters shown in Fig. 2e, Supplementary Fig. 12, 18, allows us to determine a MTB population turnover rate of approximately once every 28.3 days (Methods). That is, neglecting seasonal variation, in one year, we can expect 12.9 times the MTB population living in the water column at the time of sampling to be exported out of *d*=7.0 m, the deepest depth where live MTB was observed by the hanging-drop assay and where the sediment trap was installed. This estimate is intrinsically inclusive of the MTB-protozoan interaction, as well as any dissolution that may or may not have occurred at *d*=3.9–7.0 m with or without assistance by the iron-chelating siderophores MTB produce. Given the MTB population turnover rate, the total amount of MTB Fe exported out of the chemocline is 15.3 to 18.2 μg Fe cm^{-2} yr^{-1} (Methods). This is a small fraction of the pyritic Fe flux (estimated 838 μg Fe cm^{-2} yr^{-1})[40] in this particular euxinic basin with a high riverine Fe flux. However, the Fe flux in open euxinic basins, such as the Black Sea, is controlled mainly by turbidite frequency and the amount of remobilized shelf Fe[61]. As such, the flux of reduced Fe, estimated to be only 38±28 μg Fe cm^{-2} yr^{-1} (ref. 61), is significantly smaller. Assuming a similar MTB population density, MTB-associated Fe flux could be a significant, and heretofore overlooked, component in the iron cycle in such open euxinic systems.

Lastly, besides being an important component in the water column Fe cycle, MTB-associated Fe is also an important component of the sediment Fe cycle and sedimentary

magnetic signal. From the MTB population turnover rate and the *ARM* profile from the water column, the contribution from MTB to the surface sediment magnetic signal in one year, assuming none of the exported magnetosomes are altered by diagenesis, is 8.15×10^{-4} Am^2 m^{-2} yr^{-1} (Methods). A simple comparison between this expected signal and the fraction of surface sediment *ARM* carried by magnetosomes deduced from coercivity component analysis, accounting for accumulation rate, 3.45×10^{-4} Am^2 m^{-2} yr^{-1}, show that up to 42% of magnetosomes exported out of the chemocline remain in the surface sediment after 12.5 years of exposure to sulfidic water (Methods). Further, if all zone 1 and 50% of zone 2 magnetosomes are magnetite in composition and all zone 3 and the other 50% of zone 2 magnetosomes are greigite in composition, then of the 42% of magnetosomes that are preserved, 44-94% can be magnetite and 6-56% can be greigite, (Methods). Our analysis demonstrates that magnetosomes can be preserved in euxinic basin sediments that had been immersed in sulfidic water for a short term, which is a prerequisite if they are to be used as biomarkers of ancient euxinia. Further studies are required to understand the longer term preservation potential and diagenetic alteration pathway, though a previous study on the nearby Lower Pond sediment does show substantially retained bulk *ARM*, carrier unknown, dating as far back as 1600 A.D.[62]. Employing similar approaches to the one we have presented in this study to investigate other stratified euxinic and ferruginous systems will allow for more robust interpretation of sedimentary magnetic signal that reflect the property of diverse and naturally occurring MTB, and can lead to better understanding of their contribution to the biogeochemical cycling of iron and other important elements.

2.4 Methods

2.4.1 Water column profile and sample collection. From an anchored boat, *DO* and *Eh* were monitored on September 15, 2012 by a calibrated YSI556 electrode. Winkler titration independently confirmed negligible *DO* from several discrete water depths with DO below YSI556 detection limit. For the water collection, the intake of a Geotech pump was taped to a L-shaped aluminum bracket covered by electrical tape, which was fixed to the YSI556 electrode. Water from each sampling depth was collected into one 2 L plastic bottle and one 250 mL bottle filled to their maximum capacity at the rate of ~3 minutes per litre. The bottles were kept in coolers with ice during the ~2 hr transit between the sampling site and the lab.

A simple sediment trap was installed in the Upper Pond water column for ~10 days (September 14-24, 2012; Supplementary Fig. 2). In each of the two plastic trap cylinders, inner diameter 2.75” (6.985 cm), the estuary surface water was used to fill the cylinders up to

a pre-marked level, such that when 1 L of saturated NaCl solution (to provide density contrast) with 1 g $HgCl_2$ (to retard cell degradation) was placed in the cylinder from the bottom using a clear vinyl tubing with a plastic funnel attached, the cylinders were filled to the top. The sediment trap was suspended at *d*=7.0 m (the deepest depth by which a preliminary survey on September 3, 2012 showed the presence of magnetotactic bacteria and magnetically-responsive protists). The sediment trap was held up-right by one subsurface buoy and one surface buoy and moored.

Surface sediment samples were obtained by an Ekman dredge lowered from an anchored boat. Retrieved sediment was frozen within two hours of collection, freeze-dried, and placed in a tightly sealed container until measurement.

2.4.2 Live cell hanging-drop assay. For the observation of MTB morphotypes, hanging-drop assay, as described in ref. 35 and illustrated in Supplementary Fig. 3, was performed on water sample collected in the 2 L bottles at every depth. One representative 20 µL droplet was taken from gently shaken bottles. The south pole of a bar magnet was placed at one side of the droplet on a Zeiss Scope A1 compound microscope stage. Images were taken with a digital camera attached to the microscope at 100x magnification.

2.4.3 Filtration and sample sets. After hanging drop assay, three sets of samples were prepared by "dead end" vacuum filtration (Supplementary Fig. 4a). One set of samples intended for remanent magnetization measurements was prepared from filtering 1 L of water from each depth sequentially through four 47 mm diameter filters with pore size 0.8-8 µm (glass fiber pre-filter), 1.2 µm, 0.45 µm, and 0.22 µm. A second set of samples intended for hysteresis and ferromagnetic resonance (FMR) measurements was prepared by filtering 250 mL of water from each depth through one 47 mm diameter filter with pore size 0.22 µm. The third set of sample intended for FORC measurements was prepared by filtering 440 mL of water taken from *d*=6.6 m through one 47 mm filter with pore size 0.22 µm. To minimize oxidation, all filters were frozen immediately, freeze-dried within a day, and sealed with a store-bought vacuum food saver along with desiccant until measurements and between measurements.

Upon retrieval of the sediment trap, the bottom-most 1 L in the sediment trap was removed from a bottom valve on the sediment trap cylinders. The rest of the water in the cylinder appeared clear with little suspended material compared to the collected fraction. The collected water was transported on ice (~2-hr transit time), centrifuged at 4 ^{0}C for 45 minutes at 8500 rpm. Approximately 99% of supernatant was filtered first through a glass fiber pre-

filter (47 mm diameter, pore size 0.8- 8 μm), while ~10 mL of the supernatant and deionized (DI) water was used to re-suspend the precipitate ("pellet"), which were then also filtered through the glass fiber pre-filter. All filtrate from the glass fiber pre-filter was then passed through three 47 mm filters with pore size 1.2 μm, 0.45 μm, 0.22 μm. Again, to minimize oxidation, all filters were frozen immediately and freeze-dried within a day, sealed with a store-bought vacuum food saver along with desiccants until and between measurements.

2.4.4 Remanent magnetization and coercivity distribution. From the first sample set, four filters from each water column depth and four filters from the sediment trap were folded and tightly placed in plastic paleomagnetic cubes. To evaluate the background signal, a "blank sample" was constructed from four un-used filters, pore size 0.8- 8 μm, 1.2 μm, 0.45 μm, 0.22 μm. *ARM* and *IRM* were measured with a SQUID rock magnetometer (2G Corp. SRM) fitted with an inline alternating-field degausser and *DC* magnetizer in the Massachusetts Institute of Technology, Paleomagnetic Laboratory. *ARM* was acquired with AF_{max}=200 mT, *DC*=0.1 mT, while *IRM* was imparted with *DC*=200 mT, both along a single-axis. *AF* demagnetization of *ARM* (along the same single-axis) was measured at 98-log-spaced steps between 0 mT to 200 mT by an automated measurement sequence, i.e. elapsed time between demagnetization steps stayed constant for all samples. *ARM* susceptibility (χ_{ARM}) was calculated from the intensity of *ARM* normalized by the *DC* biasing field. The sample-to-blank ratios (*S/B*) for *ARM* (*AF*=0) and *IRM* are shown in Supplementary Fig. 5. The signal from the blank sample was subtracted from the bulk *ARM* and *IRM* data before they are presented as filtered-water-volume-normalized magnetic moment (Fig. 2e), and χ_{ARM}/IRM ratio (Supplementary Fig. 6). The coercivity distribution was calculated from *ARM AF* demagnetization curves using CODICA and modeled using a flexible generalized skewed Gaussian function by GECA (ref. 53; Supplementary Methods).

2.4.5 Hysteresis and FORC. Filters from the second (all depths) and third (*d*=6.6 m) sample sets were folded in half, with the two halves glued together by a small amount of Elmer's glue. A ceramic knife was used to cut half (containing >0.22 μm particulate fraction from 125 mL for each water depth) or ¾ (containing >0.22 μm particulate fraction from 330 mL for *d*=6.6 m) of the filter into 4.5 to 5.5 mm squares, which were then stacked and glued together and allowed to dry in air completely (Supplementary Fig. 4b). A blank sample was constructed the same way with a new 0.22 μm filter. For the sediment trap sample, the four filters in the paleomagnetic cube for remanent magnetization were unfolded, and 1/8 of each filter (or the equivalent of particulate accumulated over 1.25 days) were also cut into 4.5 mm squares and glued together. Hysteresis loops (3 to 6 replicates) for the water column (second

set) and sediment trap filters were made with an alternating gradient force magnetometer (AGFM) at Princeton Measurement Corp. (PMC), Princeton, New Jersey. Specimen anisotropy was checked by hysteresis loop measurements made on 'filter stacks' with the filter paper plane oriented parallel and perpendicular to the applied field. The similarity between the hysteresis loops measured from these two orientations indicates very small specimen anisotropy as expected from the "dead end" filtration method (Supplementary Fig. 11, 4a). Five sets of FORC from d=6.6 m were collected from the third filter sample set and measured with a AGFM at the Institute for Rock Magnetism, University of Minnesota.

Both AGFM and VSM were calibrated by a standard daily. For AGFM measurements, each sample was auto-tuned in a 500 mT applied field. For better temporal stability, a mechanical gain of 2 was specified, and the higher of the two operating frequency choices offered by the instrument control software (MicroMag) was used. Hysteresis and FORC parameters used to collect the data are listed in Supplementary Table 3.

The measured hysteresis loops and estimates of saturation magnetization (Ms) for all samples were obtained after correction for the diamagnetic slope at high field as described in ref. 63. Supplementary Table 4 summarizes Ms and signal-to-noise (s/n) ratio for the ferromagnetic hysteresis component averaged from repeated measurements. The hysteresis loop measured from an un-used 0.22 μm filter has unreasonable negative Ms after correction due to its weak signal, so no blank subtraction was performed on filter samples. Ms as a function of water depth is shown in Supplementary Fig. 12.

Five sets of FORC acquired with identical experimental parameters on the filter sample from d=6.6 m were averaged and processed by FORCinel version 2.01[64] by both equally spaced smoothing grid and a variable smoothing grid described in ref. 26. For the former, the choice of the tricube weighted loess smoothing factor (SF) was determined by inspecting the SF vs. standard deviation of the residual (SDR) and SF vs. 1st derivative of SDR between the (averaged) measured data and the smoothed FORC data (Supplementary Fig. 13). SF=15 was the optimum value determined by the software from such residual analyses (for SF=3-15 in step of 1), and the corresponding FORC diagram is shown in Supplementary Fig. 14. For the variable smoothing grid, we used S_c=15, $S_{b,0}$=10, $S_{b,1}$=15, λ_H=0.1 (see ref. 26 for parameter definition).

2.4.6 FMR. From the second sample set, the same stack of 5 mm squares samples from a few depths used for hysteresis measurements were re-used for FMR, while 4.5 mm squares were cut from the other half of the 47 mm filters from the second sample set for others. For

the sediment trap measurements, the sample for hysteresis measurement was cut in half (~1/16 of original specimen, equivalent to particulate accumulated over 0.625 days). 0.1303 g of surface sediment was used for the FMR measurement. The FMR measurements were made at X-band with a Bruker EPR Spectrometer (Elexsys E580) in the Department of Chemistry, Rutgers, The State University of New Jersey. Except for the surface sediment sample that was measured in a dedicated EPR tube (Wilmad 710-SQ-250M), the stacked filters shared a EPR tube (Wilmad 748-PQ-7) and were swapped in and out of the tube between measurements throughout the experiment. Microwave absorption was measured as a function of applied field. Between 2 to 4 scans were performed per sample (parameters are summarized in Supplementary Table 5), with periodic re-measurement of empty EPR tube to check for possible contamination.

The blank sample, constructed from an un-used 0.22 μm filter and Elmer's glue in the same manner as for the water column and sediment trap samples contain trace amounts of ferromagnetic material, attested by its similar total FMR absorption as an empty EPR tube (Supplementary Fig. 15a). Repeated measurements of empty EPR tube throughout the experiment suggest that contamination of the tube is negligible (Supplementary Fig. 15a,b). The FMR absorption spectra were processed as follows (in order): (1) the blank signal was subtracted from the raw data, (2) drift was corrected (Supplementary Fig. 16, 17a), and (3) high frequency paramagnetic peaks were removed by Fast Fourier Transform (FFT) smoothing (Supplementary Fig. 17a). The blank signal subtraction was performed in order, i.e. samples measured after t=0 and before t=1 were subtracted by blank measured at t=0, which denotes the start of the experiment. The drift correction was performed by subtracting the FMR absorption by a baseline fitted with data from 10.6-11.1 mT and 608.8-609.4 mT. The FFT smoothing was performed by removing data with frequencies above 0.01 to 0.96 times the mean frequency of the discrete Fourier transformed FMR absorption data. Examples are given in Supplementary Figure 17b, c. Total FMR absorption obtained from processed spectra as a function of water depth is presented in Supplementary Figure 18. Empirical parameters used to characterize FMR spectra were calculated from the final FFT smoothed field vs. absorption data following the approach in ref. 20–22 and graphically illustrated in Supplementary Fig. 19. The results are summarized in Supplementary Table 6 for all samples except for the water column samples from d<3.9 m having a low sample-to-blank total absorption ratio of ~1 (Supplementary Fig. 16c).

2.4.7 Analytical microscopy. TEM samples were prepared from enriched North-seeking MTB. The cells were fixed overnight with electron microscopy-grade glutaraldehyde (final

fixative concentration 2.5%). We washed the sample several times with phosphate buffer adjusted to neutral pH (0.1 M). To prepare the TEM grid, the sample was deposited on a polyvinyl butyral coated Cu 200 mesh grid inside a humid chamber. The grids were allowed to dry in air completely and stored in desiccator until and in between observations.

Images for particle size analysis was taken with a Philips CM10 TEM equipped with a digital camera (Olympus SIS MegaView G2) in the Microscopy Unit, Macquarie University. Images of two dimensional particle projections were fitted with ellipses, following the method in ref. 38, 66. The major and minor axes are reported as length and width and presented in Fig. 6b, and the width, length, and aspect ratio histograms are presented in Supplementary Fig. 20a, b, c, respectively. Error from such analyses arise from the unknown orientation of particles with respect to the TEM grid and from the ellipse approximation, both are apparently small[38,66].

Chemical composition of magnetosomes in two MTB from *d*=5.8 m and *d*=6.2 m were determined with a JEOL 2010F TEM in the Nuclear Materials Modeling and Characterization (NMMC) Programme, Australian Nuclear Science and Technology Organisation (ANSTO). All EDS spectra were collected with a live time of 30 sec. Due to the close proximity of magnetosome particles with one another and their position within the intact bacterial cell, the x-ray point analyses on individual particles likely contain signals from neighboring particles and the cell membrane.

2.4.8 MTB population turnover and Fe flux. MTB population turnover rate (i.e. the amount of time for all MTB present in the water column at any instantaneous time to die and fall out of the chemocline) was calculated from ferromagnetic particle concentration-dependent *IRM*, *ARM*, FMR total absorption and *M*s from the depth integrated water column filter measurements and the sediment trap measurements. The depth integrated signal was calculated for *d*=3.9-7.0 m only, where live MTB were observed during hanging-drop assay (Fig. 2b). An example of the MTB turnover rate calculated from the IRM signal is given in the Supplementary Methods. The results are summarized in Supplementary Table 7.

We calculate the flux of MTB Fe (i.e. the amount of MTB iron that is exported out of the chemocline per year) with the following parameters:

- Depth-integrated *M*s (*d*=3.9-7.0 m; from Supplementary Table 7) = 0.0015 $Am^2 m^{-2}$
- Average MTB turnover rate (Supplementary Table 7) = every 28.3 days or 12.9 times per year

- *M*s of magnetite (ref. 67) = 90 Am^2 kg^{-1}
- *M*s of greigite (ref. 68) = 59 Am^2 kg^{-1}

As Pettaquamscutt River Estuary is stratified year-round (complete water column overturn is not considered here), neglecting seasonally variations, the total MTB Fe flux out of the chemocline is 15.3 (as magnetite) – 18.2 (as greigite) µg Fe cm^{-2} yr^{-1}.

2.4.9 Magnetosome preservation. We compare the flux of magnetosomes (*ARM*, Am^2 cm^{-2} yr^{-1}) exported out of the chemocline with the surface sediment magnetic signal to estimate the preservation of magnetosomes. Without any diagenesis either in the sulfidic water column or in the surface sediment exposed to sulfidic water, using the averaged MTB turnover rate from Supplementary Table 7 (every 28.3 days or 12.9 times per year) and the *d*=3.9-7.0 m depth integrated *ARM* signal (6.3289×10^{-5} Am^2 m^{-2}), we can expect magnetosomes to contribute 8.15×10^{-4} Am^2 m^{-2} yr^{-1} to the surface sediment ARM signal.

The retrieved surface sediment sample represents sediment mixture from the top ~5 cm of the sediment. Using the following parameters we can calculate the magnetosome flux (*ARM* Am^2 cm^{-2} yr^{-1}) in the surface sediment:

- Sedimentation rate (averaged from 1962–2005 in ref. 69): 0.004 m yr^{-1}
- Dry sediment density (averaged from the top 6.25 cm of a sediment core in ref. 69): 2.12 $\times10^3$ kg m^{-3}
- Porosity (averaged from the top 6.25 cm of a sediment core in ref. 69): 0.9529
- Accumulation rate = (dry sediment density) × (sedimentation rate) × (1-porosity): 0.399 kg m^{-2} yr^{-1}
- ARM from magnetosomes in the surface sediment (77% of 1.1×10^{-3} Am^2 kg^{-1} estimated from ARM coercivity un-mixing, Supplementary Fig. 10): 8.5×10^{-4} Am^2 kg^{-1}

Therefore, the actual magnetosome flux to the surface sediment is 3.45×10^{-4} Am^2 m^{-2} yr^{-1}, or a 42% preservation.

Some fraction of the 58% of magnetosomes that are not preserved in the surface sediment can be attributed to reductive dissolution of magnetite magnetosomes in sulfidic water, which we estimate using the magnetite dissolution rate law from ref. 12:

$$\frac{dC_{mag}}{dt} = k\, C_s^{0.5} C_{mag} A_{mag} \qquad (2)$$

, where t is time in years, C_{mag} is the concentration of magnetite, k is the reaction rate constant, C_s is the sulfide concentration, A_{mag} is the specific surface area of magnetite grain, and the following parameters:

- Maximum amount of time the surface sediment we recovered has been exposed to sulfidic water: (sedimentation rate) × (5 cm) = 12.5 years
- C_s of Upper Pond, Pettaquamscutt River Estuary (ref. 40): 4 mM
- k: -1.5×10^{-6} (ref. 70) to -1.1×10^{-5} (ref. 12)
- A_{mag}: calculated using the Knud Thomsen's Formula for surface area of prolate spheroid from magnetosome particles size measured from d=5.0-5.4 m in the water column (semi-axis 25.8±8.6 nm and 23.1±11.5 nm), volume for prolate spheroid, and magnetite density of 5.175 g cm^{-3}, $A_{mag}=3.27\times10^{4}$ cm^2 g^{-1}.

According to the above, $C_{mag\_final} = e^{-bt}$, where b=0.0981 to 0.7194 depending on k, and over 12.5 years, on average 11.2% to 57.7% of magnetite magnetosomes that settled through the sulfidic water column and immersed in sulfidic water in the surface sediment are expected to dissolve.

The amount of magnetite vs. greigite magnetosome flux exported out of the chemocline was estimated by assuming that all *ARM* signal between d=3.9-5.0 m are from magnetite magnetosomes, *ARM* signal between d=5.0-6.0 m are from magnetite magnetosomes (50%) and greigite magnetosomes (50%), and all *ARM* signal between d=6.0-7.0 m are from greigite magnetosomes. The depth integrated *ARM* for magnetite and greigite magnetosome flux breakdown are summarized in Supplementary Table 8. Compared to the actual magnetosome flux to the surface sediment (3.45×10^{-4} Am^2 yr^{-1} m^{-2}), we estimate between 4.8% (if 1.540×10^{-4} Am^2 yr^{-1} m^{-2} magnetite magnetosome survived dissolution) to 42% (if 3.232×10^{-4} Am^2 yr^{-1} m^{-2} magnetite magnetosome survived dissolution) of the greigite magnetosome flux out of chemocline is preserved in the surface sediment after 12.5 years.

Acknowledgements

This work was supported by the Higher Degree Research fund from Department of Environment and Geography, Macquarie University and a visiting fellowship to the Institute for Rock Magnetism (IRM) to A.P.C. The authors thank the WHOI mooring team for the anchor and buoys loan, C. Lamborg (WHOI) for the sediment trap and YSI sensor loan, S. Simmons (MBL) for GeoPump loan and useful discussion, M. Johnson (WHOI) for site

suggestion and access to the compound microscope, L. Kerr (MBL) for TEM fixative and phosphate buffer, D. Birch (Macquarie University) for helpful discussion and access to TEM, C. Taylor and Z. Mlodzinska (WHOI) for providing bench space for filtration and cell fixation, J. Sepulveda and F. Schubotz (MIT) for $HgCl_2$ and access to freeze dryer, Princeton Measurement Corp for access to AGFM, A. Newell (North Carolina State University) for data and code for plotting putative sedimentary magnetofossils dimensions, R. Egli (Central Institute for Meteorology & Geodynamics) for making available CODICA & GECA, R. Harrison (University of Cambridge) for making available FORCinel v.2.01, J. Parker for the bathymetry map for Upper Pond, and D. Barry and S. Barry for discussion. The IRM is supported by the Instruments and Facilities Program of the NSF Division of Earth Science. This is IRM contribution 1404.

References

1. Bellini, S. On a unique behavior of freshwater bacteria. *Chin. J. Oceanol. Limnol.* 27, 3–5 (2009).
2. Blakemore, R. Magnetotactic bacteria. *Science* 190, 377–379 (1975).
3. Bazylizinki, D. A., Heywood, B. R., Mann, S. & Frankel, R. B. Fe304 and Fe3S4 in a bacterium. *Nature* 366, 218–218 (1993).
4. Bazylinski, D. A. *et al.* Controlled Biomineralization of Magnetite (Fe_3O_4) and Greigite (Fe_3S_4) in a Magnetotactic Bacterium. *Appl. Environ. Microbl.* 61, 3232–3239 (1995).
5. Bazylinski, D. A. & Moskowitz, B. M. Microbial biomineralization of magnetic iron minerals: microbiology, magnetism, and environmental significance. *in Geomicrobiology: Interactions Between Microbes and Minerals* Vol. 35: Reviews in Mineralogy (ed. Banfield, J. F. & Nealson, K. H.) 181–224 (Mineralogical Society of America, Washington, DC, 1997).
6. Simmons, S. L., Bazylinski, D. A. & Edwards, K. J. Population dynamics of marine magnetotactic bacteria in a meromictic salt pond described with qPCR. *Environ. Microbl.* 9, 2162–2174 (2007).
7. Moskowitz, B. M., Bazylinski, D. A., Egli, R., Frankel, R. B. & Edwards, K. J. Magnetic properties of marine magnetotactic bacteria in a seasonally stratified coastal pond (Salt Pond, MA, USA). *Geophys. J. Int.* 174, 75–92 (2008).
8. Simmons, S. L. & Edwards, K. J. Geobiology of magnetotactic bacteria. *in Magnetoreception and Magnetosomes in Bacteria* (ed. Schüler, D.) 77–102 (Springer, Berlin, Germany, 2007).

9. Kopp, R. E. & Kirschvink, J. L. The identification and biogeochemical interpretation of fossil magnetotactic bacteria. *Earth Sci. Rev.* 86, 42–61 (2008).
10. Lin, W., Bazylinski, D. A., Xiao, T., Wu, L.-F. & Pan, Y. Life with compass: diversity and biogeography of magnetotactic bacteria: Magnetotactic bacterial diversity and biogeography. *Environ. Microbl.* (2013). doi:10.1111/1462-2920.12313
11. Martins, J. L. *et al.* Grazing protozoa and magnetosome dissolution in magnetotactic bacteria. *Environ. Microbiol.* 9, 2775–2781 (2007).
12. Canfield, D. E. & Berner, R. A. Dissolution and pyritization of magnetite in anoxic marine sediments. *Geochim. Cosmochim. Acta.* 51, 645–659 (1987).
13. Vali, H. & Kirschvink, J. L. Magnetofossil dissolution in a palaeomagnetically unstable deep-sea sediment. *Nature* 339, 203–206 (1989).
14. Simmons, S. L. *Geobiology of Marine Magnetotactic Bacteria (Ph.D.)* (Massachusetts Institute of Technology and the Woods Hole Oceanographic Institution, 2006).
15. Meyer, K. M. & Kump, L. R. Oceanic euxinia in earth history: causes and consequences. *Annu. Rev. Earth Planet. Sci.* 36, 251–288 (2008).
16. Vasiliev, I. *et al.* Putative greigite magnetofossils from the Pliocene epoch. *Nat. Geosci.* 1, 782–786 (2008).
17. Reinholdsson, M., Snowball, I., Zillén, L., Lenz, C. & Conley, D. J. Magnetic enhancement of Baltic Sea sapropels by greigite magnetofossils. *Earth Planet. Sci. Lett.* 366, 137–150 (2013).
18. Moskowitz, B. M., Frankel, R. B. & Bazylinski, D. A. Rock magnetic criteria for the detection of biogenic magnetite. *Earth Planet. Sci. Lett.* 120, 283–300 (1993).
19. Egli, R. Characterization of Individual Rock Magnetic Components by Analysis of Remanence Curves, 1. Unmixing Natural Sediments. *Stud. Geophys. Geod.* 48, 391–446 (2004).
20. Weiss, B. P. *et al.* Ferromagnetic resonance and low-temperature magnetic tests for biogenic magnetite. *Earth Planet. Sci. Lett.* 224, 73–89 (2004).
21. Kopp, R. *et al.* Chains, clumps, and strings: Magnetofossil taphonomy with ferromagnetic resonance spectroscopy. *Earth Planet. Sci. Lett.* 247, 10–25 (2006).
22. Kopp, R. E. *et al.* Ferromagnetic resonance spectroscopy for assessment of magnetic anisotropy and magnetostatic interactions: A case study of mutant magnetotactic bacteria. *J. Geophys. Res.* 111, (2006).
23. Egli, R., Chen, A. P., Winklhofer, M., Kodama, K. P. & Horng, C.-S. Detection of noninteracting single domain particles using first-order reversal curve diagrams. *Geochem. Geophys. Geosyst.* 11, (2010).

24. Gehring, A. U., Kind, J., Charilaou, M. & García-Rubio, I. The detection of magnetotactic bacteria and magnetofossils by means of magnetic anisotropy. *Earth Planet. Sci. Lett.* 309, 113–117 (2011).
25. Jovane, L., Florindo, F., Bazylinski, D. A. & Lins, U. Prismatic magnetite magnetosome from cultivated magnetovibrio blakemorei strain MV-1: a magnetic fingerprint in marine sediments? *Environ. Microbiol. Rep*. 4, 664–668 (2012).
26. Egli, R. VARIFORC: An optimized protocol for calculating non-regular first-order reversal curve (FORC) diagrams. *Global Planet. Change* 110, 302–320 (2013).
27. Newell, A. J. A high-precision model of first-order reversal curve (FORC) functions for single-domain ferromagnets with uniaxial anisotropy: FORC. *Geochem. Geophys. Geosyst.* 6, (2005).
28. Charilaou, M., Winklhofer, M. & Gehring, A. U. Simulation of ferromagnetic resonance spectra of linear chains of magnetite nanocrystals. *J. Appl. Phys.* 109, 093903 (2011).
29. Lefèvre, C. T. *et al.* A Cultured Greigite-Producing Magnetotactic Bacterium in a Novel Group of Sulfate-Reducing Bacteria. *Science* 334, 1720–1723 (2011).
30. Pósfai, M., Buseck, P. R., Bazylinski, D. A. & Frankel, R. B. Reaction Sequence of Iron Sulfide Minerals in Bacteria and Their Use as Biomarkers. *Science* 280, 880–883 (1998).
31. Pósfai, M., Buseck, P. R., Bazylinski, D. A. & Frankel, R. B. Iron sulfides from magnetotactic bacteria: Structure, composition, and phase transitions. *Am. Mineral.* 83, 1469–1481 (1998).
32. Kasama, T. Magnetic properties, microstructure, composition, and morphology of greigite nanocrystals in magnetotactic bacteria from electron holography and tomography. *Am. Mineral.* 91, 1216–1229 (2006).
33. Keim, C. N., Abreu, F., Lins, U., Lins de Barros, H. & Farina, M. Cell organization and ultrastructure of a magnetotactic multicellular organism. *J. Struct. Biol.* 145, 254–262 (2004).
34. Chen, Y. *et al.* A novel species of ellipsoidal multicellular magnetotactic prokaryotes from Lake Yuehu in China: The ellipsoidal MMPs from the Lake Yuehu. *Environ. Microbl.* (2014). doi:10.1111/1462-2920.12480
35. Lefèvre, C. T. & Bazylinski, D. A. Ecology, Diversity, and Evolution of Magnetotactic Bacteria. *Microbiol. Mol. Biol. Rev.* 77, 497–526 (2013).
36. Watanabe, S., Akutagawa, S., Sawada, K., Iwasa, T. & Shimoyama, Y. A ferromagnetic resonance study of iron complexes as biologically synthesized in magnetic bacteria. *Mater. Trans.* 50, 2187–2191 (2009).

37. Faivre, D., Fischer, A., García-Rubio, I., Mastrogiacomo, G. & Gehring, A. Development of cellular magnetic dipoles in magnetotactic bacteria. *Biophys. J.* 99, 1268-1273 (2010).
38. Pósfai, M. *et al.* Crystal-size distributions and possible biogenic origin of Fe sulfides. *Eur. J. Mineral.* 13, 691–703 (2001).
39. Gaines, A. G. J. & Pilson, M. E. Anoxic water in the Pettaquamscutt River. *Limnol. Oceanogr.* 17, 42–49 (1972).
40. Wilkins, R. T. & Barnes, H. L. Pyrite Formation in an anoxic estuarine basin. *Am. J. Sci.* 297, 620–650 (1997).
41. DeLong, E. F., Frankel, R. B. & Bazylinski, D. A. Multiple Evolutionary Origins of Magnetotaxis in Bacteria. *Science* 259, 803–806 (1993).
42. Frankel, R. B., Bazylinski, D. A., Johnson, M. S. & Taylor, B. L. Magneto-aerotaxis in marine, coccoid bacteria. *Biophys. J.* 73, 994–1000 (1997).
43. Bazylinski, D. A. *et al.* Magnetococcus marinus gen. nov., sp. nov., a marine, magnetotactic bacterium that represents a novel lineage (Magnetococcaceae fam. nov., Magnetococcales ord. nov.) at the base of the Alphaproteobacteria. *Int. J. Syst. Evol. Micr.* 63, 801–808 (2013).
44. Chang, L. *et al.* Ferromagnetic resonance characterization of greigite (Fe_3S_4), monoclinic pyrrhotite (Fe_7S_8), and non-interacting titanomagnetite ($Fe_{3-x}Ti_xO_4$). *Geochem. Geophys. Geosyst.*13, (2012).
45. Sorokina, O. N., Bychkova, A. V. & Kovarskii, A. L. Analysis of the ferromagnetic resonance spectra of aggregates of magnetite nanoparticles formed by a magnetic field. *Russ. J. Phys. Chem. B.* 3, 257–261 (2009).
46. Egli, R. Theoretical considerations on the anhysteretic remanent magnetization of interacting particles with uniaxial anisotropy. *J. Geophys. Res.* 111, (2006).
47. Egli, R. Theoretical aspects of dipolar interactions and their appearance in first-order reversal curves of thermally activated single-domain particles. *J. Geophys. Res.* 111, (2006).
48. Maloof, A. C. *et al.* Sedimentary iron cycling and the origin and preservation of magnetization in platform carbonate muds, Andros Island, Bahamas. *Earth Planet. Sci. Lett.* 259, 581–598 (2007).
49. Roberts, A. P., Chang, L., Heslop, D., Florindo, F. & Larrasoaña, J. C. Searching for single domain magnetite in the 'pseudo-single-domain' sedimentary haystack: Implications of biogenic magnetite preservation for sediment magnetism and relative paleointensity determinations. *J. Geophys. Res.* 117, (2012).

50. Kodama, K. P., Moeller, R. E., Bazylinski, D. A., Kopp, R. E. & Chen, A. P. The mineral magnetic record of magnetofossils in recent lake sediments of Lake Ely, PA. *Global. Planet. Change* (2013). doi:10.1016/j.gloplacha.2013.03.012
51. Mao, X., Egli, R., Petersen, N., Hanzlik, M. & Zhao, X. Magnetotaxis and acquisition of detrital remanent magnetization by magnetotactic bacteria in natural sediment: First experimental results and theory. *Geochem. Geophys. Geosys.*15, 255–283 (2014).
52. Kruiver, P., Dekkers, M. J. & Heslop, D. Quantification of magnetic coercivity components by the analysis of acquisition curves of isothermal remanent magnetisation. *Earth Planet. Sci. Lett.* 189, 269–276 (2001).
53. Egli, R. Analysis of the field dependence of remanent magnetization curves. *J. Geophys. Res.* 108, (2003).
54. Winklhofer, M., Chang, L. & Eder, S. H. K. On the magnetocrystalline anisotropy of greigite (Fe_3S_4). *Geochem. Geophys. Geosyst.* (2014). doi:10.1002/2013GC005121
55. Newell, A. J. Transition to superparamagnetism in chains of magnetosome crystals. *Geochem. Geophys. Geosys.* 10, (2009).
56. Muxworthy, A. R. *et al.* Critical single domain grain sizes in chains of interacting greigite particles: Implications for magnetosome crystals: Single Domain Grain Sizes in Greigite. *Geochem. Geophys. Geosys.* 14, 5430–5441 (2013).
57. Penninga, I., Waard, H. de, Moskowitz, B. M., Bazylinski, D. A. & Frankel, R. B. Remanence measurements on individual magnetotactic bacteria using a pulsed magnetic field. *J. Magn. Magn. Mater.* 149, 279–286 (1995).
58. Hanzlik, M., Winklhofer, M. & Petersen, N. Pulsed-field-remanence measurements on individual magnetotactic bacteria. *J. Magn. Magn. Mater.* 248, 258–267 (2002).
59. Winklhofer, M., Abraçado, L. G., Davila, A. F., Keim, C. N. & Lins de Barros, H. G. P. Magnetic Optimization in a Multicellular Magnetotactic Organism. *Biophys. J.*92, 661–670 (2007).
60. Rowan, C. J. & Roberts, A. P. Magnetite dissolution, diachronous greigite formation, and secondary magnetizations from pyrite oxidation: Unravelling complex magnetizations in Neogene marine sediments from New Zealand. *Earth Planet. Sci. Lett.* 241, 119–137 (2006).
61. Anderson, T. F. & Raiswell, R. Sources and mechanisms for the enrichment of highly reactive iron in euxinic Black Sea sediments. *Am. J. Sci.* 304, 203–233 (2004).
62. Hubeny, J. B., King, J. W. & Cantwell, M. Anthropogenic influences on estuarine sedimentation and ecology: examples from the varved sediments of the Pettaquamscutt River Estuary, Rhode Island. *J. of Paleolimnol.* 41, 297–314 (2009).

63. Jackson, M. & Solheid, P. On the quantitative analysis and evaluation of magnetic hysteresis data. *Geochem. Geophys. Geosys.* 11, (2010).
64. Harrison, R. J. & Feinberg, J. M. FORCinel: An improved algorithm for calculating first-order reversal curve distributions using locally weighted regression smoothing. *Geochem. Geophys. Geosys.* 9, (2008).
65. Heslop, D. & Roberts, A. P. Estimation of significance levels and confidence intervals for first-order reversal curve distributions. *Geochem. Geophys. Geosys.* 13, (2012).
66. Devouard, B. *et al.* Magnetite from magnetotactic bacteria: Size distribution and twinning. *Am. Mineral.* 83, 1387–1399 (1998).
67. Dunlop, D. J. & Özdemir,, O. Rock Magnetism Fundamentals and Frontiers, p.573, (Cambridge University Press, Cambridge, UK, 2001).
68. Chang, L. *et al.* Fundamental magnetic parameters from pure synthetic greigite (Fe_3S_4). *J. Geophys. Res.* 113, (2008).
69. Lima, A. L. *et al.* High-resolution historical records from Pettaquamscutt River basin sediments: 1. 210Pb and varve chronologies validate record of 137Cs released by the Chernobyl accident. *Geochim. Cosmochim Acta* 69, 1803–1812 (2005).
70. Egli, R. Characterization of individual rock magnetic components by analysis of remanence curves. 3. Bacterial magnetite and natural processes in lakes. *Phys. Chem. Earth* 29, 869–884 (2004).

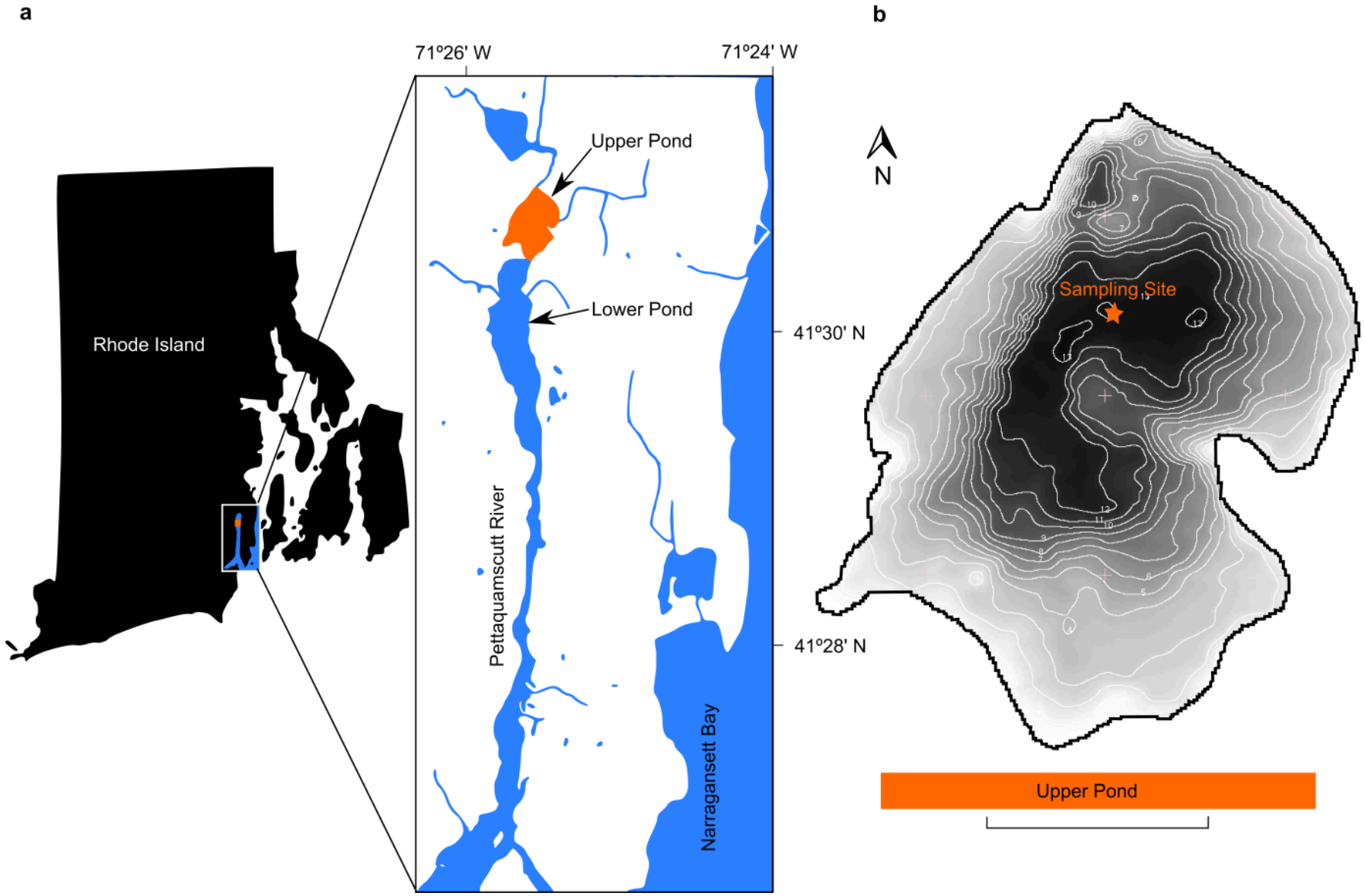

Figure 2-1: Sampling site. (a) The location of Upper Pond in the Pettaquamscutt River Estuary, Rhode Island, U.S.A. (b) Zoomed in bathymetry map of the Upper Pond. Scale bar = ¼ km.

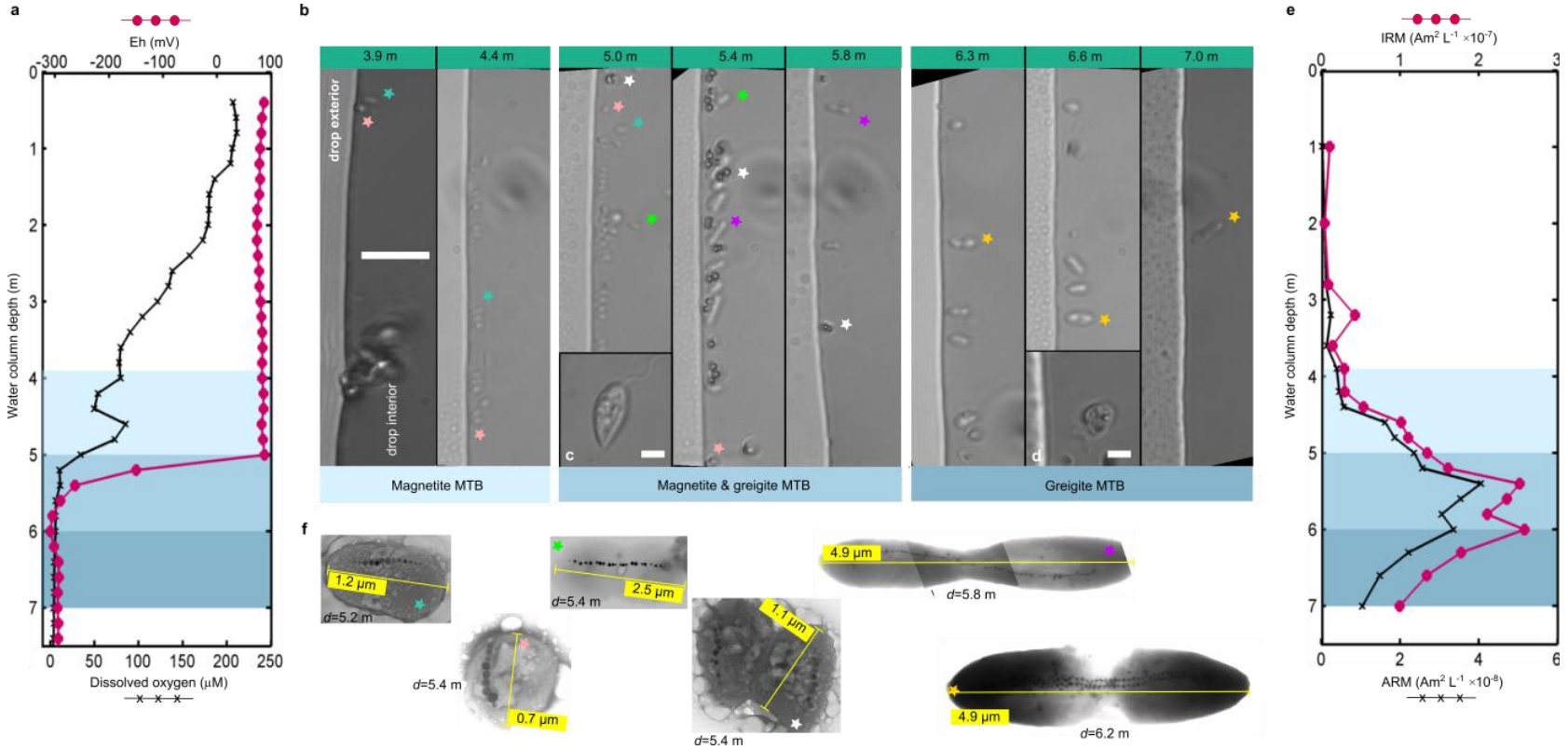

Figure 2-2: Upper Pond water column profiles and microscopy observations. (a) Water column dissolved oxygen and *Eh* measured on September 15th, 2012. (b) Light microscopy hanging-drop live MTB assay images for selected water depths between *d*=3.9-7.0 m where live MTB were observed. Except for the images of magnetic responsive protists at (c) *d*=5.0 m and (d) *d*=6.6 m, the 10 μm scale bar applies to all other hanging-drop images. The scale bars in (c) and (d) both denote 50 μm. All images were captured on the hanging-drop edge corresponding to North-seeking MTB. (e) Ferrimagnetic particle concentration-dependent parameters: isothermal remanent magnetization (*IRM*; 200 mT) and anhysteretic remanent magnetization (*ARM*, AF_{max}=200 mT, *DC*=0.1 mT). (f) Transmission electron microscopy (TEM) images of selected MTB cells. MTBs from *d*=5.8 m and *d*=6.2 m are analyzed for their magnetosome composition (see Fig. 3). The colored stars mark probable MTB morphotype connection between the TEM images and the light-microscopy hanging-drop assay. Light, medium, dark shades of blue demarcate water column zones inhabited by magnetite MTB, mixed magnetite and greigite MTB, and greigite MTB, respectively (see text).

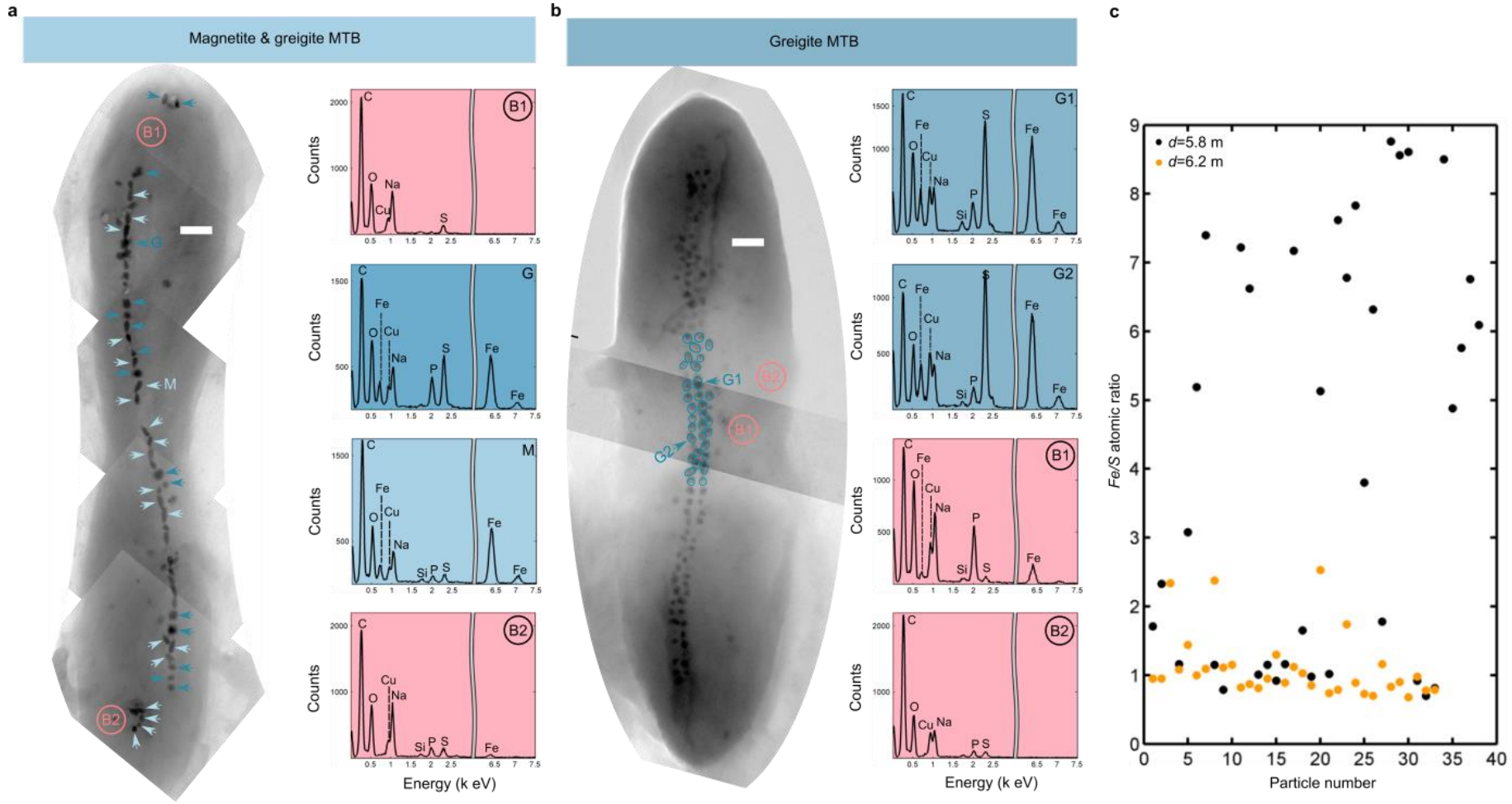

Figure 2-3: Composition analyses on MTB magnetosomes and background membrane. (a) *d*=5.8 m and (b) *d*=6.2 m analyzed with EDS. The particles in the magnetosome chain in the MTB from *d*=5.8 m show an approximately binary distribution of atomic *Fe/S* ratio. We have interpreted particles with *Fe/S*>3 as magnetite magnetosomes (marked by light blue arrows next to the particles), and *Fe/S*<3 as greigite magnetosomes (marked by dark blue arrows next to the particles). In contrast, all of the particles analyzed (blue ellipses) in MTB from *d*= 6.2 m have *Fe/S*<3 (c), which are likely greigite magnetosomes. EDS spectra are shown for selected representative particles/membrane as marked. No EDS peaks were identified for 3 <kV <6. B1 and B2 represent background cell membrane EDS signals.

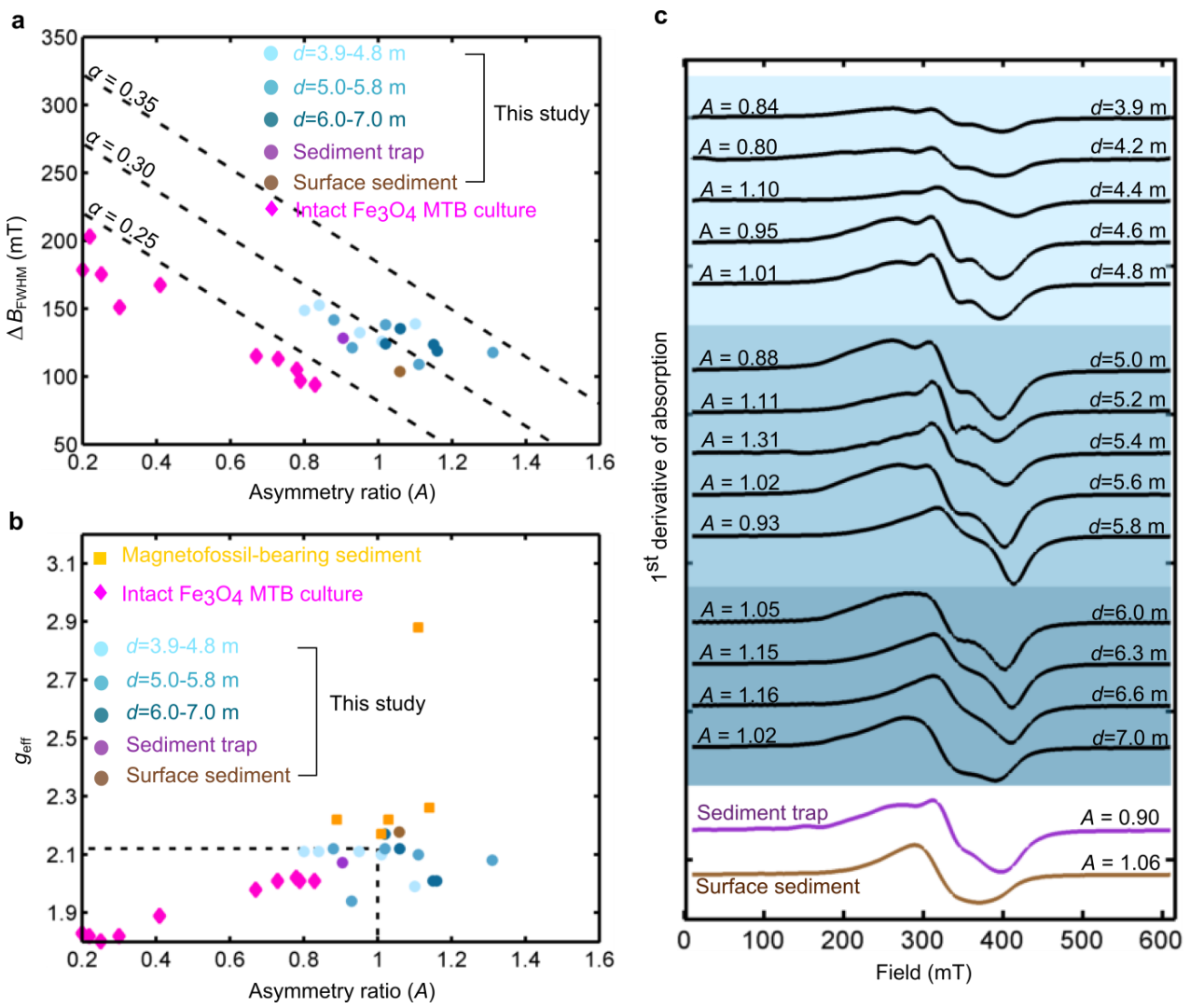

Figure 2-4: Ferromagnetic resonance spectra and derived empirical parameters. (a, b) FMR empirical parameters from this study, cultured magnetite MTB[20-22,24,25,37], and magnetofossil-bearing sediments[,20,21]. Intact magnetite MTB cultures are defined by the following parameters range: g_{eff}<2.12, asymmetry ratio A<1, and α<0.25. The parameters from this study fall within the range 0.80<A<1.31, 1.94<g_{eff}<2.17, 0.28<α< 0.34. (c) FMR absorption derivative spectra (with compressed ordinate scaling) from water column filters, sediment trap, and surface sediment samples.

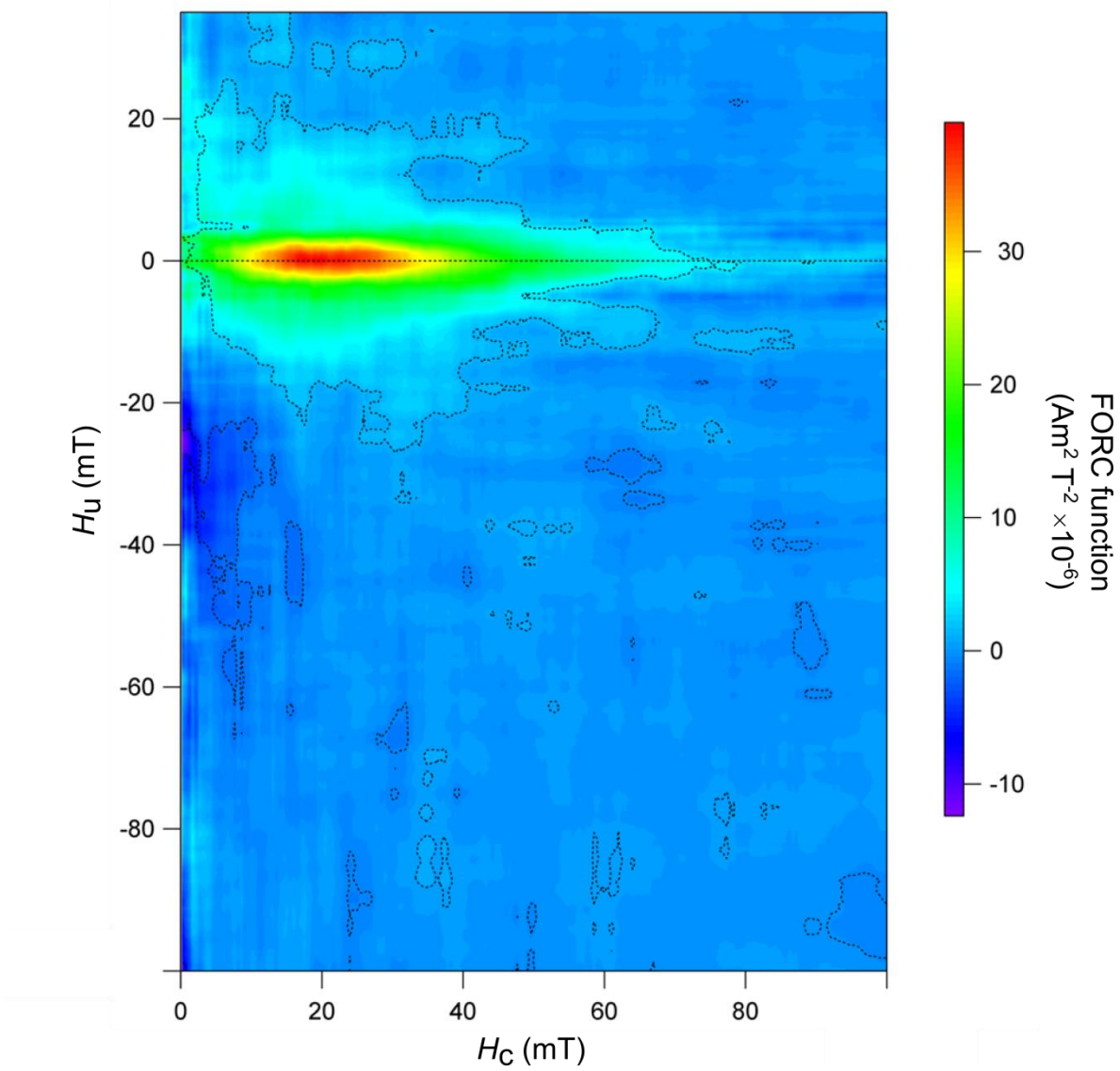

Figure 2-5: First order reversal curves diagram from greigite MTB. The measurement was made on a stack of filter containing >0.22 µm particulate filtered from 330 mL of water from *d*=6.6 m. Five identical sets of raw data were averaged and processed with a variable smoothing grid: S_c=15, $S_{u,0}$=10, $S_{u,1}$=15, λ_H=0.1. The dotted contours denote FORC distributions that are significant at the 0.05 level.

a

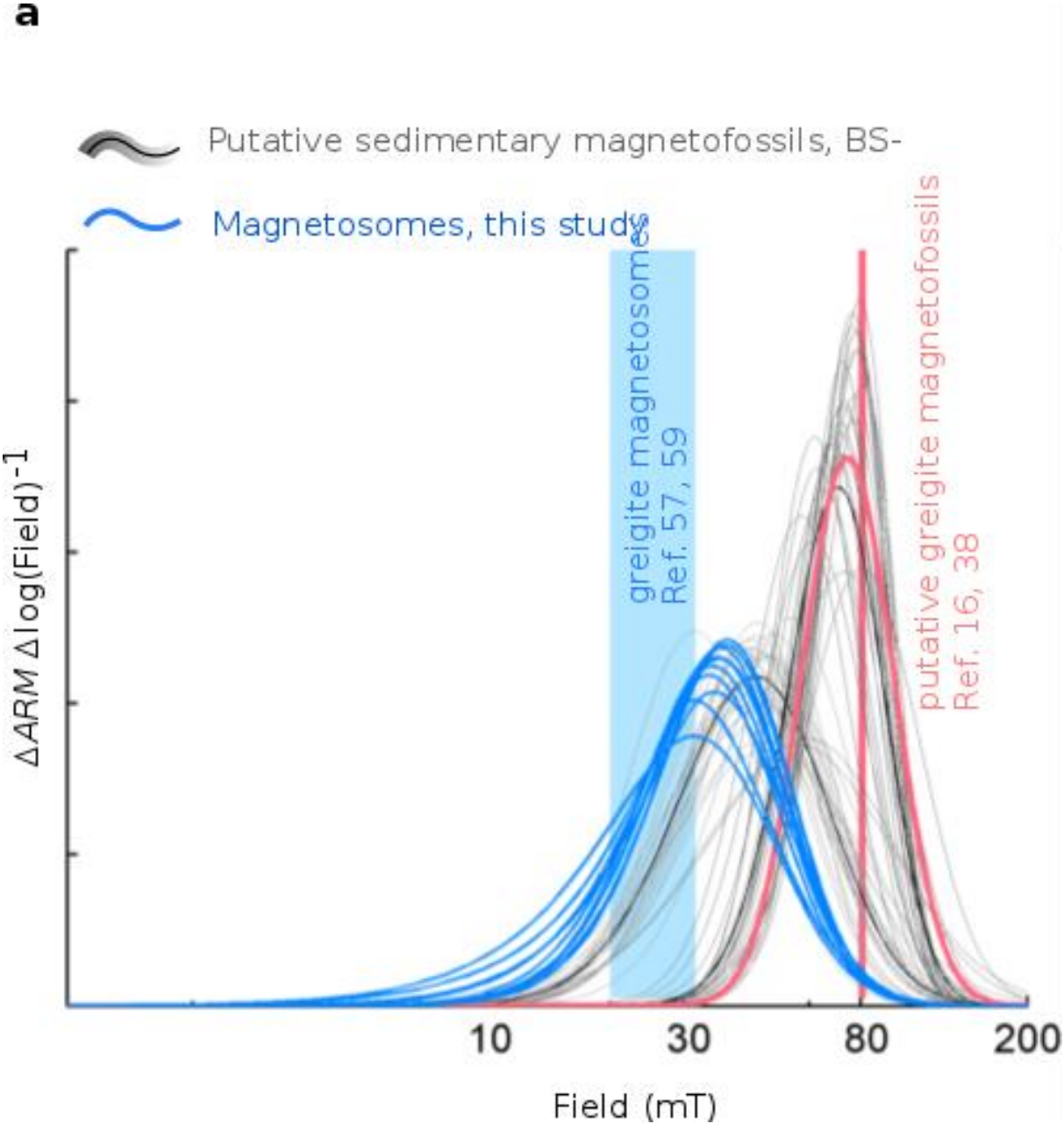
Putative sedimentary magnetofossils, BS-
Magnetosomes, this study
greigite magnetosomes
Ref. 57, 59
putative greigite magnetofossils
Ref. 16, 38
ΔARM Δlog(Field)-1
10
30
80
200
Field (mT)

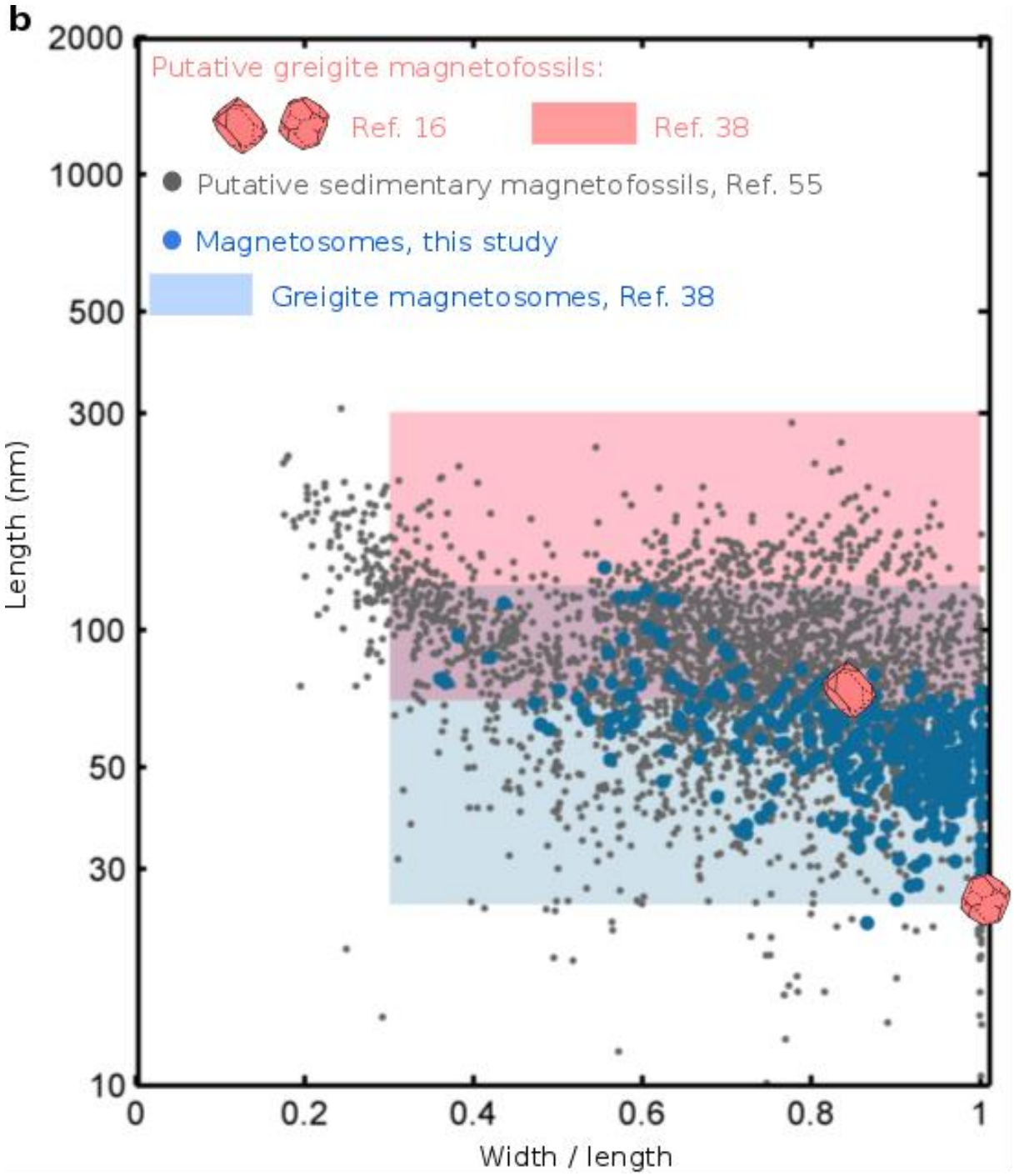
b
Putative greigite magnetofossils:
Ref. 16
Ref. 38
Putative sedimentary magnetofossils, Ref. 55
Magnetosomes, this study
Greigite magnetosomes, Ref. 38
Length (nm)
2000
1000
500
300
100
50
30
10
0
0.2
0.4
0.6
0.8
1
Width / length

Figure 2-6: Coercivity distribution and magnetosome size and shape. (a) Blue curves: *ARM* coercivity distribution of the water column samples from this study. Grey curves: hypothesized sedimentary magnetofossil coercivity distribution components BS-BM and BH-BI[19]. Black curves: averaged BS-BM and BH-BI. Thick light blue band: average coercivity determined from pulse-field experiments on individual greigite MTB from ref. 57, 59. Thin magenta band: approximate median coercivity from a Miocene marl in ref. 38 containing greigite with similar crystal size distribution as MMP ("many-celled magnetotactic prokaryote"), a greigite-producing MTB. Magenta curve: coercivity distribution determined from *IRM* acquisition curve un-mixing from Pliocene sediment containing putative greigite magnetofossils[16]. (b) Aspect ratio (width/length) vs. length for 377 magnetosomes imaged from 21 MTB in this study (blue dots). The grey dots (n ~3000) are measured length and aspect ratio from putative magnetofossils extracted from marine and lacustrine sediments[55]. Blue and magenta boxes mark the length and aspect ratio ranges for MMP magnetosomes and greigite from the Miocene marl sample mentioned above, respectively, from ref. 38. Magenta symbols denote magnetofossil shapes for the claimed oldest greigite magnetofossils from ref. 16.

Supplementary Information

Supplementary Figures

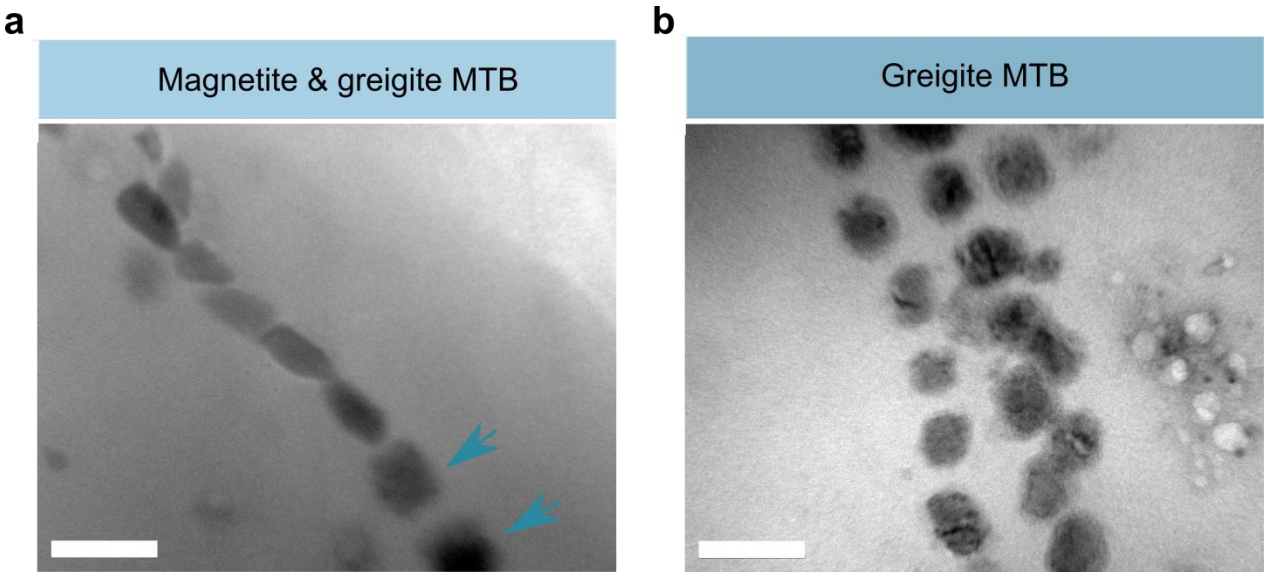

Supplementary Figure 2-1 | TEM images of greigite magnetosomes. Magnetosomes in MTB from (**a**) *d*=5.8 m and (**b**) *d*=6.2 m. Two magnetosomes marked by dark blue arrows in (**a**) and all magnetosomes shown in (**b**) have atomic ratio *Fe/S*<3, which we interpret to be greigite in composition. White scale bar denotes 100 nm.

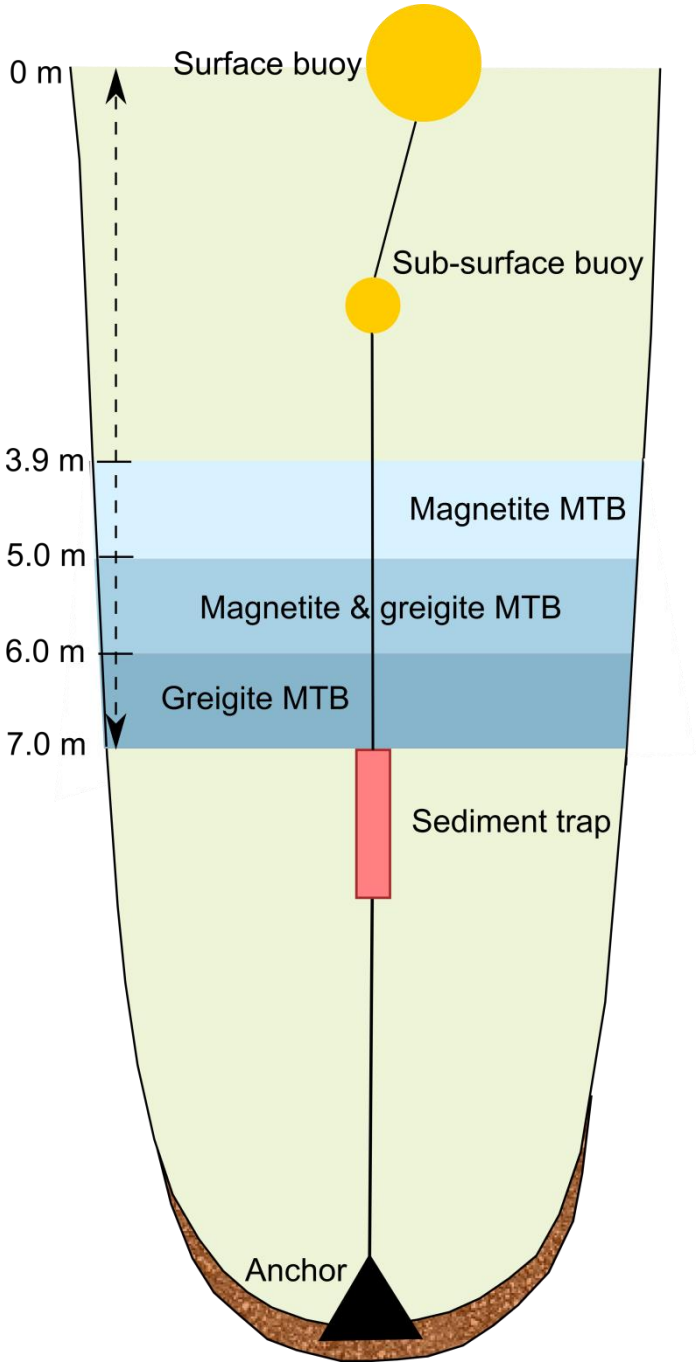

Supplementary Figure 2-2 | Sediment trap schematic.

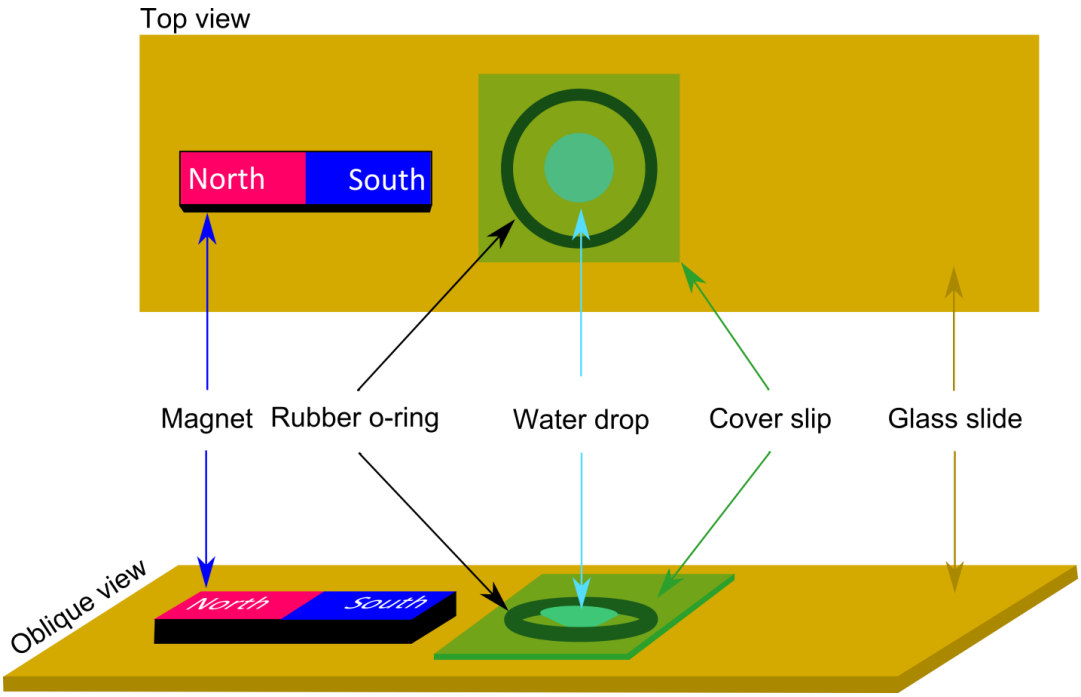

Supplementary Figure 2-3 | Live MTB assay schematic. A 20 µL water droplet is "hung" on a glass cover slip and seated on a rubber O-ring that is sitting on a glass slide positioned on a compound microscope stage. A refrigerator bar magnet is placed on one side of the droplet for ~30 seconds before observation (schematic modified from UWA Biophysics[1]).

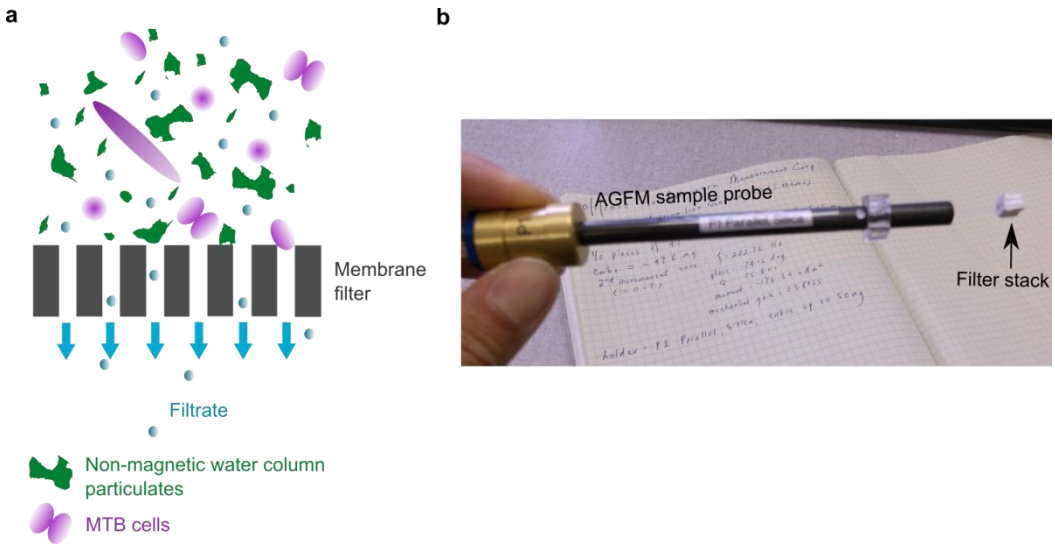

Supplementary Figure 2-4 | Vacuum filtration schematic and filter stack image. (**a**) Graphical illustration of the "dead-end" vacuum filtration method (schematic modified from SpectrumLabs[2]). (**b**) An example of a 'filter stack' used for hysteresis, FORC, and FMR measurements. The filter stack has an approximate dimension of 5×5×5 mm.

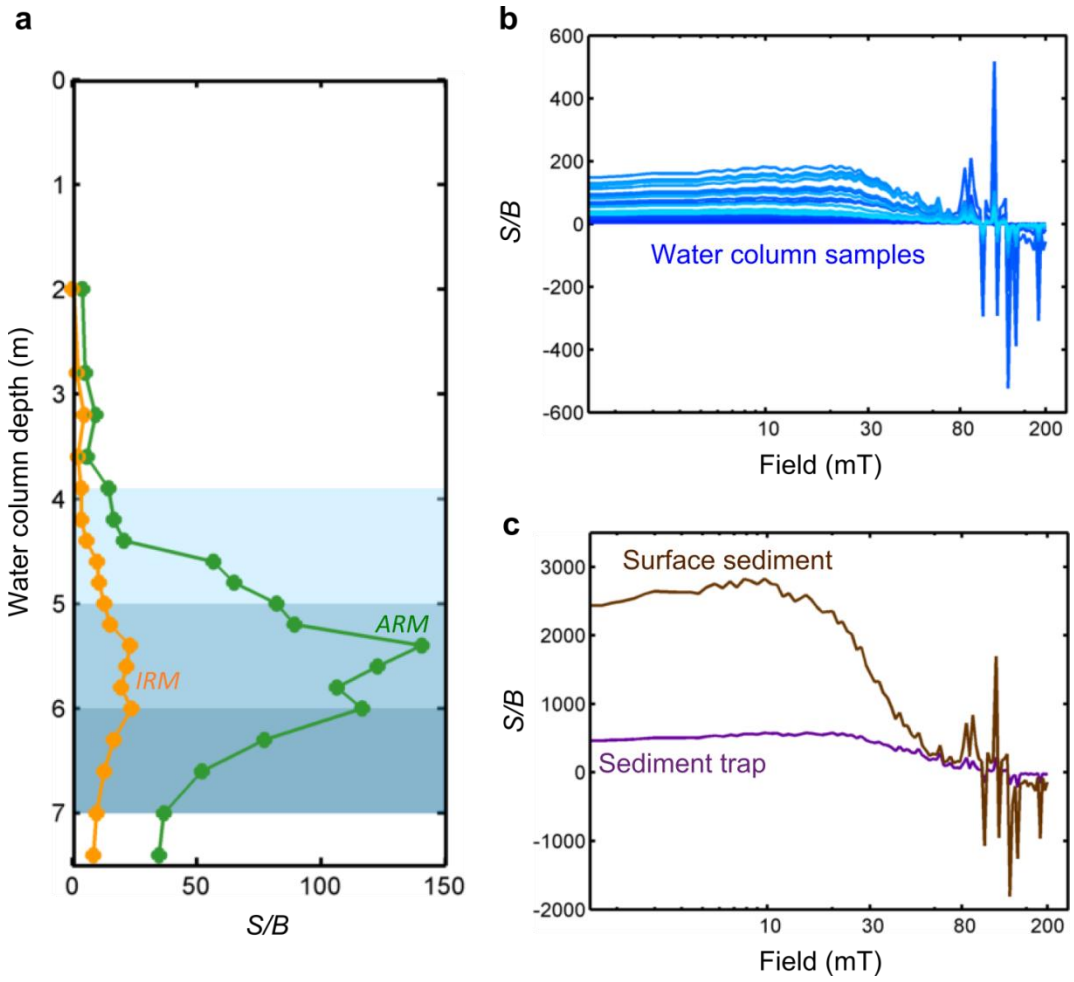

Supplementary Figure 2-5 | Remanent magnetization sample signal to blank signal ratio. (**a**) Sample-to-blank ratio (*S/B*) as a function of water depth for *ARM* (*AF*=0) and *IRM* measured from the water column filter samples. *S/B* as a function of *AF* along a single-axis for (**b**) samples from the water column *d*=2.0-7.4 m (darker shade of blue denotes deeper water depths) and (**c**) sediment trap and surface sediment samples. For the water column and sediment trap samples, the blank specimen used for comparison consists of four 47 mm un-used filters (pore size 0.8-8 µm, 1.2 µm, 0.45 µm, 0.22 µm) and empty plastic cube. For the surface sediment sample, the blank specimen used for comparison consists of empty plastic cube only. In (**a**), light, medium, dark shades of blue demarcate water column zones inhabited by magnetite MTB, mixed magnetite and greigite MTB, and greigite MTB, respectively (see text).

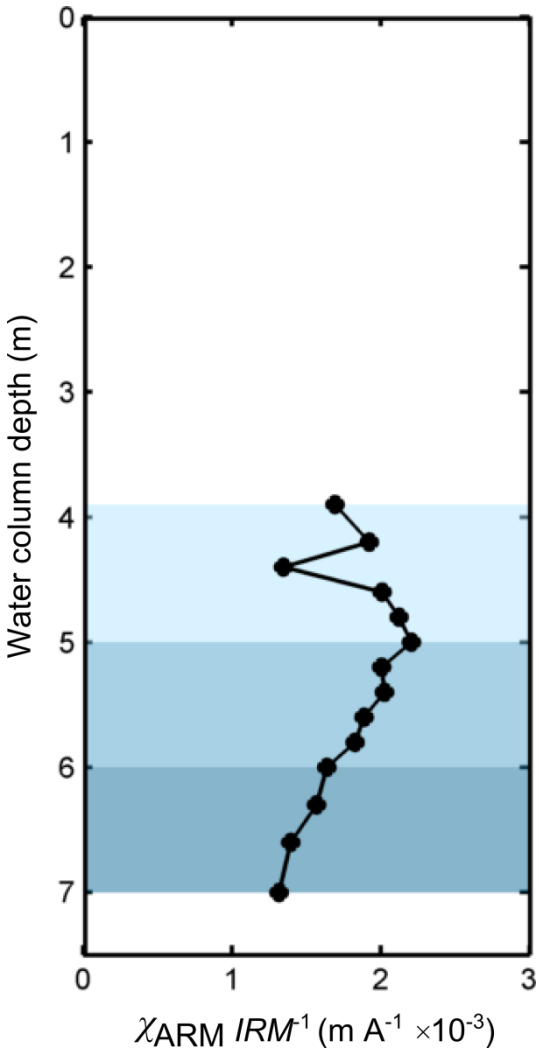

Supplementary Figure 2-6 | Susceptibility of *ARM* to *IRM* ratio as a function of water depth. Susceptibility of *ARM* (χ_{ARM}) acquired from AF_{max}=200 mT, *DC*=0.1 mT. Light, medium, dark shades of blue demarcate water column zones inhabited by magnetite MTB, mixed magnetite and greigite MTB, and greigite MTB, respectively (see text).

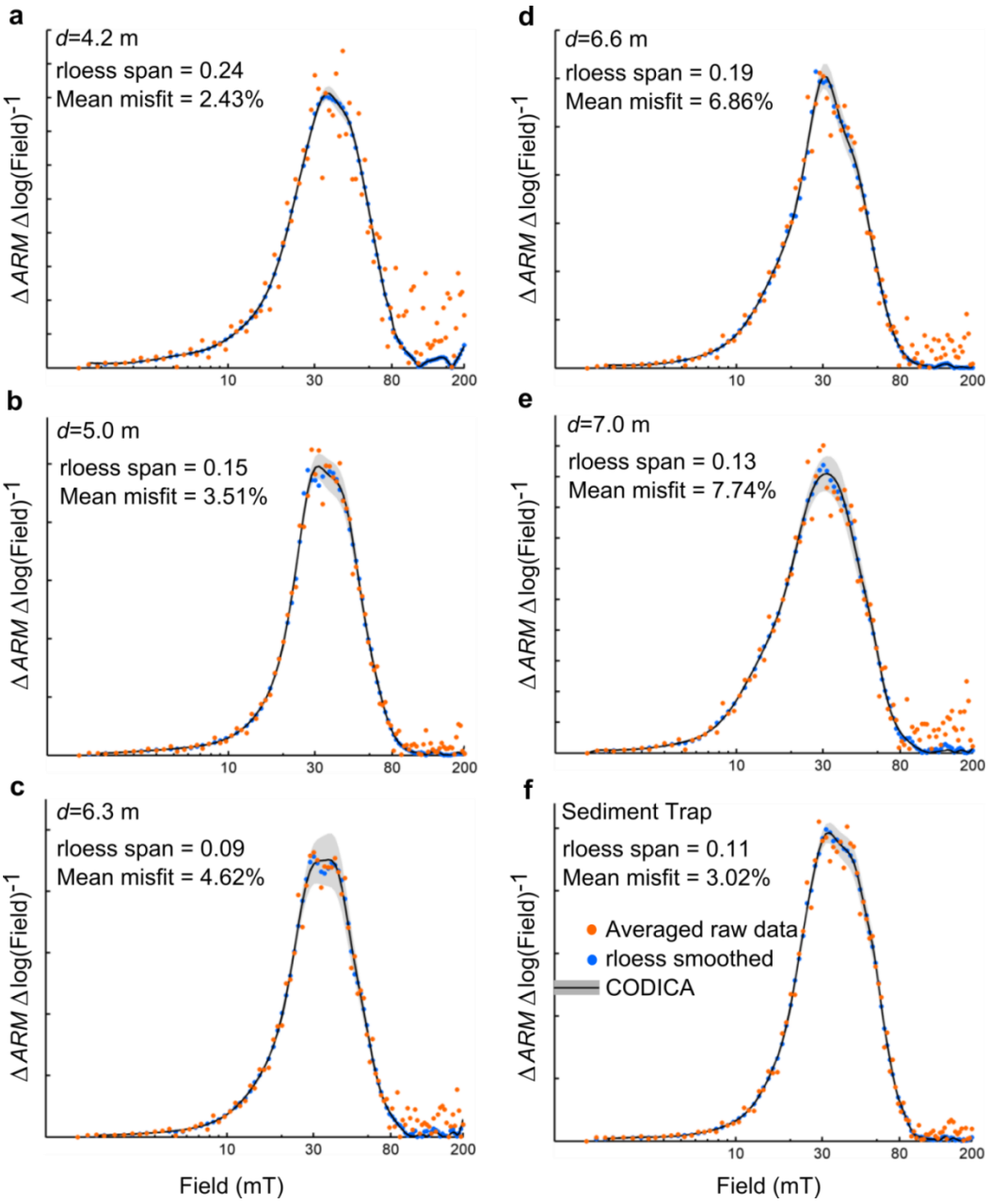

Supplementary Figure 2-7 | Coercivity distribution from *ARM AF* demagnetization of selected samples. Orange dots: numerical derivative of averaged raw data; Blue dots: numerical derivative of robust loess smoothed (span specified) averaged raw data shown in orange; Coercivity distribution (black thin line) and 95% confidence interval (grey thick line) calculated by CODICA from smoothed data.

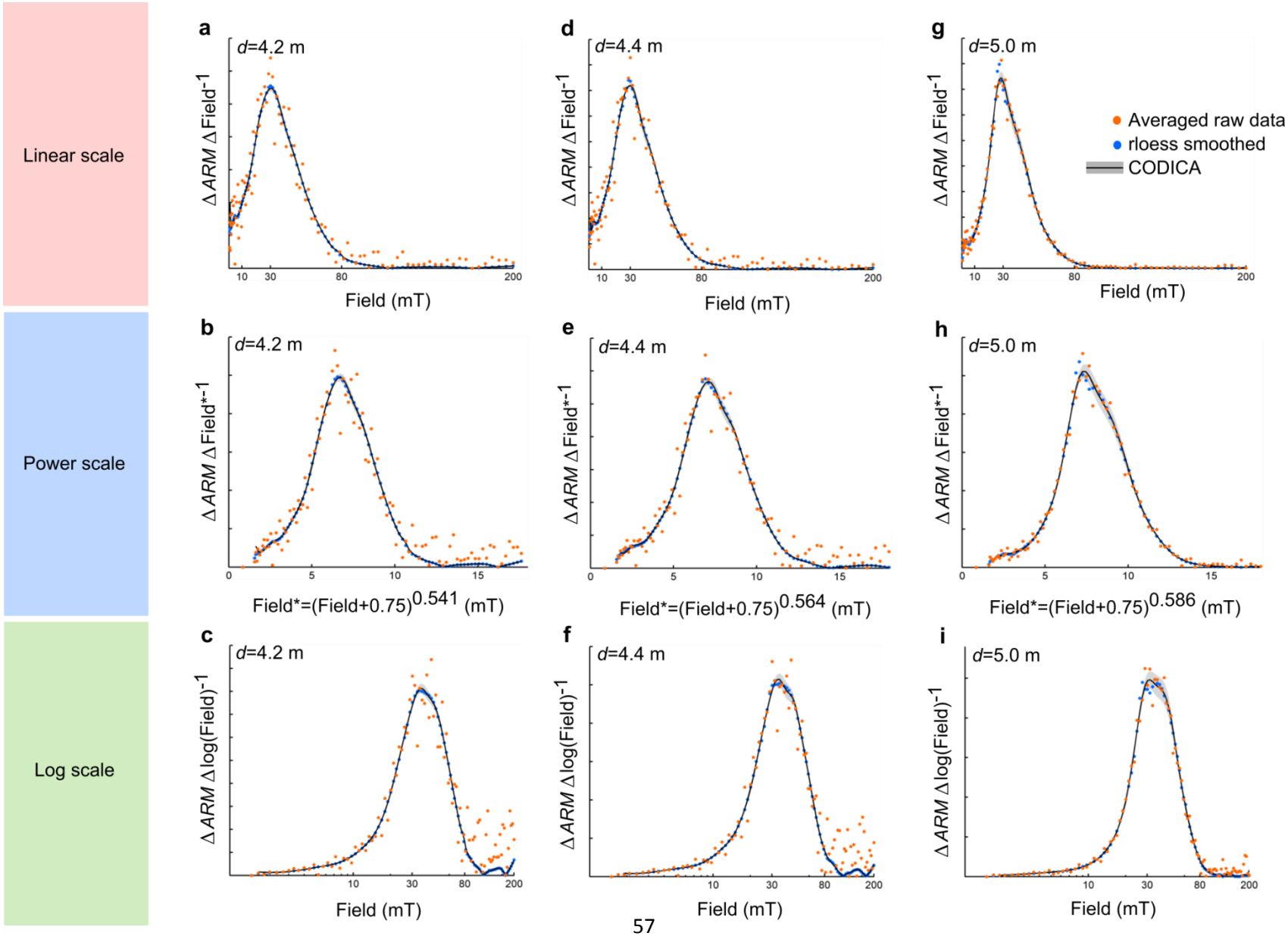
Linear scale
Power scale
Log scale
a
d=4.2 m
ΔARM ΔField-1
Field (mT)
d
d=4.4 m
ΔARM ΔField-1
Field (mT)
g
d=5.0 m
ΔARM ΔField-1
Field (mT)
Averaged raw data
rloess smoothed
CODICA
b
d=4.2 m
ΔARM ΔField*-1
Field*=(Field+0.75)0.541 (mT)
e
d=4.4 m
ΔARM ΔField*-1
Field*=(Field+0.75)0.564 (mT)
h
d=5.0 m
ΔARM ΔField*-1
Field*=(Field+0.75)0.586 (mT)
c
d=4.2 m
ΔARM Δlog(Field)-1
Field (mT)
f
d=4.4 m
ΔARM Δlog(Field)-1
Field (mT)
i
d=5.0 m
ΔARM Δlog(Field)-1
Field (mT)

Supplementary Figure 2-8 (above) | Coercivity distribution from *ARM AF* demagnetization on three different field scales. (**a**, **d**, **g**) Coercivity distribution on linear scale. The exponents for the power field scale in (**b**, **e**, **h**) are obtained in CODICA and correspond to the exponent that produced the most symmetric curve after all CODICA detected outliers have been removed. When the log scale coercivity distributions (**c**, **f**, **h**) calculated by CODICA for each of these samples were fitted with one skewed Gaussian in GECA, all of them failed the Pearson's χ^2 test. Orange dots: numerical derivative of averaged raw data; Blue dots: numerical derivative of robust loess smoothed (span specified) averaged raw data shown in orange dots; Coercivity distribution (black thin line) and 95% confidence interval (grey thick line) calculated by CODICA from smoothed data.

Supplementary Figure 2-9 (below) | Parametric *ARM* coercivity spectra fitting for selected water column samples. Results for averaged (normalized) *d*=3.9-7.0 m *ARM* alternating field demagnetization curves, *d*=4.2 m, *d*=4.4 m, and *d*=5.0 m. The latter of these three did not pass the Pearson's χ^2 test when fitted with one SGG (see Supplementary Table 2). (**a**) Initial "guesses" for the 2 end members are based on the averaged D-D+Ex and BS-BM parameters from ref. 3 (for the *d*=3.9-7.0 m average) and the optimized fitting result of *d*=3.9-7.0 m (for *d*=4.2 m, *d*=4.4 m, *d*=5.0 m). (**b**) GECA optimized 2 end member fitting results from the initial parameters in (**a**). Except for *d*=4.2 m, *d*=4.4 m and *d*=5.0 m both pass the Pearson's χ^2 test in GECA. Orange dots: numerical derivative of averaged raw data; Coercivity distribution (black thin line) and 95% confidence interval (grey thick line) calculated by CODICA from smoothed data. The percentages shown in (**b**) are the fractional contribution to the total *ARM* from each end member.

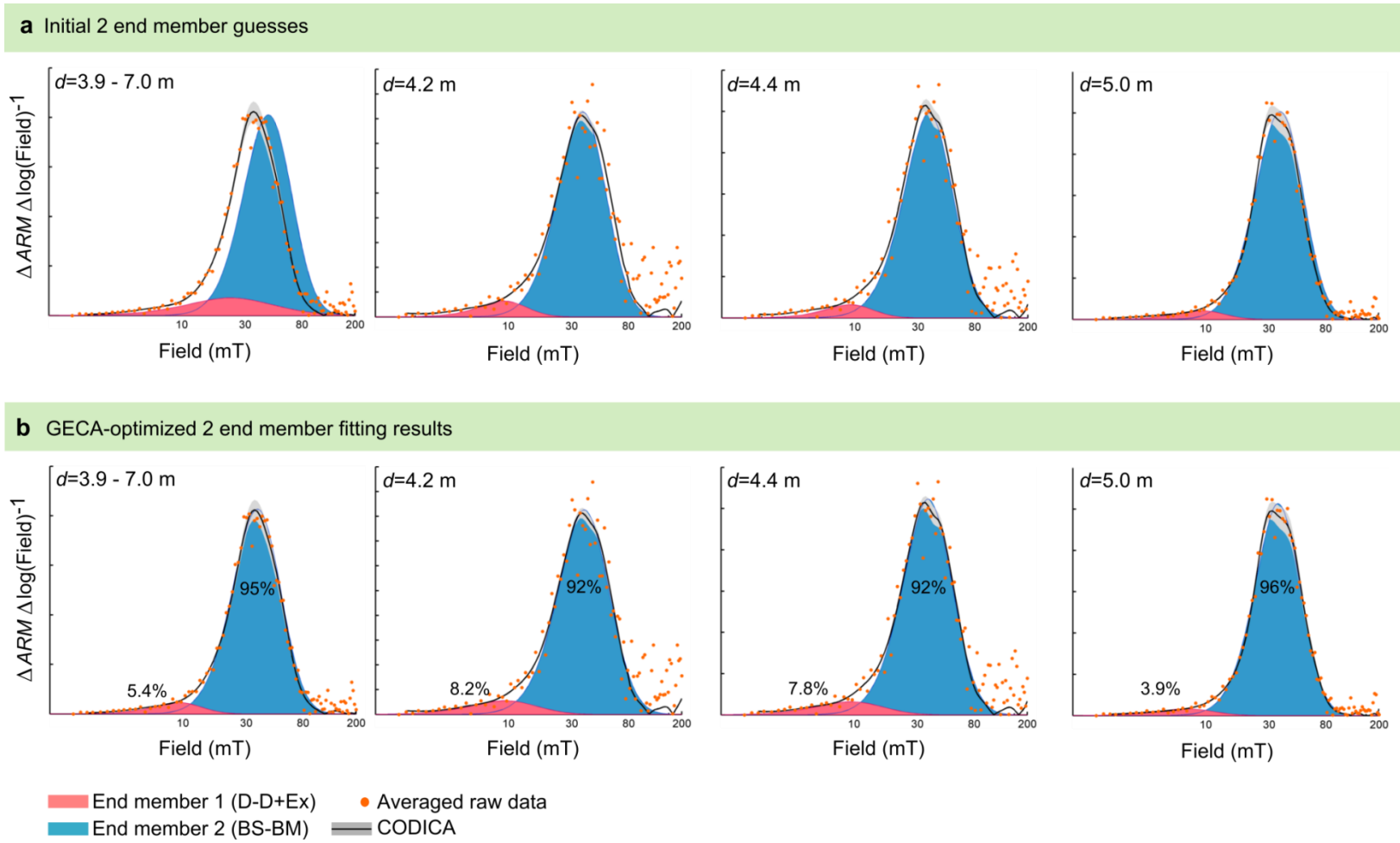
a Initial 2 end member guesses
d=3.9 - 7.0 m
d=4.2 m
d=4.4 m
d=5.0 m
Δ ARM Δ log(Field)-1
10
30
80
200
Field (mT)
b GECA-optimized 2 end member fitting results
95%
92%
92%
96%
5.4%
8.2%
7.8%
3.9%
End member 1 (D-D+Ex)
End member 2 (BS-BM)
Averaged raw data
CODICA

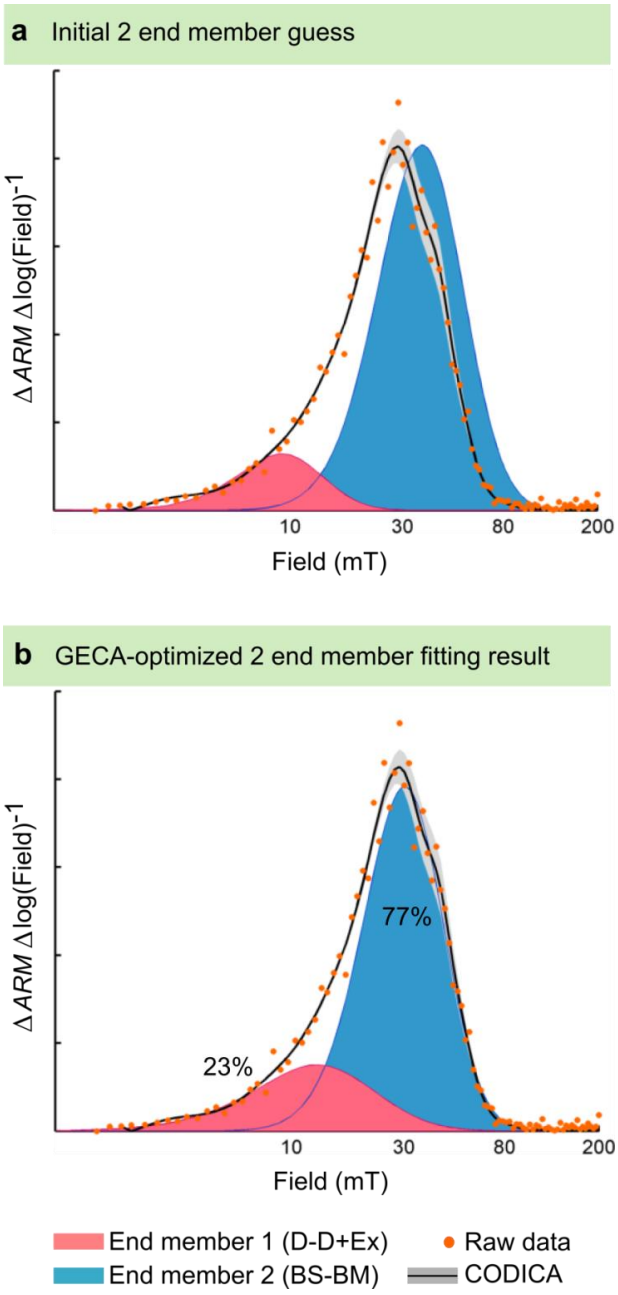

Supplementary Figure 2-10 | Parametric *ARM* coercivity spectra fitting for the surface sediment sample. (**a**) Initial "guess" for the 2 end members based on the optimized fitting result of *d*=3.9-7.0 m. (**b**) GECA optimized 2 end member fitting result (one iteration, *p* and *q* from both end members kept constant) from the initial parameters in (**a**). Orange dots: numerical derivative of raw data; Coercivity distribution (black thin line) and 95% confidence interval (grey thick line) calculated by CODICA from smoothed data. The percentages shown in (**b**) are the fractional contribution to the total *ARM* from each end member.

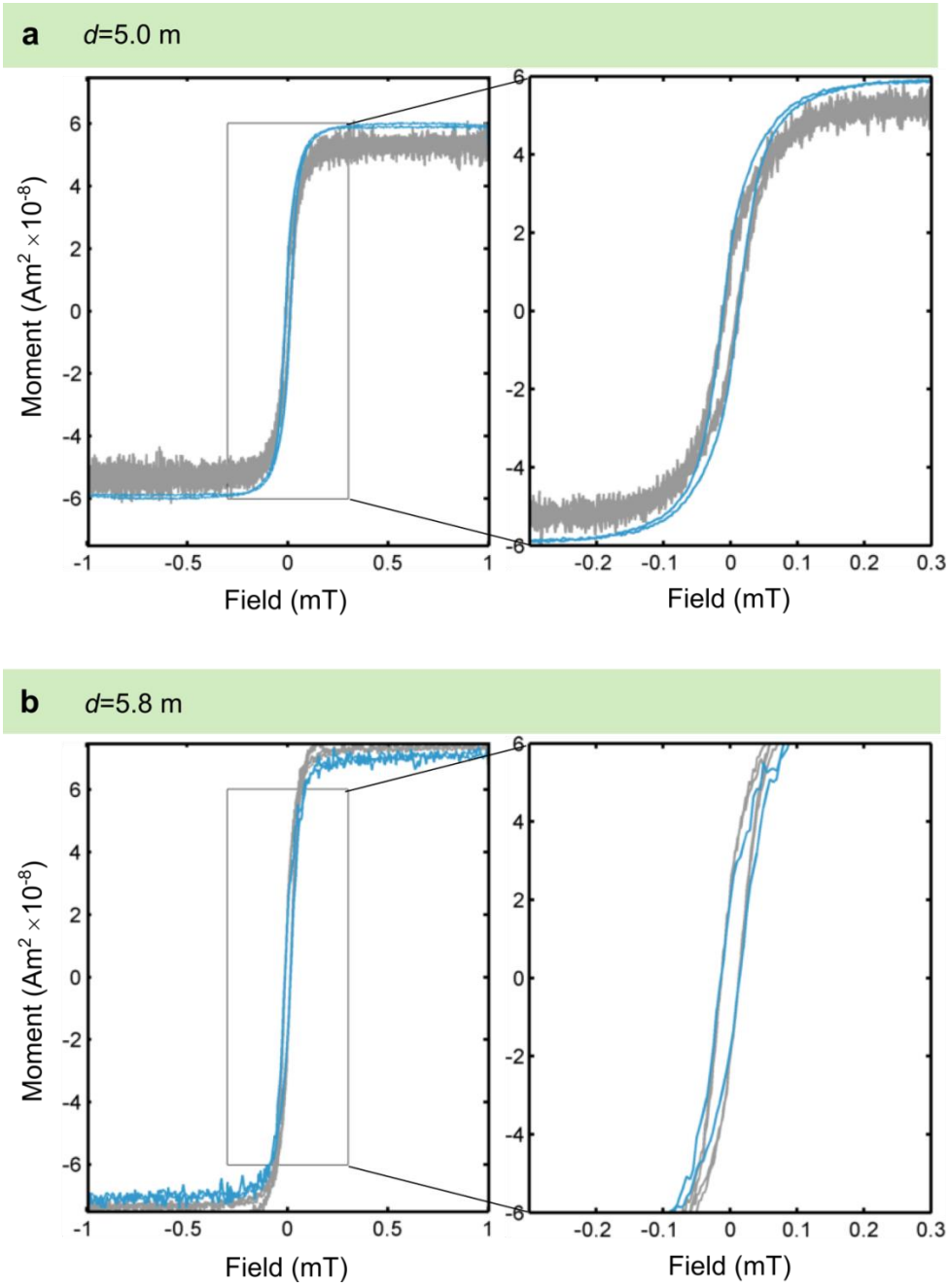

Supplementary Figure 2-11 | Angle dependent hysteresis loops. Zoomed (right) and full-scale (left) hysteresis loops acquired at two orientations. Grey and celestial blue curves denote hysteresis loops acquired with filter paper in-plane or orthogonal to the applied field, respectively, for filter stacks from (**a**) *d*=5.0 m, and (**b**) *d*=5.8 m.

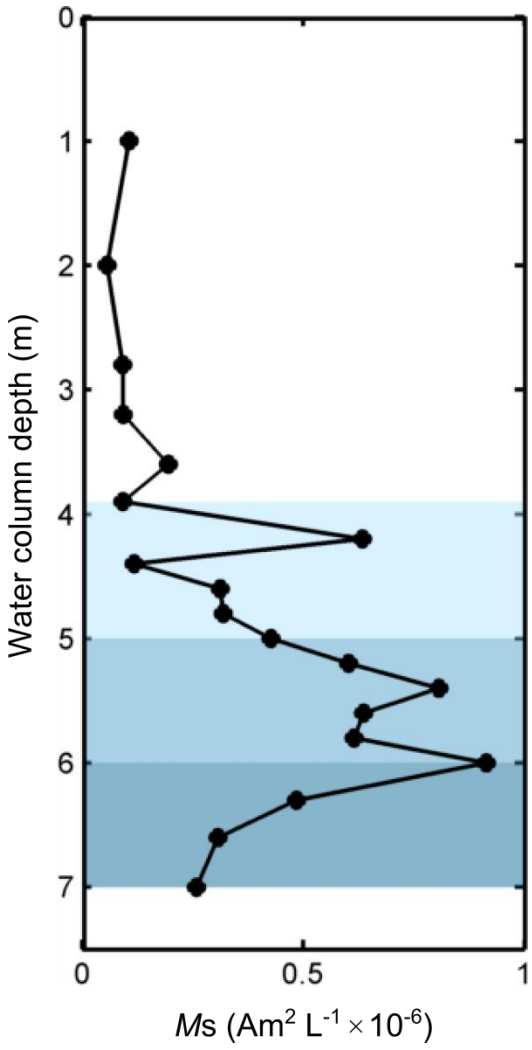

Supplementary Figure 2-12 | Saturation magnetization as a function of water column depths. Light, medium, dark shades of blue demarcate water column zones inhabited by magnetite MTB, mixed magnetite and greigite MTB, and greigite MTB, respectively (see text).

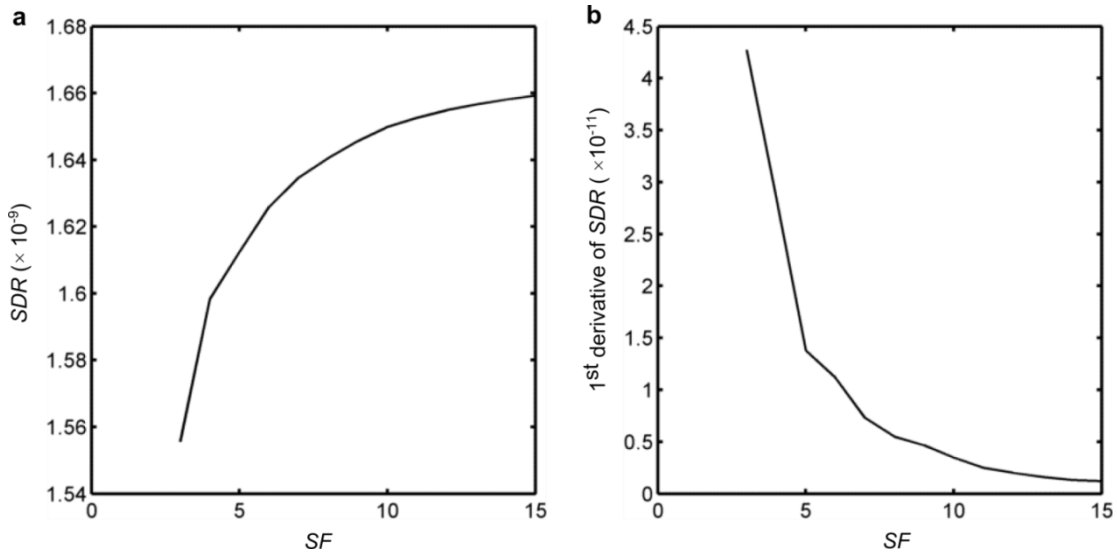

Supplementary Figure 2-13 | Optimal *SF* determination for equally spaced FORC *SF* grid. For FORC data acquired from *d*=6.6 m filter sample, (**a**) tricube weighted loess smoothing factor (*SF*) vs. standard deviation of residual (*SDR*) between averaged data and smoothed data and (**b**) *SF* vs. 1st derivative of *SRD*.

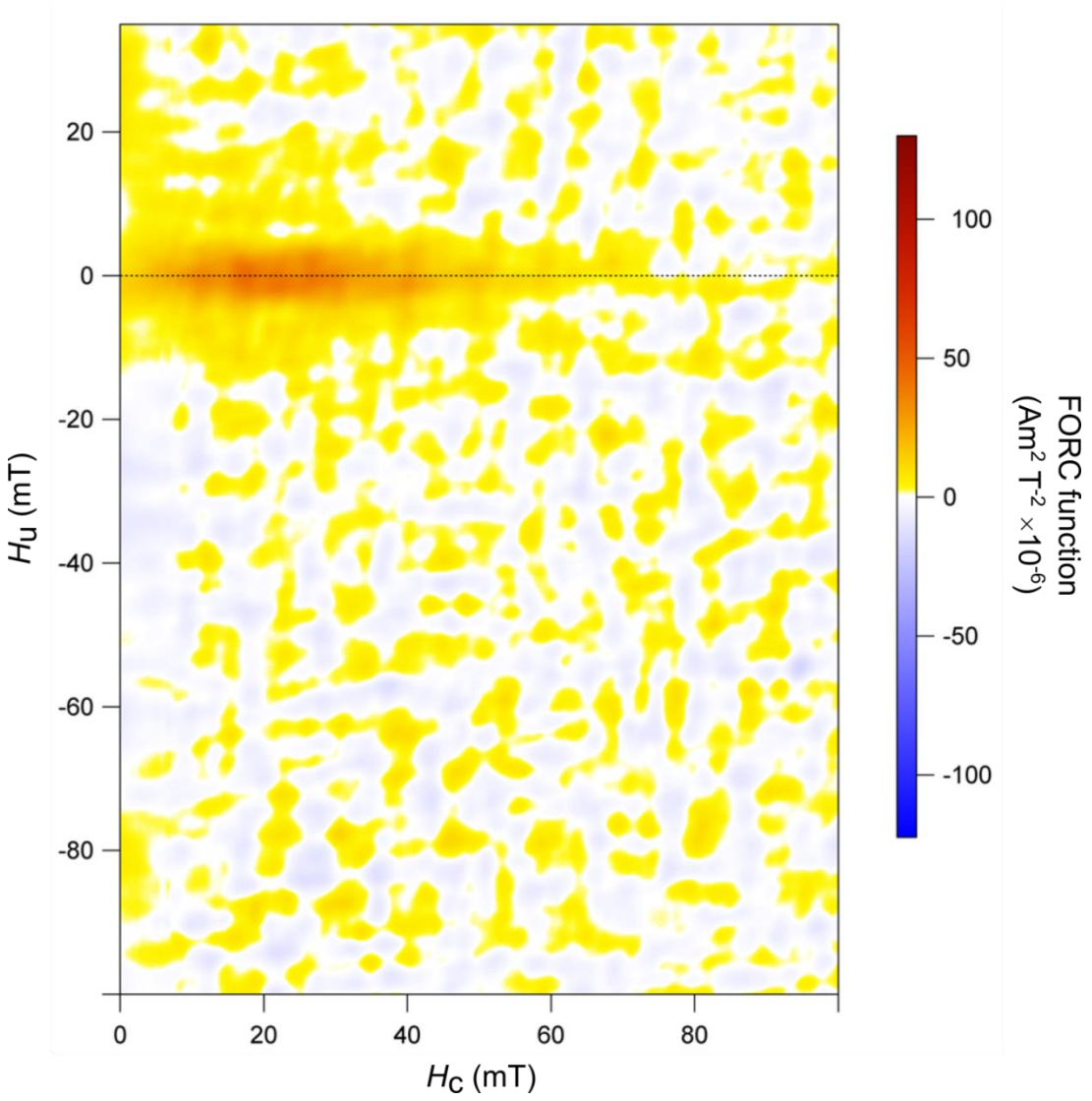

Supplementary Figure 2-14 | FORC diagram from greigite MTB. The measurement was made on filter containing >0.22 μm particulates in 330 mL of water collected from *d*=6.6 m. Five identical sets of raw data were averaged and processed with equally spaced smoothing grid, *SF*=15.

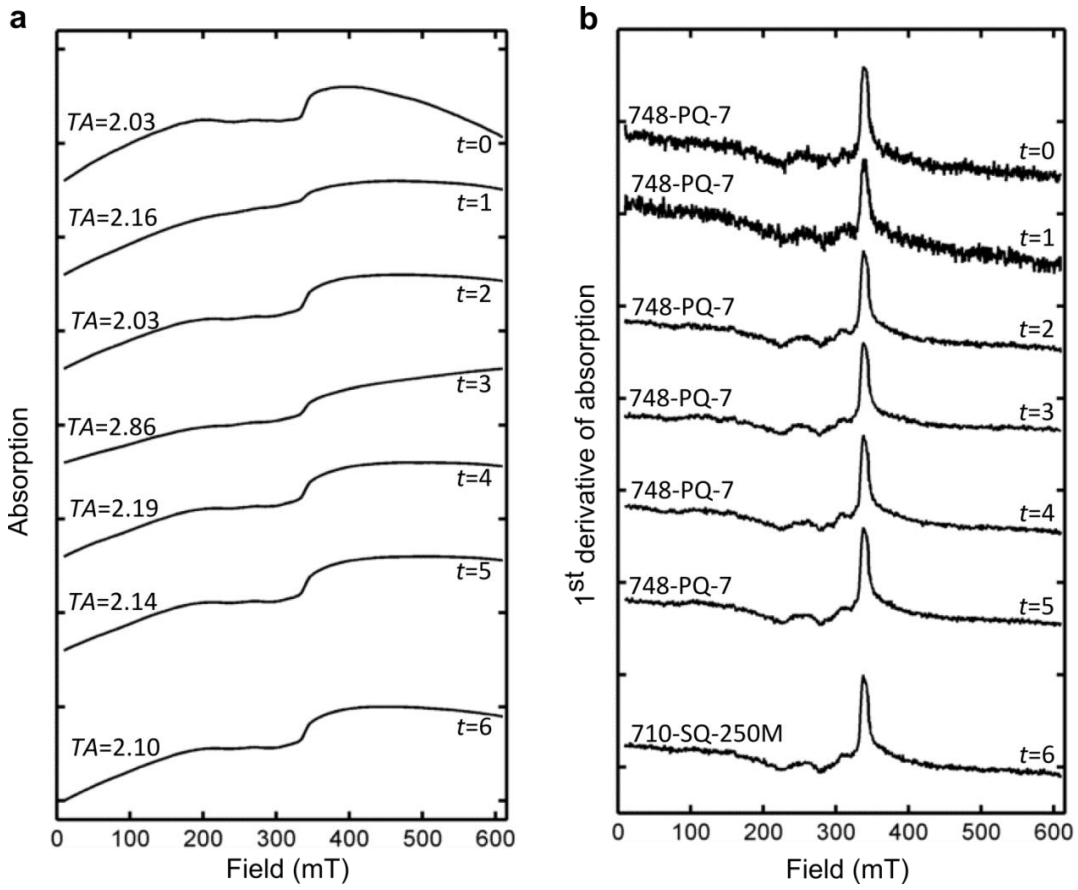

Supplementary Figure 2-15 | Contamination check of empty EPR tubes. (**a**) field vs. absorption (total absorption (*TA*) as indicated), and (**b**) field vs. 1st derivative of absorption. Time *t*=0 refers to the start of the experiment. The spectra at *t*=0 was measured from an empty EPR tube (Wilmad 748-PQ-7) plus a blank sample constructed from an un-used 0.22 µm filter with Elmer glue in the same manner as the water column and sediment trap samples. Spectra from all the other time stamps were measured from an empty EPR tube only. All water column samples and the sediment trap sample were measured with Wilmad 748-PQ-7 EPR tube, while the surface sediment sample was measured in the Wilmad 710-SQ-250M EPR tube.

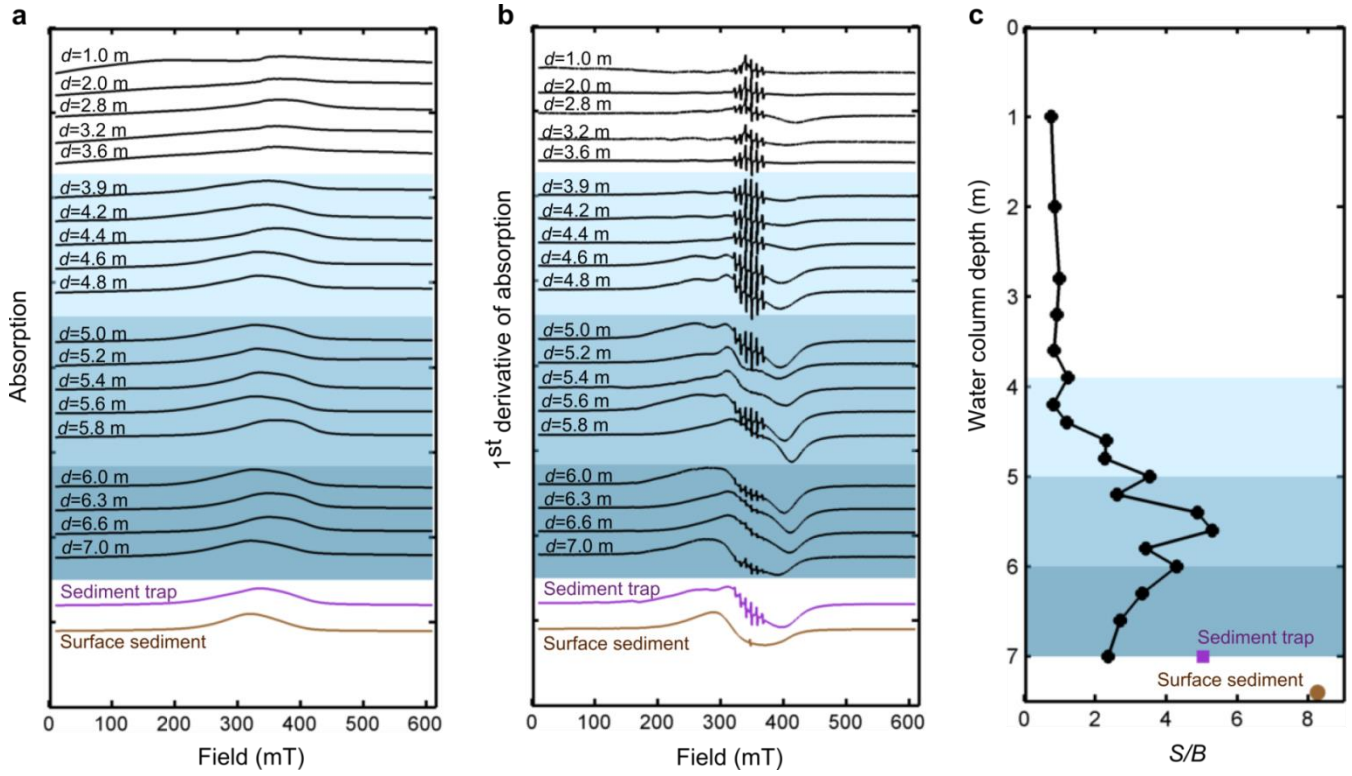

Supplementary Figure 2-16 | FMR data. FMR raw data (**a**) field vs. FMR absorption, (**b**) field vs. FMR 1st derivative of absorption shown in (**a**), (**c**) sample-to-blank (*S/B*) total absorption ratio. Both (**a**) and (**b**) are shown with compressed ordinate scaling. Light, medium, dark shades of blue demarcate water column zones inhabited by magnetite MTB, mixed magnetite and greigite MTB, and greigite MTB, respectively (see text).

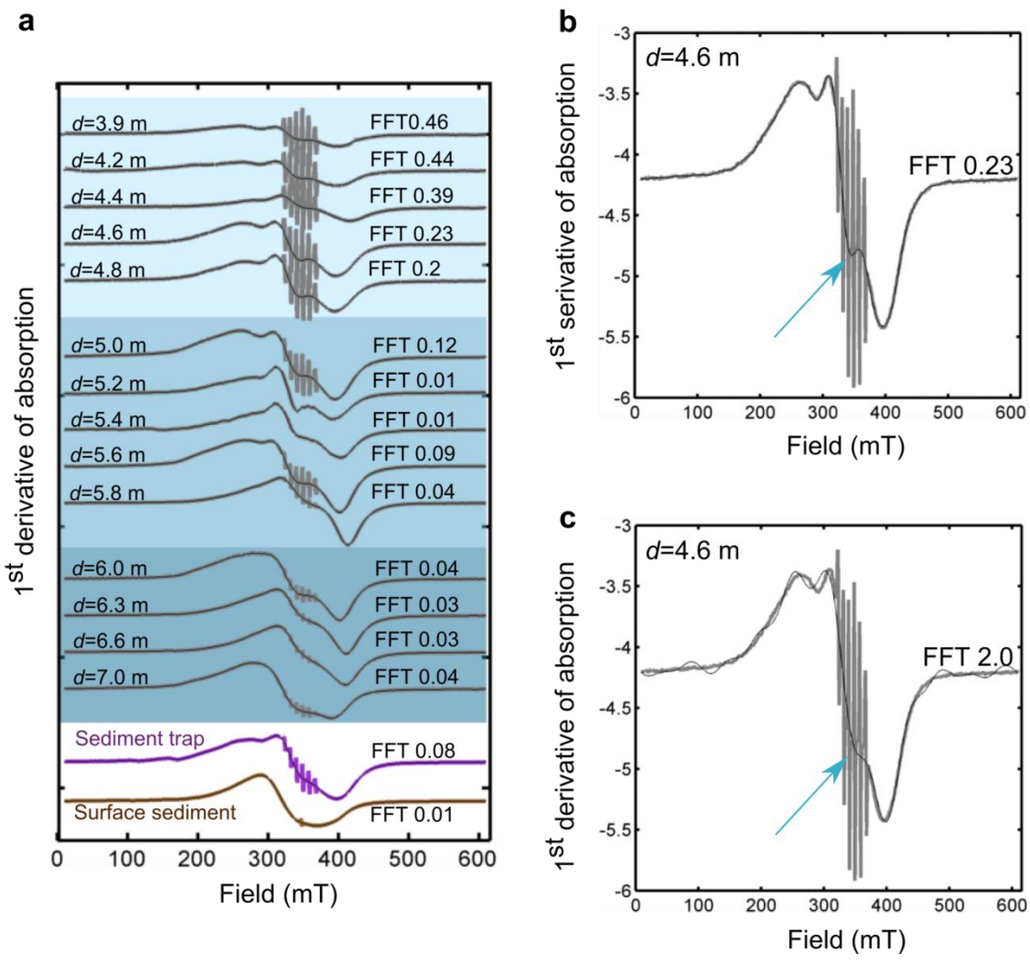

Supplementary Figure 2-17 | Processed FMR data. Blank subtracted and linear baseline drift corrected FMR data (**a**) field vs. 1st derivative of absorption with (black thin line) and without (grey thick/purple/brown thick line) FFT smoothing. The FFT values shown are the factors that were multiplied with the mean FFT frequency above which the data were smoothed out. (**b**, **c**) examples of different degree of FFT smoothing from *d*=4.6 m water column filter (black thin line: FFT smoothed data; grey thick line: unsmoothed data). The blue arrows point to a feature that is preserved in a less aggressive FFT smoothing (**b**) but lost in a more aggressive FFT smoothing (**c**). Notice that in a more aggressive FFT smoothing the misfit between smoothed and unsmoothed data is large everywhere. In (**a**), light, medium, dark shades of blue demarcate water column zones inhabited by magnetite MTB, mixed magnetite and greigite MTB, and greigite MTB, respectively (see text).

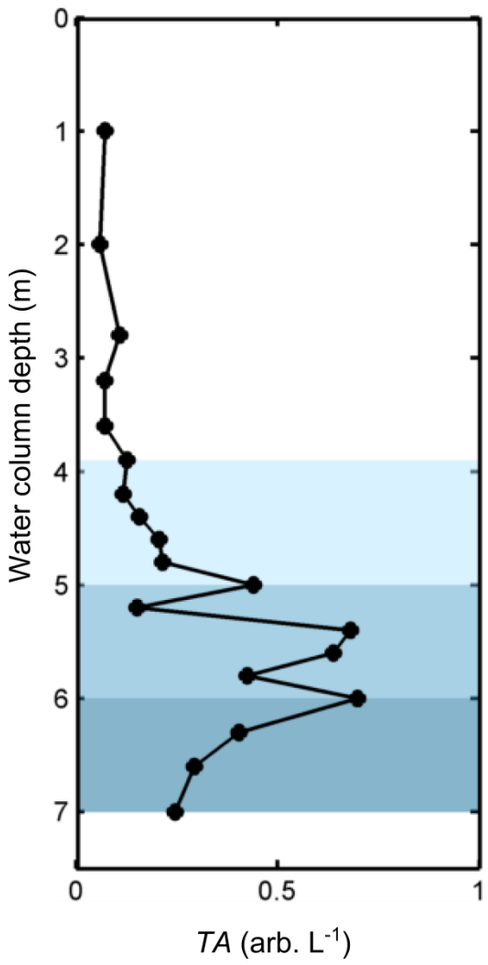

Supplementary Figure 2-18 | FMR total absorption as a function of water column depths. Light, medium, dark shades of blue demarcate water column zones inhabited by magnetite MTB, mixed magnetite and greigite MTB, and greigite MTB, respectively (see text).

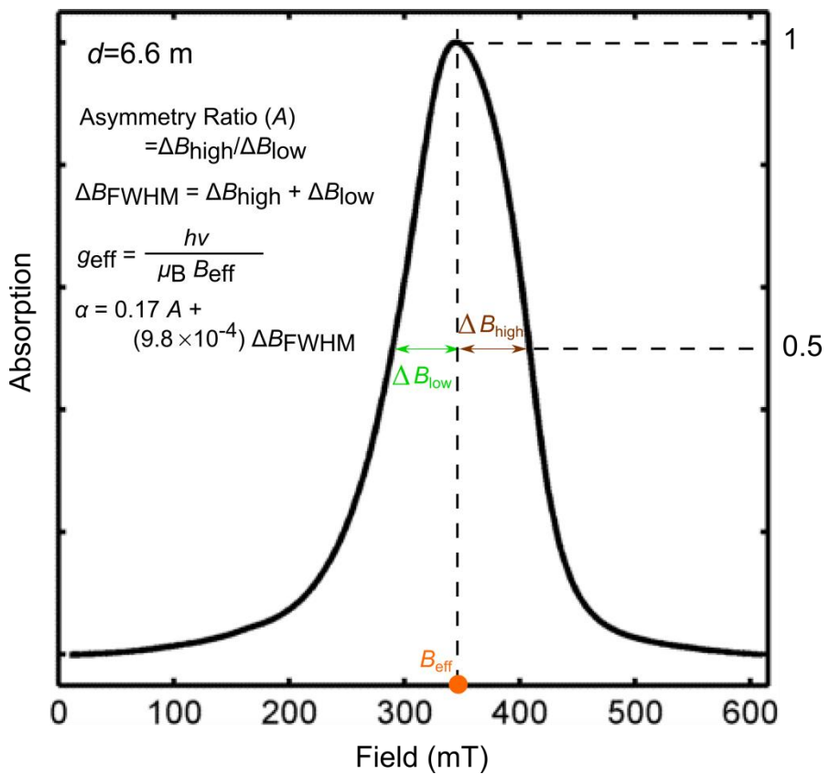

Supplementary Figure 2-19 | Schematic of empirical FMR parameters. All parameters are derived from the (blank subtracted, linear baseline corrected, FFT smoothed) FMR absorption spectra. Shown here is an example from d=6.6 m. For g_{eff}, h = 6.626 ×10^{-34} m^2 kg s^{-1} is the Planck's constant, v is the X-band microwave frequency, and μ_B = 9.274×10^{-24} J T^{-1} is the Bohr magneton. For this particular sample measured at 9.636 GHz, B_{eff}=344.6 mT, g_{eff} =2.01, ΔB_{low}=55.1 mT, ΔB_{high}=63.9 mT, asymmetry ratio (A)=1.16, and alpha (α)=0.314.

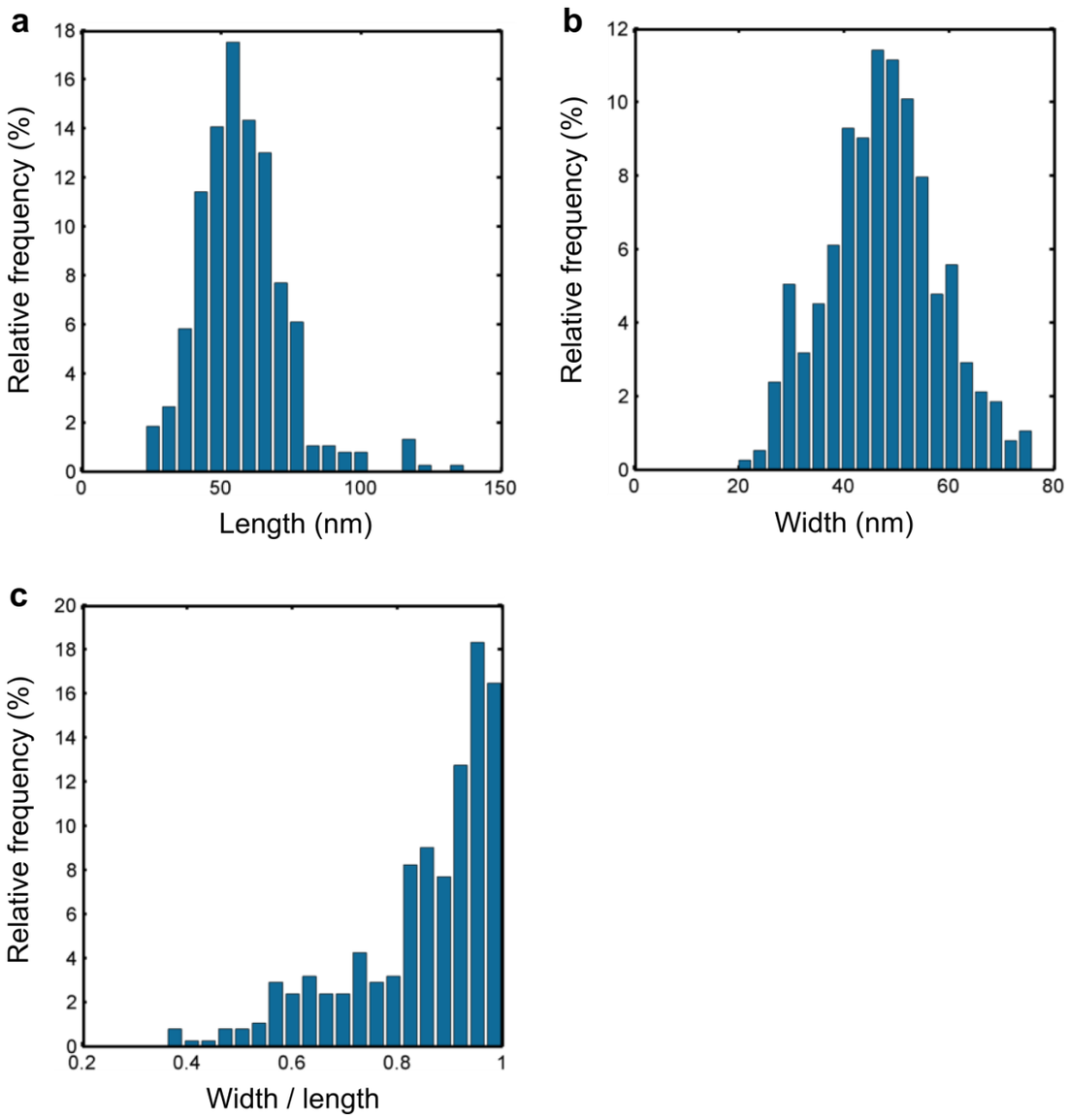

Supplementary Figure 2-20 | Magnetosome dimension.

Supplementary Tables

Supplementary Table 2-1| *ARM AF* demagnetization data smoothing parameters		
	robust loess span	**Mean misfit (%)**
**d*=4.2 m	0.24	2.43
d=4.4 m	0.21	1.32
d=4.6 m	0.08	0.85
d=4.8 m	0.09	0.83
**d*=5.0 m	0.15	3.51
d=5.2 m	0.12	2.85
d=5.4 m	0.09	1.89
d=5.6 m	0.11	1.90
d=5.8 m	0.1	1.99
d=6.0 m	0.09	1.95
**d*=6.3 m	0.09	4.62
**d*=6.6 m	0.19	6.86
**d*=7.0 m	0.13	7.74
d=3.9-7.0 m Average	0.15	1.84
*Sediment Trap	0.11	3.02
Surface Sediment	0.15	1.65
*Raw and robust smoothed data for these six samples with the largest mean misfit are shown in Supplementary Fig. 7.		

Supplementary Table 2-2| Coercivity distribution parameters														
	[1]*MF*	[2]Fitting field range	GECA 1 skewed Gaussian end member					GECA 2 skewed Gaussian end members						
	(mT)	(mT)	*μ*	*σ*	*q*	*p*	χ^2/DF [Confidence Interval]	End member	% Contribution	*μ*	*σ*	*q*	*p*	χ^2/DF [Confidence Interval]
d=4.2 m	33.0	1.6 – 116.4	1.538	0.2417	0.5747	1.868	3.5 [0.27 – 2.1]	1	8.2%	0.9433	0.2704	0.6866	1.909	4 [0.0039 – 3.8]
								2	92%	1.556	0.1997	0.7443	1.97	
d=4.4 m	32.23	1.6 – 116.4	1.528	0.2241	0.5964	1.814	2.7 [0.34 – 1.9]	1	7.8%	0.9433	0.2757	0.6866	1.909	1.6 [0.34 – 1.9]
								2	92%	1.544	0.1939	0.7443	1.97	
d=4.6 m	32.02	1.6 – 120.8	1.524	0.2087	0.6251	1.825	0.81 [0.39 - 1.8]							
d=4.8 m	32.30	1.6 – 120.8	1.529	0.1875	0.693	1.911	1.3 [0.34 – 1.9]							
d=5.0 m	32.35	1.6 – 125.3	1.529	0.185	0.7231	1.949	2.4 [0.39 – 1.8]	1	3.9%	0.8308	0.2266	0.6866	1.909	1.2 [0.39 - 1.8]
								2	96%	1.531	0.1783	0.7443	1.97	
d=5.2 m	33.06	1.6 – 125.3	1.539	0.1835	0.7251	2.022	1.7 [0.39 – 1.8]							
d=5.4 m	33.70	1.6 – 116.4	1.547	0.1825	0.7126	1.943	1.7 [0.39 – 1.9]							
d=5.6 m	34.75	1.6 – 116.4	1.559	0.1784	0.6743	1.905	1.4 [0.34 -1.9]							
d=5.8 m	35.22	1.6 – 116.4	1.562	0.1765	0.6845	1.951	1.3 [0.34 – 1.9]							
d=6.0 m	33.77	1.6 – 197.7	1.544	0.1815	0.6669	1.929	0.89 [0.34 – 1.8]							
d=6.3 m	31.52	1.6 – 130.3	1.513	0.1974	0.6293	1.826	0.77 [0.44 – 1.8]							
d=6.6 m	29.57	1.6 – 125.3	1.483	0.2047	0.6133	1.634	1.2 [0.34 – 1.9]							
d=7.0 m	27.72		1.455	0.2631	0.5746	1.947	0.62 [0.34 – 1.8]							
[3]*d*=3.9-7.0 m Average	33.04	1.6 – 120.8	1.53± 0.034	0.20± 0.026	0.66± 0.048	1.89± 0.11	1.5 [0.27 – 2.1]	1	5.4%	0.9433	0.196	0.6866	1.909	1.2 [0.27 - 2.1]
								2	95%	1.545	0.1909	0.7443	1.97	
Sediment trap	33.15	1.6 – 116.4	1.535	0.218	0.702	2.172	1.2 [0.42 – 1.8]							
Surface sediment	25.17	1.8 – 200.0	1.409	0.2771	0.4985	1.896	0.77 [0.42 – 1.8]	1	23%	1.077	0.2787	0.6866	1.909	0.69 [0.45 – 1.7]
								2	77%	1.466	0.1784	0.7443	1.97	
[4]Average *ARM* D-D+Ex (*n*=28)			1.346±0 .072	0.335 ± 0.042	0.771±0 .144	1.838±0 .105								
[4]Average *ARM* BS-BM (*n*=24)			1.636±0 .040	0.191± 0.023	0.750±0 .091	1.994±0 .030								
[4]Average *ARM* BH-BI (*n*=26)			1.838±0 .046	0.122± 0.037	0.739±0 .132	1.994±0 .066								

[1]Median field (*MF*) calculated by CODICA
[2]The range of field considered significant by GECA
[3]These average ± standard deviation does not include *d*=4.2-4.4 m nor *d*=5.0 m results
[4]Average ± standard deviation from ref. 3

Supplementary Table 2-3| Hysteresis and FORC measurement parameters

	Hysteresis	FORC	
Field sweep mode	Continuous; *Automatic		Continuous
Averaging time	100 ms;*1 sec		100 ms
Vibration amplitude	*1.0		
H-maximum	1.0 T;*1.5 T	H-saturation	1.5 T
H-increment	3 mT;*5 mT		0.7 mT
Pause at -1.0 T/*-1.5 T	1.0 sec	Pause at *H*-calibration	200 ms
		Pause at *H*-reversal field	200 ms
		H_c	0 – 100 mT
		H_u	-100 – 35 mT
Acquisition time	2.30 min.;*25.18 min.		3.44 hr

*For the surface sediment sample measured on VSM only

Supplementary Table 2-4| Hysteresis parameters			
	# Measurements	***M*s (n Am^2 L^{-1})**	**[3]Average Q_f**
d=1.0 m	3	106.2 ± 9.2	1.5
d=2.0 m	[1]3	56.3 ± 10.7	0.3
d=2.8 m	3	91.7 ± 4.9	0.7
d=3.2 m	3	92.8 ± 23.6	0.4
d=3.6 m	6	194.8 ± 11.9	1.2
d=3.9 m	5	92.0 ± 7.04	0.6
d=4.2 m	[2]6	632.8 ± 901.4	0.6
d=4.4 m	6	117.5 ± 12.6	0.6
d=4.6 m	6	311.9 ± 46.4	0.8
d=4.8 m	6	318.8 ± 34.1	1.3
d=5.0 m	6	426.4 ± 6.4	1.3
d=5.2 m	3	601.7 ± 12.0	1.9
d=5.4 m	3	805.7 ± 32.5	1.7
d=5.6 m	3	635.6 ± 36.3	1.5
d=5.8 m	3	614.2 ± 28.8	1.5
d=6.0 m	3	912.7 ± 13.3	1.8
d=6.3 m	3	484.0 ± 30.6	1.4
d=6.6 m	3	306.7 ± 14.9	0.9
d=7.0 m	3	319.4 ± 8.5	1.0
		(n Am^2 Day^{-1})	
Sediment trap	3	139.8 ± 4.0	2.0
		(Am^2 kg^{-1})	
*Surface sediment	4	0.02814 ± 0.00213	2.4

[1]One measurement with slope corrected negative *M*s excluded in the average and standard deviation

[2]Three measurements with slope corrected negative Ms excluded in the average and standard deviation

[3]Q_f is a data quality indicator and is a measure of the signal to noise ratio (Q_f= log10(*s/n*)) in the hysteresis loop defined in ref. 4

Supplementary Table 2-5| FMR Parameters					
	Frequency (GHz)	**Power (mW)**	**# of scan averaged**	**Field range (mT)**	**Field increment (mT)**
*Water column (*d*=2.0 – 7.0 m)	9.69 ± 0.0021	2.01± 0.002	4 †2	10 – 609.4	0.58
Sediment trap	9.69	2.01	4		
Surface sediment	9.75	0.02	4		
*Reported here are averages and associated standard deviations of frequency and power †For *d*=6.0 m only					

Supplementary Table 2-6| FMR empirical parameters					
	g_{eff}	B_{eff} (mT)	ΔB_{FWHM} (mT)	Asymmetry ratio (*A*)	α
d=3.9 m	2.11	328.2	152.3	0.844	0.293
d=4.2 m	2.11	328.8	148.8	0.801	0.282
d=4.4 m	2.00	348.7	138.9	1.10	0.323
d=4.6 m	2.11	328.8	132.4	0.95	0.291
d=4.8 m	2.10	329.3	126.0	1.01	0.295
d=5.0 m	2.12	327.0	141.8	0.88	0.288
d=5.2 m	2.10	329.3	109.0	1.11	0.296
d=5.4 m	2.08	333.4	117.8	1.31	0.338
d=5.6 m	2.12	326.4	138.3	1.02	0.308
d=5.8 m	1.94	356.9	121.3	0.93	0.278
d=6.0 m	2.12	326.4	135.4	1.06	0.313
d=6.3 m	2.01	344.6	123.6	1.15	0.317
d=6.6 m	2.01	344.6	118.9	1.16	0.314
d=7.0 m	2.17	319.4	124.2	1.02	0.295
Sediment trap	2.07	334.0	128.3	0.90	0.279
Surface sediment	2.18	320.0	103.7	1.06	0.282

Supplementary Table 2-7: MTB turnover time				
	ARM	***IRM*** **($Am^2 m^{-2}$)**	***M*s**	**FMR** **(arb. m^{-2})**
d=3.9 – 7.0 m depth integrated Signal	6.3289×10^{-5}	4.48×10^{-4}	0.0015	1.0881×10^{3}
[1]Sediment trap signal		**($Am^2 day^{-1} m^{-2}$)**		**(arb. $day^{-1} m^{-2}$)**
	3.3296×10^{-6}	1.6054×10^{-5}	4.5668×10^{-6}	41.6495
Turnover time (days)	19.0	27.9	40.3	26.1
Turnover time average = 28.3 days or 12.9 times per year				
[1]Using sediment trap cross sectional area = 0.0038 m^2				

Supplementary Table 2-8| Magnetite vs. greigite magnetosome flux		
	Depth integrated *ARM* signal ($Am^2 m^{-2}$)	
	As magnetite	As greigite
d=3.9 – 5.0 m	1.220×10^{-5}	0
d=5.0 – 6.0 m	1.607×10^{-5}	1.607×10^{-5}
d=6.0 – 7.0 m	0	1.895×10^{-5}
Total	2.827×10^{-5}	3.502×10^{-5}
	($Am^2 yr^{-1} m^{-2}$)	
[1]Expected magnetosome flux in sediment	3.640×10^{-4}	4.510×10^{-4}
[2]Expected remaining after 12.5 years (average)	$(1.540 – 3.232)\times10^{-4}$	?
[3]Actual sediment magnetosome flux	3.45×10^{-4}	
[1]Using MTB turnover time average of 12.9 times per year from Supplementary Table 7 [2]Applying known magnetite dissolution rate law in ref. 5, see text [3]Estimated from *ARM* coercivity 2-component un-mixing, see Supplementary Fig. 10 and text		

Supplementary Methods

Coercivity distribution data processing by CODICA and GECA.

The overall coercivity distribution on a log-scale used for coercivity distribution analyses was determined from blank subtracted *ARM* vs. *AF*. For water column samples, demagnetization spectra between *d*=4.2 and *d*=7.0 m were taken to be the moving average of three depths: *e.g.*, *d*=4.2 m ARM spectra was taken as the average from *d*=3.9 m, *d*=4.2 m, *d*=4.4 m, and *d*=7.0 m *ARM* spectra was taken as the average from normalized *d*=6.6 m, *d*=7.0 m, *d*=7.4 m, *etc*. The averaged data from the water column samples, sediment trap samples, and surface sediment samples were smoothed by the robust loess (rloess) method in MATLAB. The rloess span and misfit, generally small, between smoothed and un-smoothed data are summarized in Supplementary Table 1 and examples are shown in Supplementary Fig. 7. Next, the averaged and smoothed data was used as input for COercivity DIstribution CAlculator (CODICA; version 5.1)[6]. CODICA calculated median fields (*MF*) for the overall coercivity distributions are summarized in Supplementary Table 2. The software suggested exponent for the power function used for AF demagnetization field scale transformation prior to linearization is always accepted. All data outliers that fall more than 3 standard deviations away from the software estimated average error are removed. The software suggested correlation length of the residual (between input data and the fitted power function), used in the least-square collocation for final error estimate, is also used for all samples. It is important to note here that neither the outlier removal nor the choice of correlation length is standardized and the user is given full control over both in CODICA. We have chosen to average and smooth the *ARM* coercivity spectra prior to inputting the data into CODICA and use the CODICA suggestions as stated above as it is not always clear by looking at the residual curve what the desirable correlation length (*i.e.* scale of the smallest detail) should be. Instead, we compared the robust loess smoothed and unsmoothed averaged data visually and report the mean misfit (Supplementary Table 1). CODICA detected non-monotonic behavior in the majority of the samples analyzed at *AF*>~100 mT. These are taken to be artifacts, evident from the low *S/B* ratio and large scatter (Supplementary Fig. 5b-c) between *AF* ~100-200 mT. Examples from six samples analyzed are given in Supplementary Fig. 7.

Parametric curve fitting and coercivity distribution un-mixing were calculated by GEneralized Coercivity Analyzer (GECA; version 2.1). GECA employs a flexible skewed generalized Gaussian (SGG) distribution to describe an end-member:

$$SGG(x, \mu, \sigma, q, p) = \frac{1}{2^{1+\frac{1}{p}}\,\sigma\,\Gamma(1+\frac{1}{p})} \frac{|qe^{qx'}+q^{-1}e^{x'/q}|}{e^{qx'}+e^{x'/q}} exp\left[-\frac{1}{2}\left|\ln\left(\frac{e^{qx'}+e^{x'/q}}{2}\right)\right|^{p}\right] \quad (1)$$

where $x' = \frac{(x-\mu)}{\sigma}$, x = log (AF), σ>0, 0<|q|≤1, and p>0. The shape of SGG is controlled by μ, σ, q, and p, where 10^{μ} is the distribution median (in mT), σ, q, and p are related to the width, skewness, and kurtosis of the distribution, respectively. A symmetric Gaussian is a special case of SGG with q=1 and p=2. Since we expected majority of the *ARM* signal to be carried by magnetosomes for the water column samples between d=4.2 and d=7.0 m and for the sediment trap sample, we started by fitting these samples with one end-member only. Coercivity distribution on the log-scale calculated by CODICA was used as input for GECA, and the optimization was performed on the entire range of fields considered significant by GECA (Supplementary Table 2). We used a starting set of distribution parameters that loosely approximate the CODICA calculated distribution and allowed GECA to optimize all five parameters (amplitude (a), μ, σ, q, p) at once.

The statistical significance of the one end-member fitting result is evaluated by GECA by the Pearson's χ^2 test, whereby a 95% confidence interval is given by the weighted mean square residual (between fitted coercivity distribution and those measured and calculated by CODICA) divided by the degree of freedom (DF), the latter of which is taken by the software to be equal to one plus the number of zero crossing of the residual that tend to oscillate around zero. Aside from d=4.2, d=4.4, and d=5.0 m, χ^2/DF falls within the estimated 95% confidence interval for all samples modeled with one end-member. The results are summarized in Supplementary Table 2.

For samples with χ^2/DF > 95% confidence interval maximum (d=4.2, d=4.4, and d=5.0 m), GECA suggests that more end-members should be added to better approximate the measured and CODICA calculated coercivity distribution. However, it is not clear what the additional end-member should be or how many there should be, as there are no clear "bumps" in the coercivity distribution on linear-, log-, and power-field scale that can be suggestive of multiple components[2] (Supplementary Fig. 8). Instead, as these water column samples may contain minor amount of allochthonous material, we performed the fitting again with an additional end-member that is similar to the interpreted detrital particle end-member (D-D+Ex) in ref. 3. This coercivity end-member is thought to have a distribution that overlaps with extracellularly (Ex) produced magnetic particles from biologically induced mineralization[2]. The initial parameters (10 in total) needed for the 2-end member parametric fitting was obtained by first fitting the coercivity distribution calculated by CODICA from averaged and robust loess smoothed (rloess span 0.15; mean misfit 1.84%) *ARM* coercivity

spectra from water depth between d=3.9-7.0 m. The source of the allochthonous material should be similar for all water column samples, and averaging helps to improve the signal-to-noise ratio to better constrain the parameter estimation. Since the majority of the water column sample can be described by one end-member that is similar to BS-BM in ref. 3 and we wanted to test if the coercivity distribution fitting can be improved by the addition of an allochthonous end-member, we used the averaged SGG μ, σ, q, and p parameters for *ARM* for BS-BM and D-D+Ex from ref. 3 (Supplementary Table 2) as the initial fitting parameters. The initial amplitudes for the two end-members are adjusted so the linear combination of the two have approximately the same amplitude as the overall coercivity distribution calculated by CODICA as shown in Supplementary Fig. 9a. At this point in the curve fitting, GECA asks the user for input for the optimization procedure. For a two end-member parametric fitting, the user has the choice of holding any combinations of 10 variables constant at each optimization iteration (2 sets of a, μ, σ, q, and p) for as many iterations as the user chooses. We went through five optimization iterations by changing one of the five parameters, μ, a, σ, p, and q, at a time for both end-members (*i.e.* 2 parameters at a time in order listed) while holding others constant at every iteration. The fitting result is shown in Supplementary Fig. 9b. The χ^2/DF after five optimization iterations is within the 95% confidence interval estimated by GECA, and the parameters are listed in Supplementary Table 2.

The parameters (μ, σ, q, and p from each end-member) from the averaged d=3.9-7.0 m un-mixing using two end-members were then used as the initial parameter to un-mix the three samples (d=4.2, d=4.4, and d=5.0 m) that did not pass the Pearson's χ^2 test previously when fitted with only one SGG. Again, the initial amplitudes of the two end-members were adjusted such that the linear combination of them loosely approximates the amplitude of the CODICA calculated coercivity distribution (Supplementary Fig. 9a). The optimization was performed with one iteration by holding p and q constant for both end-members. The results are shown in Supplementary Fig. 9b. From this analysis, two of them (d=4.4 and d=5.0 m) had χ^2/DF within 95% confidence interval while d=4.2 m still shows χ^2/DF>95%. Since d=4.2 m shows considerable scatter in its distribution calculated from the averaged and smoothed data (orange dots in Supplementary Fig. 7a) and we do not have any information about what a third end-member might be, we stopped the analyses here for this sample. The contribution for end-member 1 and 2 to the total ARM signal for each sample was taken as the fractional contribution of each end-member to the linear combination of the two combined. The results are summarized in Supplementary Table 2, and the component resembling BS-BM accounts for 92% and 96% of the ARM signal for d=4.4 and d=5.0 m, respectively. For simplicity and clarity, the blue curves in Fig. 6a includes SGG functions

representing *ARM* coercivity distribution from all Upper Pond water column depth between *d*=3.9–7.0 m except for *d*=4.2, 4.4, 5.0 m.

We observe from the one end-member fitting result of the surface sediment sample that, while statistically significant (*i.e.* χ^2/DF within 95% confidence interval estimated in GECA), it has a much larger σ of 0.28 compare to the range (0.18-0.22) spanned by the water column samples. This is expected as the surface sediment, having been accumulated for ~12.5 years, would contain not only the water column magnetosome input but also allochthonous material and/or extracellularly produced magnetic particles typified by a larger variance (*ARM* D-D+Ex average σ=0.335±0.042 in ref. 3). As such, we fitted the surface sediment sample with 2 SGG end-members in the same manner as for *d*=4.2, *d*=4.4, and *d*=5.0 m described above (Supplementary Fig. 10, Supplementary Table 2). The resulting χ^2/DF is still within 95% confidence interval estimated in GECA.

An example of MTB population turnover rate determined from the *IRM* results

From the *IRM* depth profile (Fig. 1e), we arrived at the depth-integrated signal of 4.48×10^{-4} Am^2 m^{-2}. Because live MTB were observed between *d*=3.9 m, and *d*=7.0 m, we only integrate between these two limits. We can find out how fast dead MTB get exported out of *d*=3.9 –7.0 m by using the *IRM* signal from the sediment trap we installed at *d*=7.0 m over a period of 10 days. The sediment trap *IRM* signal amounts to 1.6054×10^{-5} Am^2 day^{-1} m^{-2}, calculated by taking the measured sediment trap *IRM* signal (6.1517×10^{-7} Am^2) divided by the number of collection day (10; as stated in Methods) and the sediment trap cross sectional area (0.0038 m^2; sediment trap cylinder inner diameter stated in Methods). Then we calculated how many days would be required for a sediment trap installed at *d*=7.0 m to accumulate the depth-integrated MTB *IRM* signal:

$$\frac{4.48\times10^{-4}\ Am^2m^{-2}}{1.6054\times10^{-5}Am^2m^{-2}day^{-1}} = 27.9\ days \quad (2)$$

Supplementary References

1. How can you see them, http://www.biophysics.uwa.edu.au/STAWA/magbac_4.html
2. Competitive edge, http://www.spectrumlabs.com/filtration/Edge.html
3. Egli, R. Characterization of Individual Rock Magnetic Components by Analysis of Remanence Curves, 1. Unmixing Natural Sediments. *Stud. Geophys. Geod.* **48,** 391–446 (2004).
4. Jackson, M. & Solheid, P. On the quantitative analysis and evaluation of magnetic hysteresis data. *Geochem. Geophys. Geosys.* **11,** (2010).

5. Canfield, D. E. & Berner, R. A. Dissolution and pyritization of magnetite in anoxic marine sediments. *Geochim. Cosmochim. Acta.* **51,** 645–659 (1987).
6. Egli, R. Analysis of the field dependence of remanent magnetization curves. *J. Geophys. Res.* **108,** (2003).

Chapter 3

Rotational- and Gyro-remanent magnetization of magnetosomes

A. P. Chen[1], D. K. Potter[2], M. K. Chan[3], C-S. Horng[4], D. A. Bazylinski[5]

Author affiliations

[1] Department of Environment & Geography, Macquarie University, North Ryde, New South Wales, Australia.

[2] Department of Physics, University of Alberta, Edmonton, Alberta, Canada.

[3] Department of Physics, University of Minnesota, Minneapolis, Minnesota, USA.

[4] Institute of Earth Sciences, Academia Sinica, Nankang, Taipei, ROC, Taiwan.

[5] School of Life Sciences, University of Nevada at Las Vegas, Las Vegas, Nevada, USA.

Correspondence should be addressed to A.P.C. (email: AmyPChen012s@gmail.com).

Author contributions

A.P.C. initiated the project, collected the samples, conducted the measurements, provided the interpretations, and drafted the manuscript. D.K.P. advised on the RRM measurements and data interpretations. M.K.C. assisted in MMP sample collection. C-S.H. provided the EJC specimens. D.A.B. provided the cultured MTB specimens. All authors participated in discussion and manuscript revision.

Prepared for submission to *Geophysical Research Letters*.

3.1 Abstract

Two types of gyromagnetism experiments were performed on samples containing uncultivated and cultivated magnetite– and greigite–magnetosome producing magnetotactic bacteria (MTB). We found that magnetosomes, despite being within the single-domain (SD) size range, uniformly acquire negligible rotational– and gyro–remanent magnetization. This observation may be explained by the chain or chain-like magnetosome arrangement, which effectively limits the number of stable moment orientations that are conducive to retaining deflected moment during switching by the externally applied magnetic field. Marginally higher effective gyrofield is obtained for samples (lysed MTB cultured cells and sediment that potentially contain lysed uncultivated MTB cells) affected by dipolar interaction, which may explain the large gyrofield typically associated with highly interacting SD greigite particles arranged in framboidal form. Lastly, the markedly low gyroremanence acquired by greigite magnetosomes compared to authigenic greigite framboid–bearing sediments further implicates structural defects as a limiting factor of gyroremanence acquisition.

3.2 Introduction

The remanent magnetization acquired by rocks and minerals after they have been rotated in the presence of an alternating field (AF), termed rotational remanent magnetization (RRM), was first systematically investigated by Wilson and Lomax [1972]. Except for a schist specimen containing millimeter-sized magnetite crystals, an igneous rock with very low paleomagnetic stability, and two high coercivity specimens (synthetic hematite and olivine with highly magnetic intergrowth), all the other igneous rocks and a synthetic magnetite specimen they tested acquired detectable RRM at low rotation rates of 0.002 to 3 r.p.s. Since then various geological materials and rock types have been shown to be capable of acquiring RRM (at varying, though generally low, rotation rates), including quartz dolerite [Edwards, 1982b], basalt [Brock and Iles, 1974; Roperch and Taylor, 1986; Madsen, 2004], serpentinite [Roperch and Taylor, 1986], sill with exolved magnetite [Madsen, 2004], siltstone [Brock and Iles, 1974], loess [Roperch and Taylor, 1986], mudstones [Sagnotti and Winkler, 1999], tuffaceous silts [Brock and Iles, 1974], lake and marine sediments [Snowball, 1997; Stephenson and Snowball, 2001; Hu et al., 2002; Madsen, 2004], sandstone [Shi and Tarling, 1999], pottery [Mahon and Stephenson, 1997], as well as an exoskeleton from a gastropod containing iron-sulphide [Suzuki et al., 2006]. There have been several systematic RRM studies on ferrimagnetic minerals such as magnetite [Edwards, 1980, 1982a; Potter and Stephenson, 1986; Snowball, 1997; Madsen, 2004], maghemite [Potter and Stephenson, 1986;

Stephenson and Potter, 1987; Edwards and Desta, 1989], greigite [Snowball, 1997], chromium dioxide [Madsen, 2003], and pyrrhotite [Thomson, 1990]. Moreover, Noel [1988] showed that it is possible to impart a RRM on a stationary sample by applying a rotating direct field, while Stephenson [1988] showed that rotating samples exposed to a stationary, decreasing direct field can also acquire RRM. The RRM acquired as a function of rotation speed, sense of rotation, field amplitude, and the angle between the applied field and the rotation vector depend on magnetic particle size and mineralogy. For similar concentrations, stable single-domain (SSD) and pseudo-single-domain (PSD) magnetite (Fe_3O_4) acquire a higher RRM than their multi-domain (MD) counterpart [Potter and Stephenson, 1986]. The largest effective gyrofield (B_g) measured to-date has come from a sediment sample containing clusters (framboids) of octahedral greigite (individual particle size ~1 μm) [Stephenson and Snowball, 2001].

An association between RRM and gyromagnetism was put forward when Stephenson [1980a, b] and Smith and Merrill [1980] independently invoked the precession of magnetic moments (not aligned with the external AF) as the underlying mechanism. Smith and Merrill [1980] argued that for an assemblage of non-interacting SSD anisotropic grains, the precession and thermal fluctuation coupling in sufficiently large AF amplitude could account for the characteristic rotation speed-dependent RRM vector direction. Stephenson [1980a, b] on the other hand proposed that for an assemblage of randomly oriented SSD particles, it is possible to preferentially deflect the magnetic moment due to the inherent gyroscopic behavior during switching by the external field. This was thought possible by some or all of the particles having three unequal orthogonal anisotropy axes [Stephenson, 1981], a scenario later modeled by Dean et al [1990]. Stephenson [1980b] also predicted that such remanent magnetization does not require any relative motion between the specimen and the field. He then demonstrated that it is indeed possible for an anisotropic specimen to acquire what he termed gyroremanent magnetization (GRM) when subjected to static AF [Stephenson, 1980b]. Subsequently, based on geometrical considerations, isotropic samples have also been predicted and shown to be capable of acquiring GRM by two successive static AF treatments applied at different angles to a specimen [Edwards, 1982]. The most recent development on the RRM and GRM mechanism invoked metastable single domain (SD) states [Potter and Stephenson, 2006]. Such an explanation is still based on gyromagnetism, though the preferentially deflected moment is governed by available metastable net magnetic moment orientations rather than the three hypothetical unequal orthogonal anisotropy axes as proposed by Stephenson [1981]. The alternative mechanism proposed by Potter and Stephenson [2006]

helps to explain the occurrence of RRM and GRM in particles that are ellipsoids of revolution (just two unequal axes). Potter and Stephenson [2006] proposed that the range of such metastable orientations varies inversely with the particle elongation. They found a correlation between maghemite particle aspect ratio and RRM in support of this phenomenological model: the lower the ratio of width/length the smaller the RRM.

An intriguing implication that arises from the relationship between RRM (and presumably GRM) particle aspect ratio, mineralogy, and domain state is the possibility of using RRM or GRM to assist in the detection of intact chains of magnetite and/or greigite particles (magnetosomes) produced by magnetotactic bacteria (MTB), and to distinguish them from magnetosome naturally occurring in clusters [e.g. Cox et al., 2002; Simmons et al., 2007], magnetosome clusters due to lysed MTB, or non-biologically-controlled particle clusters (e.g. greigite framboids). MTB are ubiquitous in stratified aquatic environments [Lefèvre and Bazylinski, 2013]. The ferrimagnetic particles they produce, termed magnetosomes, are generally within the SSD range [Witt et al., 2005; Muxworthy and Williams, 2006; Newell, 2009; Muxworthy et al., 2013] and can contribute significantly to sedimentary magnetic signals [e.g. Heslop et al., 2013]. While some uncultivated MTB can produce complicated magnetosome arrangements [e.g. Simmons et al., 2004; Kasama et al., 2006; Abreu et al., 2013; Lefèvre and Bazylinski, 2013; Zhang et al., 2013] and the individual magnetosomes can have a wide range of aspect ratios [e.g. Lefèvre and Bazylinski, 2013; Newell, 2009 and references therein], when they take on a simple single-chain geometry, they can be modeled as a single elongated particle [e.g. Charilaou et al., 2011]. As such, on the basis of the correlation found by Potter and Stephenson [2006] between RRM and aspect ratio, one might expect that intact magnetosome chains would have lowered RRM compared to similar SSD particles not in simple chains. The purpose of the present study is to test this hypothesis. Furthermore, of the two known magnetosome mineralogies, greigite and magnetite, greigite seems to have a yet-unexplained propensity for acquiring a large RRM [Snowball, 1997; Stephenson and Snowball, 2001; Hu et al., 2002] and occasionally GRM [see Roberts et al., 2011 and references therein], at least for samples containing SSD particles in cluster form (framboids). Some measurements of RRM have been reported from putative fossilized magnetosomes (magnetofossils) in two previous studies [Snowball, 1997; Reinholdsson et al., 2013], though the co-existence of these putative greigite magnetofossils with other remanent magnetization carriers in the sediment mixture and the low rotation rate used to impart the RRM preclude an unambiguous evaluation of MTB gyromagnetism. Here we present the first RRM measurements at high rotation rate, as well as GRM experiments,

on magnetosomes from uncultivated and cultured magnetite and greigite producing MTB. The aim was to determine if there are fundamental differences between magnetite and greigite magnetosomes in their gyromagnetism and how they compare with framboidal greigite-bearing sediments.

3.3 Samples and Experimental Methods

Specimens of uncultivated MTB characterized in this study were collected from two localities in New England, USA: Upper Pond, Pettaquamscutt River Estuary, North Kingstown, Rhode Island, and the Little Sippewissett marsh, Woods Hole, Massachusetts. The Upper Pond is one of two brackish basins (surface area 0.29 km^2) with a year-round stratified water column (maximum depth 13.5 m; Orr and Gaines, 1973). Live MTB were observed from a depth, d, between d = 3.9 – 7.0 m. Whilst MTB from shallower microaerobic depths biosynthesize predominantly short single-chains of magnetite magnetosomes, MTB from d = 5.0 – 6.0 m can co-produce both magnetite and greigite. MTB found in the sulfidic hypolimnion, d=6.0 – 7.0 m produce only greigite. The samples used for measurements consist of four filters that contain particulates > 0.22 μm from 1 litre of water per discrete depth. The filters were freeze-dried and kept in vacuum between measurements. A sediment trap sample, containing dead MTB exported out of the chemocline and collected at d=7.0 m over ~10 days, and a surface sediment sample, collected by an Ekman dredge, were also included. Collectively, Upper Pond magnetosomes have a narrow and left-skewed generalized Gaussian ARM coercivity distribution on a log-field scale (median 33.9 ± 1.1 mT, dispersion factor 0.20 ± 0.03) that reflect the uniformly-sized SD particles synthesized under strict genetic control. Detailed water chemistry, MTB morphotype distribution, magnetosome properties, and sample collection and preparation are reported in Chapter 2.

The magnetotactic multicellular prokaryotes (MMPs) enriched from the sulfidic Little Sippewissett salt marsh surface sediment are 3 – 12.5 μm diameter cell aggregates of MTB cells, with each aggregate containing 491 ± 195 greigite magnetosomes [Simmons et al., 2007] and individual crystals sized 25 – 100 nm [Bazylinski et al., 1991; Pósfai et al., 1998; 2001]. Magnets were positioned a few centimeters above the sediment-water interface on the outside of the containers. The sample of MMPs used in this study consist of three filters that captured particulates sized 0.8 – 20 μm from water collected adjacent to the magnets (see Supplementary Information). ARM coercivity distribution for this sample is approximately a left-skewed generalized Gaussian (median coercivity 23.4 mT; Supplementary Information).

A sample of Little Sippewissett salt marsh sediment freeze-dried prior to MMPs enrichment described above is also included.

Two samples of cultured marine vibrio Magnetovibrio blakemorei strain MV-1 are included in this study. Cells of strain MV-1 produce 10.4 ± 3.9 magnetosomes (each with dimension 35 × 53 nm) arranged in a single chain [Bazylinski et al., 2013]. Sample MV-1_A consists of freeze-dried whole cells dispersed in calcium fluoride. Sample MV-1_B consists of lysed MV-1 cells, and therefore interacting magnetosomes, previously described [Chen et al., 2007]. Both MV-1 samples have been stored in ambient atmospheric condition and therefore partially oxidized. For comparison, two non-magnetosome samples are characterized in this study: TC05, a tuff specimen containing near SD TM ~10 titanomagnetite from the Yucca Mountain, NV, U.S.A. [Carter-Stiglitz et al., 2006], and EJC, Plio-Pleistocene greigite-containing mudstone specimens from the Lower Gutingkeng Formation in southwestern Taiwan [Horng et al., 1998; Jiang et al., 2001].

RRM and rotational ARM (rARM) were imparted by a rotational magnetizer [Stephenson and Molyneux, 1987] housed at the University of Alberta. The procedure consists of three steps (Figure 1). Firstly, the sample was set to rotate clockwise (direction of rotation vector, ω, denoted –z in sample coordinate marked arbitrarily on paleomagnetic plastic cubes) at ~95 r.p.s, then an AF (max: 80 mT, frequency: 60 Hz) was applied perpendicularly to the rotational vector, held for ~5 s, and ramped down linearly to zero (at ~7 mT s^{-1}). All the while, a small vertical field was applied by a direct-field (DF) coil to cancel the Earth's local field and the field produced by the motor driving the rotation. The motor was then turned off, and the sample measured by a calibrated spinner magnetometer. By convention, a "normal" RRM is acquired by the sample antiparallel to the rotation vector, i.e. a +z remanent magnetization acquired during a clockwise rotation is denoted normal. Secondly, the above process was repeated with the sample installed in the rotational magnetizer in exactly the same orientation but instead rotating in an anti-clockwise manner (i.e. the rotation vector was now in the +z direction and a normal RRM is acquired in the –z direction). An average RRM is obtained by subtracting the RRM in step 2 from the RRM in step 1 and dividing by two. This has the advantage that the external fields do not need to be perfectly cancelled. Thirdly, the sample was again returned to the rotational magnetizer in the same orientation as the previous steps and set to rotate anti-clockwise, but no field was applied by the direct-field coil. As a result, the acquired remanence is the sum of a rARM acquired in the vertical field provided by the Earth's field plus the motor field (~70 μT) in the

+z direction in addition to an RRM in the -z direction from step 2. The RRM and rARM were calculated as:

$$RRM = 0.5(M_{z1} - M_{z2}) \quad (1)$$

$$rARM = (M_{z3} - M_{z2}) \quad (2)$$

, where M_{z1}, M_{z2}, M_{z3} are the remanent magnetization in the sample's z–coordinate measured after the first, second, and third step described above, respectively. Additionally, we calculate the effective gyrofield, rB_g, considered as the equivalent direct field acting along the rotation vector generated during particle switching, which is gyroscopic in origin and produces an inherently asymmetrical distribution of moments due to the rotation, by the external AF that resulted in deflection of the particle moment [A. Stephenson, 1980a; Potter and Stephenson, 1986]:

$$rB_g = b(RRM/rARM) \quad (3)$$

, where b = 70 μT is the direct field used to impart rARM.

For the static GRM experiment, we employed the protocol outlined in Edwards [1982]. A paleomagnetic plastic cube containing the sample was marked with arbitrary orthogonal axes, and a maximum AF of 80 mT (0.0075 mT half-cycle^{-1}) was applied by a D-tech AF demagnetizer throughout the experiment. The experiment consists of three applications of an AF and two magnetization measurements for a given angle Θ (between x and AF axes) carried out in a magnetically shielded room in the Institute for Rock Magnetism at the University of Minnesota. In the first step, the sample was inserted into the D-tech AF demagnetizer and the AF applied along the +x axis. In the second step, the sample was rotated through an angle Θ in the xy plane (z being parallel to the rotation vector) and the AF was applied again. The resulting remanent magnetization, M_1, was measured by a 2G DC SQUID magnetometer. In the third step, the AF was again applied along the x axis. The resulting remanent magnetization, M_2, was measured. The GRM was calculated as follows:

$$GRM(\Theta) = 0.5(M_{z1} - M_{z2}) \quad (4)$$

, where M_{z1} and M_{z2} are the remanent magnetizations in the z-coordinate of M_1, and M_2, respectively. Unlike in the RRM experiment detailed above, the specimen in the static GRM experiment is only rotated through one direction, i.e. anti-clockwise. As such, and following the same convention as for RRM, a positive or "normal" GRM is acquired antiparallel to the rotation vector (i.e. in –z). Lastly, we acquire a static ARM (sARM) along +x after

GRM(180°) using AF_{max} = 80mT (0.0075 mT half-cycle^{-1}) and a 70 μT direct field, and calculate a static effective gyrofield:

$$sB_g = b(GRM/sARM) \quad (5)$$

, where b = 70 μT and sARM is taken as the remanent magnetization measured along +x.

3.4 Results and Interpretations

Table 1 summarizes the results for the RRM and rARM experiments. Intact chain magnetosome samples (uncultivated MTB from Pettaquamscutt River estuary Upper Pond water column, enriched MMP from the Little Sippewissett salt marsh, MV-1_A) acquired negligible to very low RRM compared to the respective rARM, resulting in low rB_g. Whilst RRM data from samples containing assemblages of non-interacting and non-chain SD particles having the same size as the magnetosomes are not available, we note that all of the rB_g measured from intact chain magnetosomes in this study are significantly smaller than the rB_g of 102 μT and 305 μT measured from dispersed, naturally irregularly shaped magnetite < 0.7 μm and synthetic cubic shaped magnetite 0.2-0.8 μm, respectively, in Potter and Stephenson [1986] (acquired at 108 r.p.s., AF_{max} = 80 mT, AF frequency = 50 Hz, b = 43 μT). We interpret the small rB_g from the MTB samples as a consequence of a predominant magnetosome chain and chain-like architecture, which may be approximated as a very elongated particle. Potter and Stephenson [2006] have shown for assemblages of randomly oriented and dilute dispersion of SD maghemite particles that RRM correlates inversely with particle elongation. According to their phenomenological model, elongated particles have fewer stable moment orientations that are conducive to retaining deflected moment during switching by the external AF.

The highest rB_g we measured among intact magnetosome specimens is 7.3 μT from the enriched MMP of the Little Sippewissett salt marsh which contains greigite magnetosomes. The slightly higher rB_g measured from this sample may reflect a higher propensity of RRM acquisition by greigite relative to magnetite. However, as the magnetosomes in the MMP often form chain bundles rather than isolated single chains [e.g. Abreu et al., 2013], the influence of magnetostatic interaction cannot be excluded. In fact, data from this study suggest magnetostatic interaction seems to enhance rB_g. This is evident from the result of MV-1_B, which contains interacting partially-oxidized magnetite magnetosomes with rB_g = 10.9 μT compared to rB_g = 1.0 μT from the freeze-dried whole cell with partially-oxidized magnetite magnetosomes (MV-1_A). Similarly, the surface sediment

from both the Pettaquamscutt River estuary Upper Pond and the Little Sippewissett salt marsh have larger rB_g than the MTB prior to sedimentation at the respective localities. One possible explanation is that the surface sediments contain proportionally more lysed MTB cells and their magnetosomes (once in a single chain or chain bundle geometry) that subsequently clumped during sedimentation. rB_g enhancement by magnetostatic interaction may also explain the much larger rB_g of 77 to 1070 μT (acquired at 95 r.p.s., AF_{max} = 80 mT, AF frequency = 50 Hz, b = 70 μT [Stephenson and Snowball, 2001; Hu et al., 2002]) commonly associated with sedimentary specimens containing greigite clusters that are often highly interacting [see Roberts et al. 2011 and references therein], including the two greigite-containing mudstone specimens measured in the present study (rB_g = 552.2 μT and 790.4 μT, Table 1).

Table 1, Figures 2 and 3 show results from the static GRM experiment. Edwards [1982] posited that for an isotropic specimen GRM as a function of Θ is described by $A[(\pi/2)\Theta - \Theta^2]$, for $0 \leq \Theta \leq \pi/2$, and $A[(\pi^2/2)\Theta - (3\pi/2) + \Theta^2]$, for $\pi/2 \leq \Theta \leq \pi$ where A is a material dependent constant. According to this prediction, the GRM(Θ) is a maximum (minimum) at Θ = 45° (135°) and zero at Θ = 0°, 90° and 180°. Uncultivated MTB from the Pettaquamscutt River estuary water column, the enriched MMP, and MV-1_A acquired negligible GRM comparable to the background instrument signal at all angles (Figures 2a, b, d, e). The other two magnetosome containing specimens, surface sediment from the Pettaquamscutt River estuary Upper Pond and MV-1_B, acquired more pronounced GRM (Figures 2c, f). However, the sign of the GRM acquired is reversed from those predicted by Edwards [1982] for MV-1_B, i.e. the GRM was acquired parallel instead of antiparallel to the rotation vector. This sample also acquired a reversed RRM (Table 1). It is not clear why MV-1_B displays the reversed RRM and GRM behavior. Perhaps magnetostatic interaction among the clumped magnetosomes is responsible, though clearly the effect of interaction on RRM and GRM is complicated as reversed RRM measured at high rotation rate are not commonly associated with highly interacting greigite-bearing mudstone (this study) and sediments [Stephenson and Snowball, 2001; Hu et al., 2002]. We note that both sB_g and rB_g are positively correlated (Figures 3) as expected since both types of remanent magnetization are due to gyromagnetism.

Six paleomagnetic plastic cube samples were prepared from homogenized powder of TC05 and EJC40.3B. Cubes 1 to 5 were used in the static GRM experiment while Cube 6 was used for the acquisition of sARM. In the first instance, each cube 1 to 5 was subjected to

static AF (max = 80 mT) demagnetization along the +x. Then each cube 1 to 5 were rotated through an angle Θ = 0°, 45°, 90°, 135°, 180°, respectively, AF demagnetized again before being returned to their initial position and demagnetized for the third time (Figure 4c). The results are shown in blue in Figures 4a, b. Cube 1 from each sample that was used for Θ = 0° experiment above were further repeated for the three successive AF demagnetization step for Θ = 45°, 90°, 135°, and 180° to investigate the effect of treatment history and the results are shown in red in Figures 4a, b. While TC05 results are independent of prior demagnetization treatment, EJC40.3B results seem to depend on the AF treatment history. The two most likely explanations for the observed behavior are mineralogy of the GRM carrier (TM10 for TC05, greigite for EJC40.3B) and magnetostatic interaction (nearly no interaction for TC05 and likely marked interaction for EJC40.3B).

3.5 Discussion

It appears that RRM and GRM acquisition are strongly influenced by particle arrangement and magnetostatic interaction. Even though the magnetosomes are within the SD size limit and should be excellent carriers of gyroremanence, their associated rB_g (in μT) is far smaller than that predicted from the empirical $rB_g \cong 100/s$ relationship (s being the particle size in μm) for submicron magnetite particles [Potter and Stephenson, 1986]. Instead, the chain architecture and the associated small magnetosome width/magnetosome chain length ratio, even for the uncultivated MTB that forms complicated non-single-linear chains (e.g. uncultivated MTB from Pettaquamscutt River estuary and MMP), seem to limit the acquisition of RRM and GRM as predicted by Potter and Stephenson [2006].

The data presented in this study suggest that greigite magnetosomes (e.g. MMP) are only marginally better carriers of RRM and GRM than their stoichiometric and partially-oxidized magnetite counterpart (e.g. uncultivated MTB from the Pettaquamscutt River estuary water column, MV-1_A), at least when the comparison is made between intact whole MTB cells. We surmise that greigite mineralogy is not what gives rise to the large rB_g and pronounced GRM often associated with greigite-bearing sediment. Rather, the large inter-particle interaction between SD greigite particles in cluster form (perhaps acting like a large SD particle) may be responsible for their propensity for acquiring a large RRM and GRM. Some evidence for enhanced RRM and GRM acquisition is presented in this study between whole cell vs lysed magnetosomes. Alternatively, greigite magnetosomes differ from authigenic greigite in framboidal form in their structural defects. Stacking faults, with yet unknown effect on gyromagnetism, are commonly associated with greigite magnetosomes

[Pósfai et al., 2001] and may have resulted from the transformation of mackinawite or cubic FeS to greigite [Pósfai et al., 1998a, b].

Previously, small rB_g values measured at a low rotation rate of ~5 r.p.s. for putative magnetosome-bearing sediment were found by Snowball [1997] and Reinholdsson et al. [2013]. Our results, for high rotation frequency of 95 r.p.s., suggest that the low rB_g from magnetosome-bearing sediments, compared to the high values of 84 – 137 μT in greigite-bearing sediments reported by Snowball [1997], is not entirely due to dilution by the large MD detrital magnetic particles in the sedimentary mixture. Similarly, we surmise that the absence of a pronounced GRM associated with a bacterial greigite bearing soil in a study by Fassbinder and Stanjek [1994] is due to the inherently low GRM and RRM acquisition by such particles.

3.6 Conclusion

Rotational and static gyromagnetism experiments were performed on samples containing uncultivated and cultivated MTB. We found that magnetosomes, despite being within the SD size range, uniformly acquire negligible rotational– and gyro–remanent magnetization regardless of magnetosome composition. One plausible explanation for this observation is that the chain or chain-like magnetosome arrangement effectively limits the number of stable moment orientations that are conducive to retaining deflected moment during switching by the externally applied magnetic field. The effect of dipolar interaction on gyromagnetism is gleaned from the marginally higher effective gyrofield obtained for lysed cultured MTB cells and sediment that potentially contain lysed uncultivated MTB cells (as opposed to intact whole MTB cells). This may explain the large gyrofield typically associated with highly interacting SD greigite particles arranged in framboidal form. Lastly, the markedly low gyroremanence acquired by greigite magnetosomes compared to authigenic greigite framboid–bearing sediments may imply that structural defects limit gyroremanence acquisition.

Acknowledgement

This work was supported by the Higher Degree Research fund from Department of Environment and Geography, Macquarie University and a visiting fellowship to the Institute for Rock Magnetism (IRM) to A.P.C. A.P.C. thanks M. Jackson for the inspiration of this study and for helpful discussion.

References

Abreu, F., K. T. Silva, P. Leão, I. A. Guedes, C. N. Keim, M. Farina, and U. Lins (2013), Cell Adhesion, Multicellular Morphology, and Magnetosome Distribution in the Multicellular Magnetotactic Prokaryote Candidatus Magnetoglobus multicellularis, *Microsc. Microanal.*, *19*(03), 535–543, doi:10.1017/S1431927613000329.

Bazylinski, D. A., R. B. Frankel, A. J. Garratt-Reed, and S. Mann (1991), Biomineralization of Iron Sulfides in Magnetotactic Bacteria from Sulfidic Environments, in *Iron Biominerals*, edited by R. B. Frankel and R. P. Blakemore, pp. 239–255, Springer US, Boston, MA.

Bazylinski, D. A. et al. (2013), Magnetovibrio blakemorei gen. nov., sp. nov., a magnetotactic bacterium (Alphaproteobacteria: Rhodospirillaceae) isolated from a salt marsh, *Int. J. Syst. Evol. Micr.*, *63*(Pt 5), 1824–1833, doi:10.1099/ijs.0.044453-0.

Brock, A., and W. Iles (1974), Some Observations of Rotational Remanent Magnetization, *Geophys. J. Int.*, *38*(2), 431–433, doi:10.1111/j.1365-246X.1974.tb04134.x.

Carter-Stiglitz, B., P. Solheid, R. Egli, and A. Chen (2006), Tiva Canyon Tuff (II): near single domain standard reference material available, *IRM Quarterly*, *16*(1).

Charilaou, M., M. Winklhofer, and A. U. Gehring (2011), Simulation of ferromagnetic resonance spectra of linear chains of magnetite nanocrystals, *J. Appl. Phys.*, *109*(9), 093903, doi:10.1063/1.3581103.

Chen, A. P., R. Egli, and B. M. Moskowitz (2007), First-order reversal curve (FORC) diagrams of natural and cultured biogenic magnetic particles, *J.Geophys. Res.*, *112*(B8), doi:10.1029/2006JB004575.

Cox, B. L., R. Popa, D. A. Bazylinski, B. Lanoil, S. Douglas, A. Belz, D. L. Engler, and K. H. Nealson (2002), Organization and Elemental Analysis of P-, S-, and Fe-rich Inclusions in a Population of Freshwater Magnetococci, *Geomicrobl. J.*, *19*(4), 387–406, doi:10.1080/01490450290098504.

Dean, B., R. W. Chantrell, A. Hart, D. . Parker, and A. Stephenson (1990), The mathematical modeling of the acquisition of gyroremanent magnetization in a single domain particle, *J. Appl. Phys.*, *67*(9), 4481–4483.

Edwards, J. (1980), An experiment relating to rotational remanent magnetization and frequency of demagnetizing field, *Geophys. J. Int.*, *60*(2), 283–288, doi:10.1111/j.1365-246X.1980.tb04293.x.

Edwards, J. (1982a), Studies of partial rotational remanent magnetization and rotational remanent magnetization at slow speeds of rotation, *Geophys. J. Int.*, *68*(3), 609–624, doi:10.1111/j.1365-246X.1982.tb04918.x.

Edwards, J. (1982b), Gyroremanent magnetization produced by specimen rotation between successive alternating field treatments, *Geophys. J. Int.*, *71*(1), 199–214, doi:10.1111/j.1365-246X.1982.tb04993.x.

Edwards, J., and M. Desta (1989), Static alternating field demagnetizations of anhysteretic and rotational remanent magnetizations in rocks and synthesized samples, *Geophys. J. Int.*, *99*(3), 739–748, doi:10.1111/j.1365-246X.1989.tb02055.x.

Fassbinder, J. W. E., and H. Stanjek (1994), Magnetic properties of biogenic soil greigite (Fe_3S_4), *Geophys. Res. Lett.*, *21*(22), 2349–2352, doi:10.1029/94GL02506.

Frankel, R. B., D. A. Bazylinski, M. S. Johnson, and B. L. Taylor (1997), Magneto-aerotaxis in marine, coccoid bacteria, *Biophys. J.*, *73*, 994–1000.

Heslop, D., A. P. Roberts, L. Chang, M. Davies, A. Abrajevitch, and P. De Deckker (2013), Quantifying magnetite magnetofossil contributions to sedimentary magnetizations, *Earth Planet. Sci. Lett.*, *382*, doi:10.1016/j.epsl.2013.09.011.

Hillhouse, J. W. (1977), A method for the removal of rotational remanent magnetization acquired during alternating field demagnetization, *Geophys. J. Int.*, *50*(1), 29–34, doi:10.1111/j.1365-246X.1977.tb01322.x.

Horng, C.-S., M. Torii, K.-S. Shea, and S.-J. Kao (1998), Inconsistent magnetic polarities between greigite- and pyrrhotite/magnetite-bearing marine sediments from the Tsailiao-chi section, southwestern Taiwan, *Earth Planet. Sci. Lett.*, *164*(3-4), 467–481, doi:10.1016/S0012-821X(98)00239-8.

Hu, S., A. Stephenson, and E. Appel (2002), A study of gyroremanent magnetisation (GRM) and rotational remanent magnetisation (RRM) carried by greigite from lake sediments, *Geophys. J. Int.*, *151*(2), 469–474, doi:10.1046/j.1365-246X.2002.01793.x.

Jiang, W.-T., C.-S. Horng, A. P. Roberts, and D. R. Peacor (2001), Contradictory magnetic polarities in sediments and variable timing of neoformation of authigenic greigite, *Earth Planet. Sci. Lett.*, *193*(1-2), 1–12, doi:10.1016/S0012-821X(01)00497-6.

Kasama, T. (2006), Magnetic properties, microstructure, composition, and morphology of greigite nanocrystals in magnetotactic bacteria from electron holography and tomography, *Am. Mineral.*, *91*(8-9), 1216–1229, doi:10.2138/am.2006.2227.

Lefèvre, C. T., and D. A. Bazylinski (2013), Ecology, Diversity, and Evolution of Magnetotactic Bacteria, *Microbiol. Mol. Biol. Rev.*, *77*(3), 497–526, doi:10.1128/MMBR.00021-13.

Madsen, A. T. (2009), A chronology of hurricane landfalls at Little Sippewissett Marsh, Massachusetts, USA, using optical dating, *Geomorphology*, 109, 36 – 45, doi:10.1016/j.geomorph.2008.08.023.

Madsen, K. N. (2003), A reversed gyromagnetic effect in chromium dioxide particles, *J. Magn. Magn. Mater.*, *260*(1-2), 131–140, doi:10.1016/S0304-8853(02)01238-6.

Madsen, N.K. (2004), Angular dependence of the switching field and implications for gyromagnetic remanent magnetization in three-axis alternating-field demagnetization, *Geophys. J. Int.*, *157*(3), 1007–1016, doi:10.1111/j.1365-246X.2004.02228.x.

Mahon, S. W., and A. Stephenson (1997), Rotational remanent magnetization (RRM) and its high temporal and thermal stability, *Geophys. J. Int.*, *130*(2), 383–389, doi:10.1111/j.1365-246X.1997.tb05654.x.

Moench, T. T., and W. A. Konetzka (1978), A novel method for the isolation and study of a magnetotactic bacterium, *Arch. Microbiol.*, *119*(2), 203–212, doi:10.1007/BF00964274.

Muxworthy, A. R., and W. Williams (2006), Critical single-domain/multidomain grain sizes in noninteracting and interacting elongated magnetite particles: Implications for magnetosomes, *J. Geophys. Res.*, *111*(B12), doi:10.1029/2006JB004588.

Muxworthy, A. R., W. Williams, A. P. Roberts, M. Winklhofer, L. Chang, and M. Pósfai (2013), Critical single domain grain sizes in chains of interacting greigite particles: Implications for magnetosome crystals: Single Domain Grain Sizes in Greigite, *Geochem. Geophys. Geosys.*, *14*(12), 5430–5441, doi:10.1002/2013GC004973.

Newell, A. J. (2009), Transition to superparamagnetism in chains of magnetosome crystals, *Geochem. Geophys. Geosys.*, *10*(11), n/a–n/a, doi:10.1029/2009GC002538.

Noel, M. (1988), Some observations of the gyroremanent magnetization acquired by rocks in a rotating magnetic field, *Geophys. J. Int.*, *92*(1), 107–110, doi:10.1111/j.1365-246X.1988.tb01125.x.

Orr, W. L., and A. G. J. Gaines (1973), Observations on the rate of sulfate reduction and organic matter oxidation in the bottom waters of an estuarine basin: The upper basin of the Pettaquamscutt River (Rhode Island)., in *Advances in Organic Geochemistry* (eds. B. Tissot and F. Bienner), pp. 791–812.

Pósfai, M., P. R. Buseck, D. A. Bazylinski, and R. B. Frankel (1998), Reaction Sequence of Iron Sulfide Minerals in Bacteria and Their Use as Biomarkers, *Science*, *280*(5365), 880–883, doi:10.1126/science.280.5365.880.

Pósfai, M., P. R. Buseck, D. A. Bazylinski, and R. B. Frankel (1998), Iron sulfides from magnetotactic bacteria: Structure, composition, and phase transitions, *Am. Mineral.*, *83*, 1469–1481.

Pósfai, M., K. Cziner, E. Márton, P. Márton, P. R. Buseck, R. R. B. Frankel, and D. A. Bazylinski (2001), Crystal-size distributions and possible biogenic origin of Fe sulfides, *Eur. J. Mineral.*, *13*(4), 691–703, doi:10.1127/0935-1221/2001/0013-0691.

Potter, D. K., and A. Stephenson (1986), The detection of fine particles of magnetite using anhysteretic and rotational remanent magnetizations, *Geophys. J. Int.*, *87*(2), 569–582, doi:10.1111/j.1365-246X.1986.tb06638.x.

Potter, D. K., and A. Stephenson (2006), The stable orientations of the net magnetic moment within single-domain particles: Experimental evidence for a range of stable states and implications for rock magnetism and palaeomagnetism, *Phys. Earth Planet. In.*, *154*(3-4), 337–349, doi:10.1016/j.pepi.2005.06.018.

Reinholdsson, M., I. Snowball, L. Zillén, C. Lenz, and D. J. Conley (2013), Magnetic enhancement of Baltic Sea sapropels by greigite magnetofossils, *Earth Planet. Sci. Lett.*, *366*, 137–150, doi:10.1016/j.epsl.2013.01.029.

Roberts, A. P., L. Chang, C. J. Rowan, C.-S. Horng, and F. Florindo (2011), Magnetic properties of sedimentary greigite (Fe_3S_4): An update, *Rev. Geophys.*, *49*(1), doi:10.1029/2010RG000336.

Roperch, P., and G. K. Taylor (1986), The importance of gyromagnetic remanence in alternating field demagnetization. Some new data and experiments on G.R.M. and R.R.M., *Geophys. J. Int.*, *87*(3), 949–965, doi:10.1111/j.1365-246X.1986.tb01978.x.

Sagnotti, L., and A. Winkler (1999), Rock magnetism and palaeomagnetism of greigite-bearing mudstones in the Italian peninsula, *Earth Planet. Sci. Lett.*, *165*(1), 67–80, doi:10.1016/S0012-821X(98)00248-9.

Shi, H., and D. H. Tarling (1999), The origin of bore-core remanences: mechanical-shock-imposed irreversible magnetizations, *Geophys. J. Int.*, *137*(3), 831–838, doi:10.1046/j.1365-246x.1999.00850.x.

Simmons, S. L., D. A. Bazylinski, and K. J. Edwards (2007), Population dynamics of marine magnetotactic bacteria in a meromictic salt pond described with qPCR, *Environ. Microbiol.*, *9*(9), 2162–2174, doi:10.1111/j.1462-2920.2007.01330.x.

Smith, G., and R. T. Merrill (1980), The origin of rotational remanent magnetization, *Geophys. J. Int.*, *61*(2), 329–336, doi:10.1111/j.1365-246X.1980.tb04320.x.

Snowball, I. F. (1997), The detection of single-domain greigite (Fe_3S_4) using rotational remanent magnetization (RRM) and the effective gyro field (Bg): mineral magnetic and palaeomagnetic applications, *Geophys. J. Int.*, *130*(3), 704–716, doi:10.1111/j.1365-246X.1997.tb01865.x.

Stephenson, A. (1980a), Rotational remanent magnetization and the torque exerted on a rotating rock in an alternating magnetic field, *Geophys. J. Int.*, *62*(1), 113–132, doi:10.1111/j.1365-246X.1980.tb04847.x.

Stephenson, A. (1980b), A gyroremanent magnetisation in anisotropic magnetic material, *Nature*, *284*(5751), 49–51, doi:10.1038/284049a0.

Stephenson, A., and D. K. Potter (1987), Gyroremanent Magnetizations in Dilute Anisotm Dispersions of Gamma Ferric Oxide Particles fro Magnetic Recording Tape, *IEEE Trans Magn*, *MAG-23*(5), 3820–3830.

Stephenson, A. (1988), Gyromagnetic remanence produced by rotation of magnetite and maghemite particles in a slowly reducing direct field, *J. Magn. Magn. Mater.*, *71*(2), 179–185, doi:10.1016/0304-8853(88)90083-2.

Stephenson, A., and L. Molyneux (1991), A versatile instrument for the production, removal and measurement of magnetic remanence at different temperatures, *Meas. Sci. Techn.*, *2*(4), 280–286, doi:10.1088/0957-0233/2/4/003.

Stephenson, A. (1981), Gyromagnetic remanence in single-domain particles, rocks, and magnetic recording tape, *Phil. Mag. B.*, 44, 635 – 664.

Stephenson, A., and I. F. Snowball (2001), A large gyromagnetic effect in greigite, *Geophys. J. Int.*, *145*(2), 570–575, doi:10.1046/j.0956-540x.2001.01434.x.

Suzuki, Y., R. Kopp, T. Kogure, A. Suga, K. Takai, S. Tsuchida, N. Ozaki, K. Endo, J. Hashimoto, and Y. Kato (2006), Sclerite formation in the hydrothermal-vent "scaly-foot" gastropod—possible control of iron sulfide biomineralization by the animal, *Earth Planet. Sci. Lett.*, *242*(1-2), 39–50, doi:10.1016/j.epsl.2005.11.029.

Thomson, G. F. (1990), The anomalous demagnetization of pyrrhotite, *Geophys. J. Int.*, *103*(2), 425–430, doi:10.1111/j.1365-246X.1990.tb01781.x.

Wilson, R. L., and R. Lomax (1972), Magnetic Remanence Related to Slow Rotation of Ferromagnetic Material in Alternating Magnetic Fields, *Geophys. J. Int.*, *30*(3), 295–303, doi:10.1111/j.1365-246X.1972.tb05815.x.

Witt, A., K. Fabian, and U. Bleil (2005), Three-dimensional micromagnetic calculations for naturally shaped magnetite: Octahedra and magnetosomes, *Earth Planet. Sci. Lett.*, *233*(3-4), 311–324, doi:10.1016/j.epsl.2005.01.043.

Zhang, W.-Y., K. Zhou, H.-M. Pan, H.-J. Du, Y.-R. Chen, R. Zhang, W. Ye, C. Lu, T. Xiao, and L.-F. Wu (2013), Novel Rod-Shaped Magnetotactic Bacteria Belonging to the Class Alphaproteobacteria, *Appl. Environ. Microb.*, *79*(9), 3137–3140, doi:10.1128/AEM.03869-12.

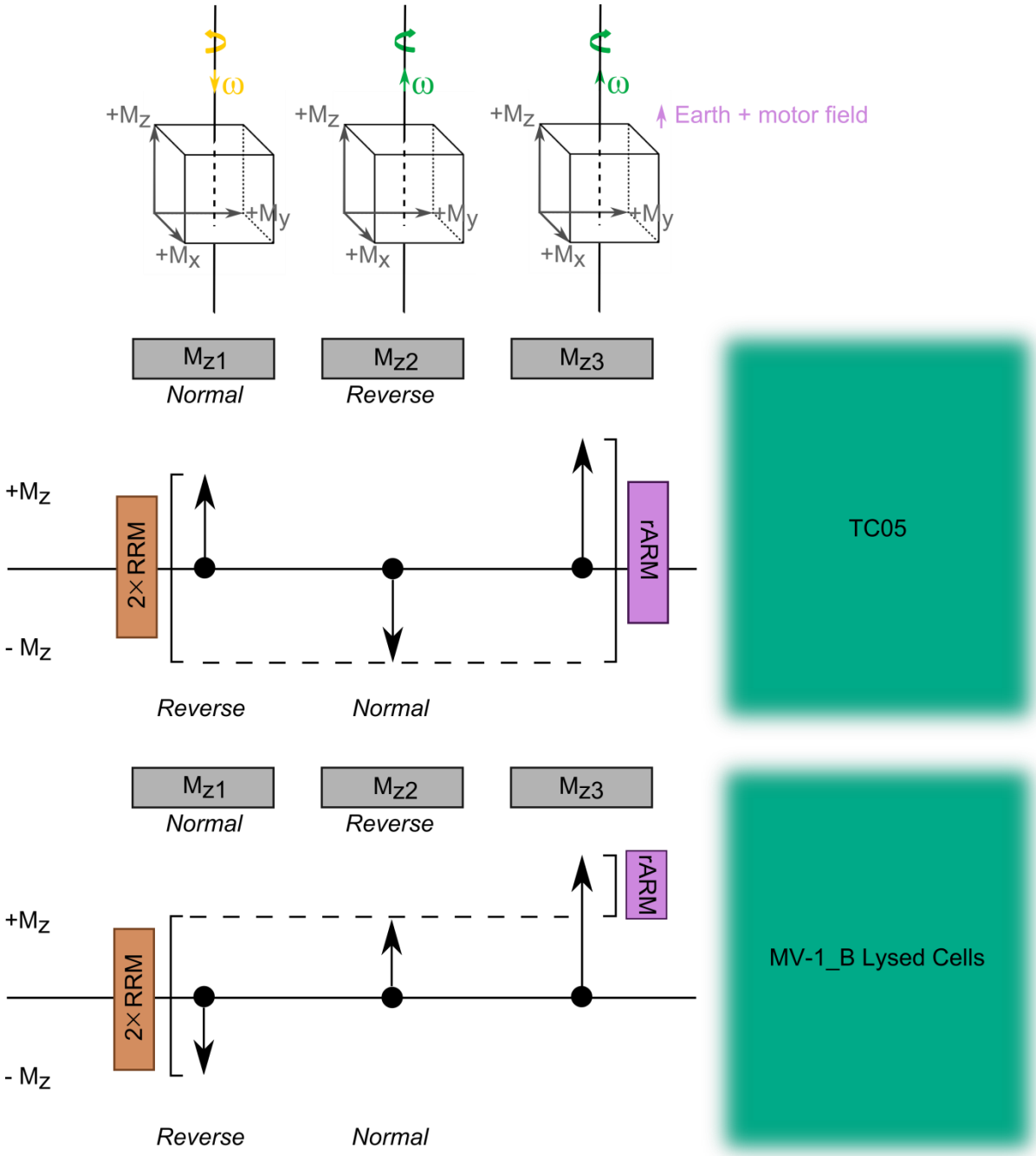

Figure 3-1: RRM acquisition schematics. The lengths of the arrowed vectors are not to scale. ω is the rotation vector, M_x, M_y, M_z are arbitrary sample remanent magnetization coordinate, the sum of the ambient Earth's magnetic field and the motor (inside the RRM instrument) field amounts to approximately 70 µT, M_{z1}, M_{z2}, M_{z3}, are the remanent magnetization in the sample z-axis after the first, second, and third experimental steps (see text).

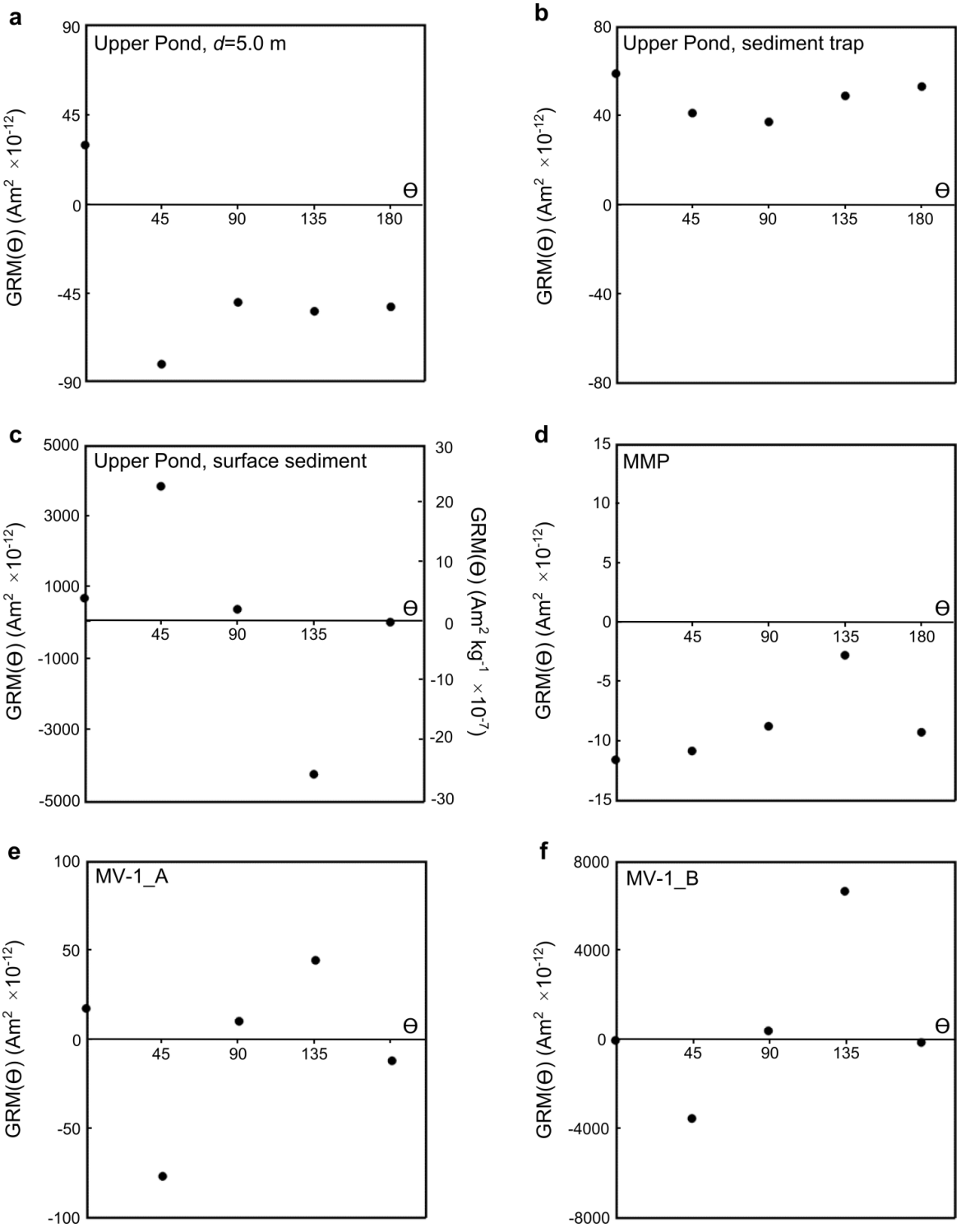

Figure 3-2: Static GRM acquired as a function of angle Θ. (**a**) Upper Pond MTB, (**b**) MTB in sediment trap installed over a period of ~10 days in the Upper Pond, (**c**) Upper Pond surface sediment for which MTB carry ~77% of the overall ARM signal, (**d**) enriched MMP from the Little Sippeewissett salt marsh, (**e**) cultured MV-1 whole cells, (**f**) cultured MV-1 lysed cells.

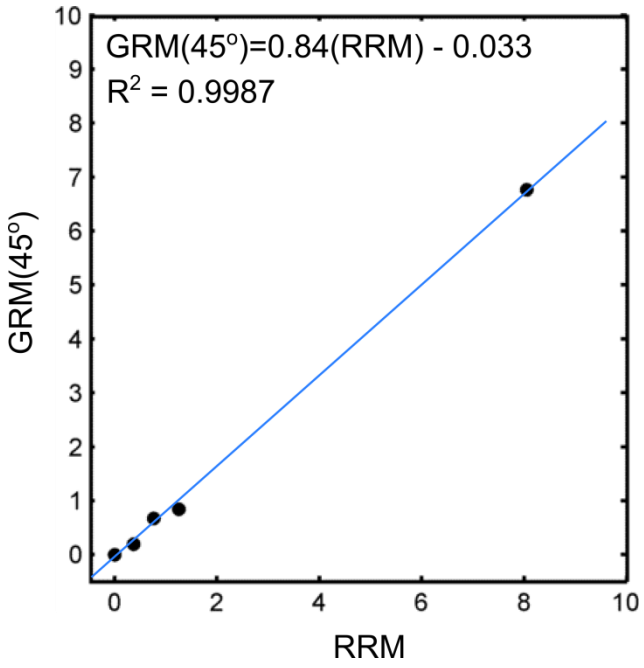

Figure 3-3: Static GRM vs. RRM. For nine samples shown in Table 1. RRM and GRM(45°) shown have the same normalizer (litre of water filtered, days of sediment trap deployed, sample mass, or no normalizer) for a given sample. Five out of nine specimens plotted here have nearly identical RRM and GRM around ~0.

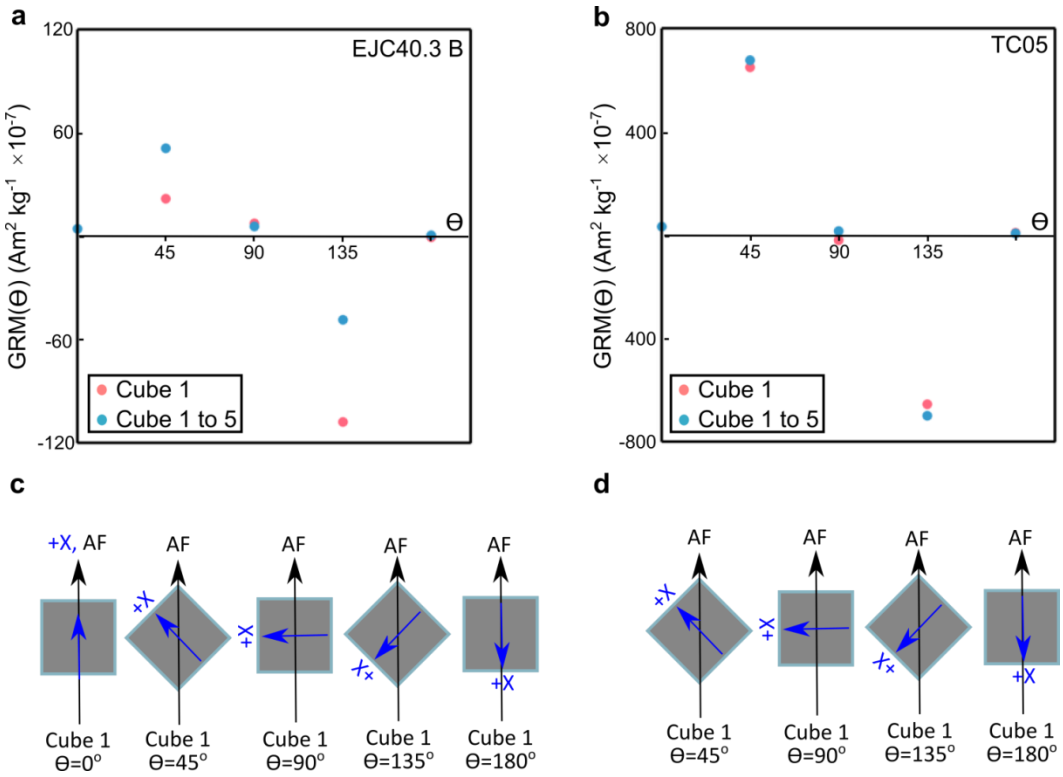

Figure 3-4: Static GRM acquired as a function of angle Θ for non-MTB samples. (**a**) greigite-bearing mudstone and (**b**) Tiva Canyon tuff. (**c-d**) The position of the $+x$ (specimen coordinate, in blue) with respect to the AF direction (black) for the two types of static GRM experiments performed.

Table 3-1| Rotational-, anhysteretic-, gyro-remanent magnetization							
	Magnetic Mineral	**[1] RRM**	**[2] χ_{rARM}**	**rB_g**	**GRM(45°)**	**[3] χ_{sARM}**	**sB_g**
Upper Pond, Pettaquamscutt River Estuary, RI, U.S.A.							
Water Column Particulate (d=5.0 m)	SD magnetite magnetosome from uncultivated MTB	($Am^2 L^{-1}$) 0	($m^3 L^{-1}$) 20.7×10^{-11}	(μT) 0	($Am^2 L^{-1}$) -5.65×10^{-11}	($m^3 L^{-1}$) 3.89×10^{-10}	(μT) -0.2
Sediment trap	SD magnetite & greigite from uncultivated MTB	($Am^2 Day^{-1}$) -146×10^{-12}	($m^3 Day^{-1}$) 7.62×10^{-11}	2.4	($Am^2 Day^{-1}$) 6.70×10^{-12}	($m^3 Day^{-1}$) 16.3×10^{-11}	0.1
Surface sediment	~77% magnetite & greigite magnetosomes	($Am^2 kg^{-1}$) 36.9×10^{-6}	($m^3 kg^{-1}$) 8.34×10^{-6}	5.6	($Am^2 kg^{-1}$) 1.97×10^{-6}	($m^3 kg^{-1}$) 16.3×10^{-6}	0.2
Little Sippewissett salt marsh, Woods Hole, MA, U.S.A.							
Enriched MMP	SD greigite magnetosomes from MMP	(Am^2) 320×10^{-11}	($A\ m^{-1}$) 5.51×10^{-10}	7.3	(Am^2) -1.08×10^{-11}	($A\ m^{-1}$) 6.96×10^{-10}	0
Surface sediment		($Am^2 kg^{-1}$) 6.01×10^{-7}	($m^3 kg^{-1}$) 3.35×10^{-8}	22.5	----------Not measured----------		
MTB Culture strain MV-1							
	SD (partially-oxidized) magnetite magnetosome	(Am^2)	($A\ m^{-1}$)		(Am^2)	($A\ m^{-1}$)	
MV-1_A freeze dried whole cells		-448×10^{-11}	5.72×10^{-9}	1.0	-7.68×10^{-11}	11.3×10^{-9}	0
MV-1_B lysed cells		[4] -105×10^{-9}	[4] 1.20×10^{-8}	[4] 10.9	-3.54×10^{-9}	1.26×10^{-8}	-0.4
Tiva Canyon tuff, NV, U.S.A.							
	near SD ~TM10 titanomagnetite	($Am^2 kg^{-1}$)	($m^3 kg^{-1}$)		($Am^2 kg^{-1}$)	($m^3 kg^{-1}$)	
TC05 mixture of level 7.1, 7.2, 9.0		80.4×10^{-5}	3.15×10^{-5}	32.0	6.76×10^{-5}	12.5×10^{-5}	0.7
Lower Gutingkeng Formation (Taiwan) mudstone							
		($Am^2 kg^{-1}$)	($m^3 kg^{-1}$)		($Am^2 kg^{-1}$)	($m^3 kg^{-1}$)	
EJC40.3B	SD framboidal greigite	----------Not measured----------			5.10×10^{-6}	2.20×10^{-7}	29.1
EJC49.1C		76.0×10^{-6}	17.3×10^{-8}	552.2	6.73×10^{-6}	1.06×10^{-8}	799.7
EJC50.1C		125×10^{-6}	199×10^{-9}	790.4	8.43×10^{-6}	1.60×10^{-9}	6605.5
[1] Positve *RRM*="Normal" *RRM* = RRM acquired antiparallel to the rotation vector (see Figure 1)							
[2] Susceptibility of rARM along M_z acquired at ~95 r.p.s., AF max = 80 mT, b = 70 μT							
[3] Susceptibility of sARM along M_x acquired at AF max = 80 mT, DC = 70 μT							
[4] Averaged from 2 measurement replicates							

Supplementary Information

Magnetotactic multicellular prokaryotes (MMPs) enriched from the Little Sippewissett salt marsh (Figure S3-1).

For the collection of MMPs, thirty-two 2-quart (~1.9 L) containers and ten 1-L containers were filled approximately half-full of surface sediments from a shallow mud pond in the Little Sippewissett salt marsh. A small amount of sediment was freeze-dried immediately upon collection and kept in vacuum until, and in between, magnetic measurements. The sediment has a strong "rotten egg" smell from its high hydrogen sulfide content. It is also very rich in organic matter and contains abundant and visible purple aggregates of bacteria (Figure S3-2a). The other half of each container was filled with water collected from the same mud pond. Following the method of *Moench and Konetzka* [1978] for MTB enrichment, bar magnets were attached approximately 2 cm above the sediment water interface on two opposing sides of the container as illustrated in Figure S1b after the sediment has been settling for ~1 hr. The containers were covered up by aluminum foil and allowed to settle for an additional 3 to 5 hours. A pipette was then used to collect approximately 2-mL of water immediately next to the magnet from each polarity. The presence of MMP was checked by a hanging-drop technique outlined in *Frankel et al.* [1997] (Figure S3-3). Glutaraldehyde were added to the collected water sample containing MMP at 1% final fixative concentration and filtered through 20 μm pore size membrane filter (discarded). The filtrate was further passed through three filters with pore size 0.8-8 μm (glass fiber pre-filter), 3 μm, and 1.6 μm. The three filters were freeze-dried immediately, folded and packed into a paleomagnetic cube, and kept in vacuum until, and in between, magnetic measurements.

An anhysteretic remanent magnetization (ARM) was imparted along a single axis (alternating field (AF) maximum = 200 mT, direct field = 0.1 mT) and AF demagnetized by 98 log-spaced steps along the same axis. The coercivity distribution from the demagnetization curve was calculated and modeled by CODICA and GECA [*Egli*, 2003] after the data has been smoothed by a robust loess (rloess) method in MATLAB (rloess span 0.1, mean misfit between raw and smoothed data = 2%). The raw data, the coercivity distribution calculated by CODICA, and the skewed generalized Gaussian (SGG) function fitted by GECA are shown in Figure S3-4 and the SGG parameters are summarized in Table S3-1. During data processing, all software suggested parameters were accepted and all five parameters controlling the SGG function were allowed to be optimized in one step.

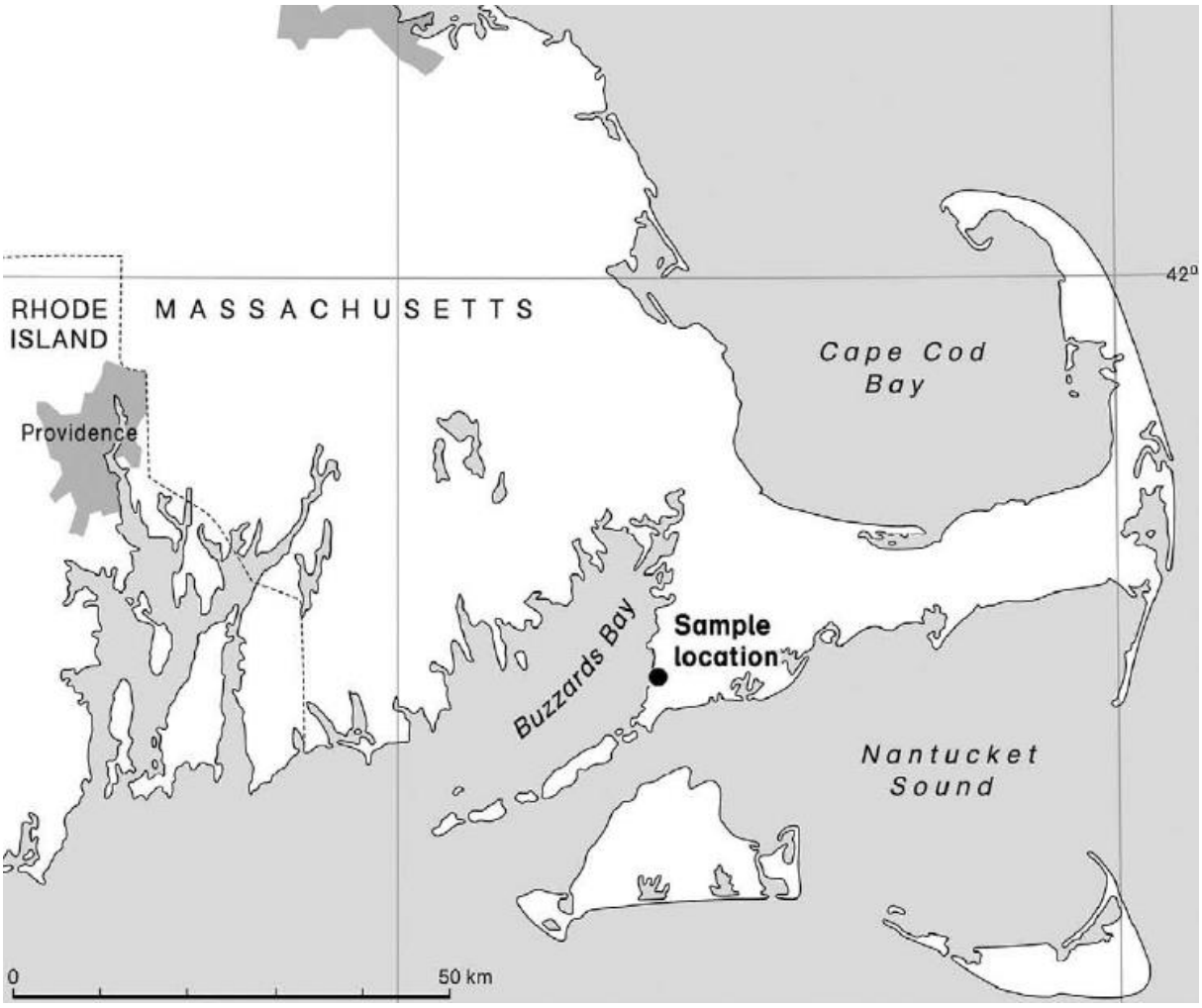

Figure S3-1| Sampling location (modified from Madsen et al. 2009)**.**

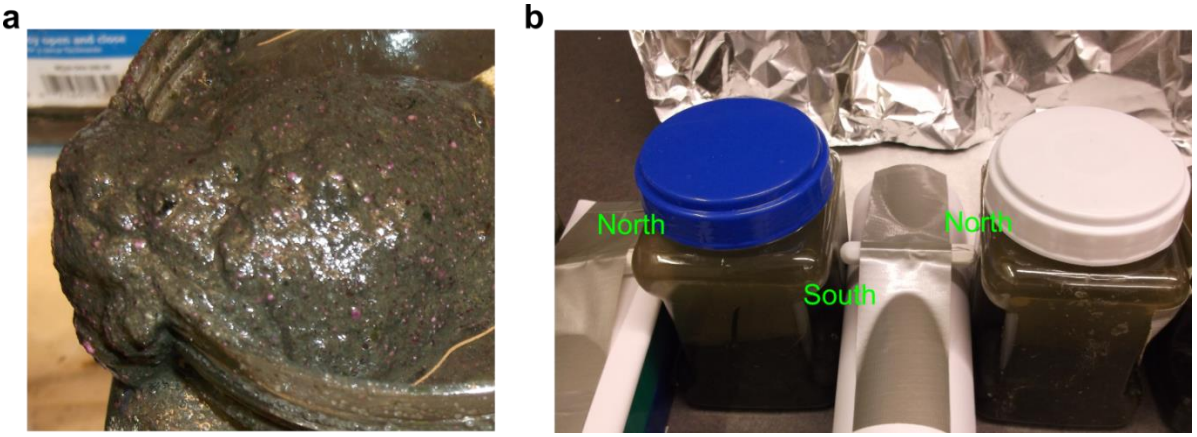

Figure S3-2| MMP enrichment. (a) Surface sediment from Little Sippewissett salt marsh containing abundant organic matter and visible purple aggregates of bacteria. (b) Setup for enrichment of MMP. The containers containing surface sediment and pond water were placed adjacent to one another with bar magnets in between with polarity as pictured. The polarities of the magnets were checked with a compass.

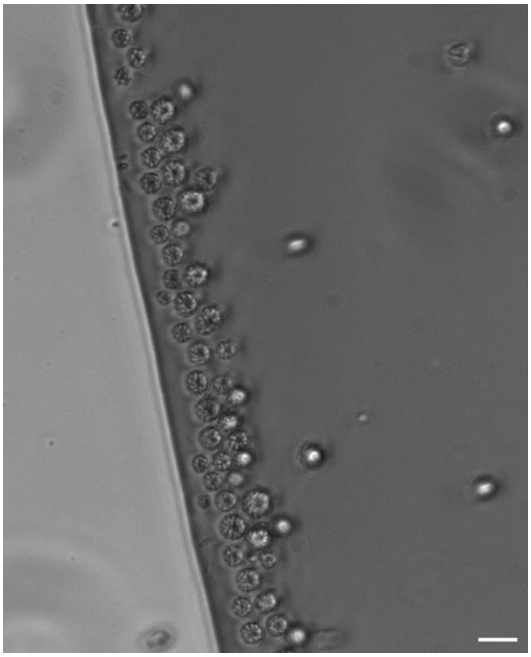

Figure S3-3| MMP hanging-drop observation. A light microscopy hanging-drop live MTB assay image on the sample collected after enrichment showing abundant MMP congregating along the water drop edge close to a magnet (not shown). Scale bar = 5 μm.

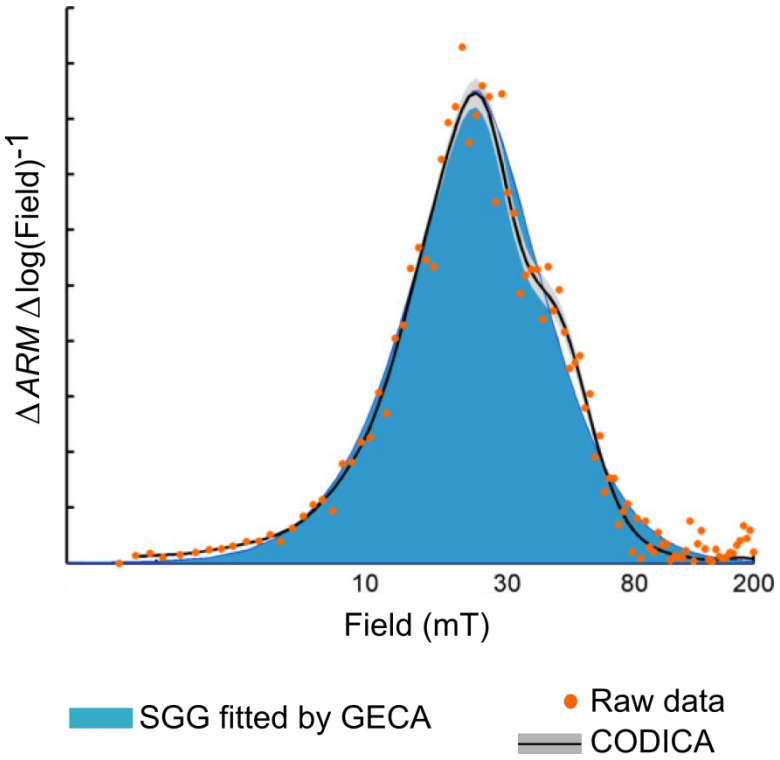

Figure S3-4| Measured and modeled (by CODICA and GECA) ARM coercivity distribution

Table S3-1| Corecivity distribution parameters					
[1]MF	[2]Fitting field range	GECA fitted SGG parameters			
(mT)	(mT)	μ	σ	q	p
23.36	1.76 – 192.8	1.538	0.2417	0.5747	1.868
[1]Median field calculated by CODICA					
[2]This is the entire range of field considered significant by GECA					

Chapter 4

A comparative multiproxy approach to address paleoredox change at the Paleocene-Eocene boundary, New Jersey Coastal Plain

Amy P. Chen[1], Edward D. Burton[2], Simon C. George[3], Paul P. Hesse[1], Peter Kraal[4], José M. Mogollón[4], David K. Potter[5], Julio Sepúlveda[6], Patrick Trimby[7], Nicole G.F. Vella[8]

Author affiliations

[1]Department of Environment & Geography, Macquarie University, North Ryde, Australia

[2]Southern Cross GeoScience, Southern Cross University, Lismore, Australia

[3]Department of Earth & Planetary Sciences, Macquarie University, North Ryde, Australia

[4]Department of Earth Sciences – Geochemistry, Utrecht University, Utrecht, The Netherlands

[5]Department of Physics, University of Alberta, Edmonton, Canada

[6]Earth, Atmospheric, & Planetary Sciences, Massachusetts Institute of Technology, Cambridge, U.S.A.

[7]Australian Centre for Microscopy and Microanalysis, The University of Sydney, Sydney, Australia

[8]Microscopy Unit, Faculty of Science, Macquarie University, North Ryde, Australia

Author contributions

A.P.C. initiated the project, conducted the measurements, provided the interpretations, and drafted the manuscript. E.D.B., P.K., and J.M.M. advised on and assisted in the inorganic geochemistry. S.C.G. and J.S. advised on and assisted in the organic geochemistry. D.K.P. advised on and assisted in RRM experiments. P.T. and N.G.F.V. advised on and assisted in electron microscopy. P.H. advised throughout. Everyone participated in discussion and manuscript revision.

Prepared for submission to *Paleoceanography*.

4.1 Abstract

The laminated Marlboro Clay unit on the New Jersey Coastal Plain (NJCP) contains an exceptional record of paleoenvironmental change and anomalous magnetic signal associated with the Paleocene Eocene Thermal Maxima (PETM). This study presents new data from trace metal (vanadium and molybdenum), iron species, biomarker (gammacerane, pristane and phytane), and magnetofossil abundance from the Millville site on the NJCP to assess paleoredox changes. In agreement with published nanofossil, foraminifera, and dinocyst data, these geochemical and magnetic results support a transition toward increased stratification and dysoxia coincident the abrupt warming. Moreover, the lack of concomitant molybdenum enrichment and an overall DOP of less than 0.3 indicate the lack of euxinia establishment. Importantly, we provide strong evidences for framboidal/cluster greigite particles as carrier of the anonymous magnetic signal by analytical microscopy, RRM, and ARM coercivity spectra unmixing for the first time. As such greigite particles most likely precipitated via organoclastic sulphate reduction in the fine-grained kaolinitic Marlboro Clay, they are not the product of comet impact plume condensates.

4.2 Introduction

Superimposed on the gradual warming trend from the late Paleocene (ca. 58 Ma) to Early Eocene Climatic Optimum (EECO; ca. 53.5 Ma) are pulses of short duration hyperthermals [Lourens *et al*., 2005; Nicolo *et al*., 2007]. The Paleocene-Eocene Thermal Maximum (PETM, ca. 55.8 Ma) is the earliest in this series of transient warming events, characterized by a ~2–8 ‰ negative stable carbon isotopic excursion (CIE) in marine and terrestrial records [e.g. Shackleton, 1986; Kennett and Stott, 1991; Koch *et al*., 1992; Thomas *et al*., 2002; Schmitz and Pujalte, 2003; McCarren *et al*., 2008; Handley *et al*., 2008; Wright and Schaller, 2013]. The CIE is indicative of ^{13}C-depleted carbon injection into the ocean and atmosphere and the most recent constraint on the timing and magnitude of the isotopically light carbon release came from expanded PETM records on the New Jersey Coastal Plain (NJCP) [Wright and Schaller, 2013]. By asserting that the rhythmic bedding in the kaolinite-rich Marlboro Clay in NJCP shallow marginal cores containing the CIE represents annual couplets, Wright and Schaller [2013] stated that the onset of CIE took place in 13 years. The authors further estimated the maximum magnitude of the CIE by proposing a logarithmic relationship between paleodepths and the magnitude of the CIE for six NJCP sites, with the extrapolated 0 m paleodepth CIE amounting to –20 ‰.

On the basis of this extremely short CIE onset duration, compared to previous estimates of ~750 y [Röhl *et al*., 2007] and ~30000 y [Murphy *et al*., 2010], and the large maximum CIE magnitude, Wright and Schaller [2013] single out two among several [e.g. Dickens *et al*., 1995; Katz *et al*., 2001; Kurtz *et al*., 2003; Higgins and Schrag, 2006; Pancost *et al*., 2007; Nisbet *et al*., 2009; Gu *et al*., 2011; Dickens, 2011; DeConto *et al*., 2012; see below] previously hypothesized isotopically light carbon sources: thermogenic methane from North Atlantic Igneous Province emplacement [Svensen *et al*., 2004; Maclennan and Jones, 2006; Storey *et al*., 2007] and cometary carbon [Kent *et al*., 2003; Cramer and Kent, 2005]. The latter was given preference because of the recent recognition that a substantial fraction of magnetization-carrying particles in the PETM Marlboro Clay has unclear origins [Wang *et al*., 2012]. The attribution of the fraction of magnetic particles having unclear origin as evidence of a comet impact is problematic, not least because Wang *et al*. (2012) had already pointed out the incompatibility between the observed grain size distribution and composition and those from the modeled outcome of impact plume condensates.

The fundamental question that remains, notwithstanding the attention Marlboro Clay's magnetic properties have garnered for more than a decade [Lanci *et al*., 2002; Kent *et al*., 2003; Kopp *et al*., 2007; Kopp *et al*., 2009; Lippert and Zachos, 2007; Schumann *et al*., 2008; Wang *et al*., 2012], is concerning the source of the magnetic particles that gave rise to the anomalous magnetic signal. This work aims to address this question with a variety of tools ranging from inorganic geochemistry, microscopy, to emergent magnetic characterizations. We demonstrate that it is possible to resolve the multiple sources of thus far inexplicable magnetization carrying-particles while accounting for those resembling fossilized magnetosomes (magnetofossils) produced by magnetotactic bacteria (MTB) found in previous studies [Kopp *et al*., 2007; Lippert and Zachos, 2007]. These intracellularly produced biogenic particles are thought to reflect an expansion of the suboxic zone on the North Atlantic margin setting conducive to their production by MTB and their subsequent preservation [Kopp *et al*., 2007, 2009; Lippert and Zachos, 2007; Dickens, 2008]. This change in paleoredox inferred from the presence of magnetofossils is corroborated by the benthic foraminiferal records [Stassen *et al*., 2012], though as the contribution of magnetofossils to the magnetic signal has been called into question, so is their redox significance. We therefore assess paleoredox change at NJCP by independent proxies, including lipid biomarker, degree of pyritization (DOP), and trace metal analyses.

4.3 Material and methods

4.3.1 Site description

Samples investigated in this study came from the Millville site located in the Salisbury Embayment (Figure 1). Millville is one of the continuously cored sites on the NJCP as part of ODP Leg 174 AX. The paleodepositional water depth for the Marlboro Clay at Millville is estimated at ~60 m at the CIE onset based on 2D backstripping and projection onto a common dip line using a slope gradient of 1:1,000 determined for the northern Salisbury Embayment [Wright and Schaller, 2013]. At this site, the CIE interval (maximum $\Delta^{13}\delta C$ = 3.9 ‰; Wright and Schaller, 2013) spans 273.96 – ~279 m, where the top is capped by an unconformity [Kopp *et al*., 2009; Harris *et al*., 2010; Wright and Schaller, 2013].

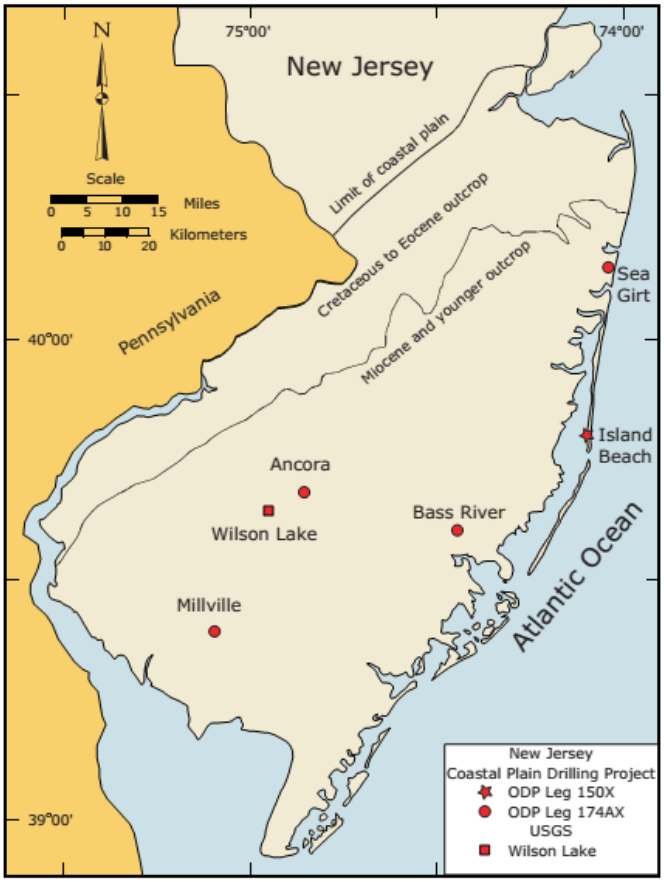

Figure 4-1: Millville site location map (taken from A. Harris, 2010).

4.3.2 Magnetic characterizations

To determine the magnetic coercivity distribution, anhysteretic remanent magnetization (ARM) imparted on seven Millville specimens (AF_{max}=200 mT, DC=0.1 mT) was AF

demagnetized and measured in 98 log-spaced steps by a SQUID rock magnetometer (2G Corp. SRM). Two samples each were selected from pre- and post-CIE, while three samples were selected, spaced at quasi-regular intervals from within the CIE. The resultant ARM spectra were modeled with CODICA and GECA, with the latter resolving the coercivity distribution into individual magnetic components characterized by generalized skewed Gaussian functions [Egli, 2003]. Rotational remanent magnetization (RRM; AF_{max}=80 mT, ~95 r.p.s., frequency=60 Hz) and rotational ARM (rARM; AF_{max}=80 mT, ~95 r.p.s., frequency=60 Hz, DC=70 μT) were imparted on Millville samples by a rotational magnetizer described in Stephenson and Molyneux [1987] and measured by a calibrated spinner magnetometer. The effective gyrofield, rB_g (in μT), was calculated as rB_g = 70×(RRM/rARM).

4.3.3 Inorganic geochemistry

Following the sequential iron extraction protocol of Poulton and Canfield [2005], five operationally defined iron pools were determined from each powdered Millville sample: (1) carbonate Fe (e.g. siderite, ankerite) extracted by pH 4.5 Na Acetate for 24 hr., (2) Fe oxide (e.g. ferrihydrite, lepidocrocite) extracted by hydroxylamine-HCl for 48 hr., (3) Fe oxide (e.g. goethite, akaganéite, hematite) extractable by dithionite for 2 hr., (4) Fe oxide (e.g. magnetite) extracted by ammonium oxalate in 6 hr., (5) poorly reactive Fe in sheet silicate extracted by boiling 12 N HCl. In addition, pyritic Fe (Fe_{PY}) was calculated stoichiometrically from the chromium reducible sulfur fraction [Canfield, 1986]. Highly reactive Fe (Fe_{HR}) is defined as the sum of the Fe pools from sequential extraction steps (1) through (4) plus pyritic Fe. Unreactive Fe is taken as the difference between the total Fe (Fe_T; determined from 1:3 Nitric/HCl digestion and analysis by an ICP-MS) and the sum of the above five iron pools and pyritic Fe. The DOP is defined as DOP=Fe_{PY}/(Fe_{PY} + Fe_R), where Fe_R is the sum of all reactive iron pools from sequential extraction steps (1) through (5). Lastly, the abundance of aluminum, vanadium, and molybdenum were determined by 1:3 Nitric/HCl digestion and analysis by an ICP-MS.

4.3.4 Organic geochemistry

Powdered Millville samples were manually extracted (with repeated vortex, sonication, and centrifugation) by a solvent mixture of dichloromethane:methanol in a 9:1 (v/v) ratio. The concentrated total lipid extract (TLE) was separated into asphaltenes and a maltene fraction by elution with hexane and DCM, respectively. Elemental sulfur was removed from the maltene fraction using HCl-activated copper beads. Gas chromatography-mass spectrometry

(GC-MS) was used to identify isoprenoid hydrocarbons pristane and phytane, while GC-MS metastable reaction monitoring (MRM-GC-MS) was used to identify gammacerane and hopane used in the calculation of the redox-sensitive gammacerane index defined as gammacerane/(gammacerane + 17α, 21ßC$_{30}$hopane)×100.

4.3.5 Microscopy

For scanning electron microscopy (SEM), one set of sediments were embedded in LR White resin and cut into ~2 µm thick sections using a microtome. The sections were deposited onto a stub lined with carbon tape and subsequently carbon coated. Images formed from backscattered electrons (BSE) and energy-dispersive x-ray spectra (EDS) were taken by a JEOL JSM-6400 LA field emission SEM equipped with an EX-2300 BU EDS analyser operating at 15 keV. One sample from within the CIE interval was magnetically extracted with a custom built magnetic extractor modeled after the unit described in Reynolds *et al*. [2001]. The extracted fraction was made into a polished thin section (by Burnham Petrographics LLC) and coated with carbon. BSE image of this sample was collected by a Zeiss Ultra Plus SEM operating at 20 keV.

4.4 Results

4.4.1 ARM coercivity distribution and RRM

Figure 4-2 shows ARM coercivity distribution for seven Millville samples. For four samples from pre- and post- CIE intervals, the bulk ARM signal is one to two orders of magnitude smaller than the three samples from syn-CIE (Table 1). As such, the coercivity distribution from the four pre- and post-CIE samples are too noisy for coercivity distribution un-mixing. For the three syn-CIE samples, CODICA calculated coercivity distribution on log-field scale from minimally robust LOESS (rloess; in MATLAB) smoothed raw data (rloess span and mean misfit reported in Table 1) are modeled as the linear combinations of four components using GECA: D+Ex, M, G, and H. Component D+Ex is thought to represent detrital and/or extracellularly produced magnetic particles. Component M can represent magnetosomes of both greigite and magnetite composition with aspect ratio (width/length) <0.4 from uncultivated magnetotactic bacteria (see Chapter 2). Component G most likely represents elongated magnetosomes or authigenic greigite particles (see Chapter 2). Component H categorizes magnetic particles with a high coercivity, most likely from canted antiferromagnets and/or poorly ordered ferromagnets. For the three samples from syn-CIE, component M accounts for 22.2% to 37.3% of the overall ARM, while component G accounts

for 54% to 62.7% of the total ARM. Compared to component M and G, component D+Ex and H both contribute minimally to the total ARM (Table 1).

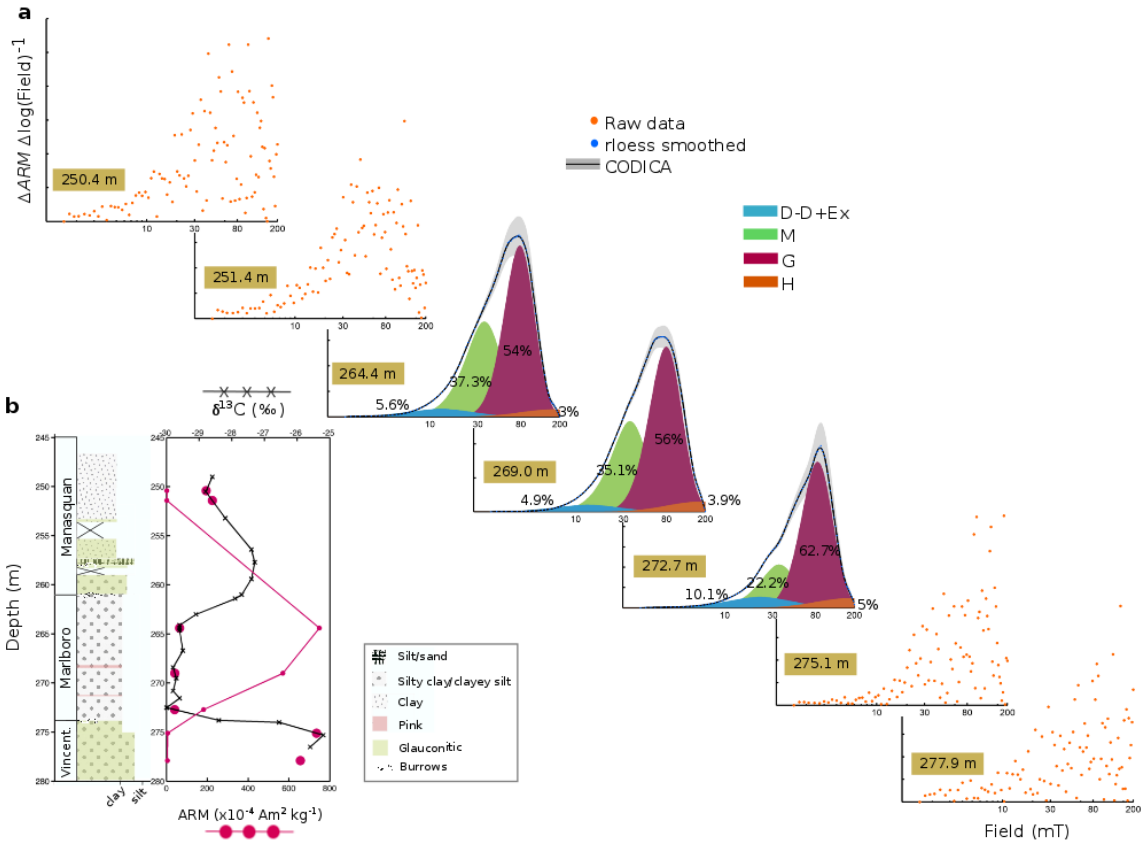

Figure 4-2: ARM coercivity distribution. (**a**) ARM coercivity distribution for the seven Millville samples marked as red dots in (**b**). For the four samples pre- (277.9 m and 275.1 m) and post- (251.4 m and 250.4 m) CIE, the numerical derivative of raw data (shown in orange dots) are too noisy for coercivity component analyses. ARM coercivity distribution for the three syn-CIE samples (272.7 m, 269.0 m, 264.4 m) were modeled as the linear combination of four magnetic components D-Ex, M, G, and H (see text and Table 1). (**b**) carbon isotope stratigraphy (black line) and lithostratigraphy (redrawn after Kopp *et al*., 2009), and ARM (red line, acquired with AF_{max}=200 mT, DC=0.1 mT).

Table 4-1|*ARM* coercivity distribution parameters

	[1]*ARM*	[1]χ_{ARM}	robust loess span	Mean misfit %	[2]*MF*	[3]Field range	[4]GECA 4 skewed Gaussian end members						
	($Am^2\ kg^{-1}$)	($m^3\ kg^{-1}$)			(mT)	(mT)	End Members	% Contribution	μ	σ	q	p	χ^2/DF [Confidence Interval]
250.4 m	1.94×10^{-6}	2.44×10^{-8}											
251.4 m	1.61×10^{-6}	2.02×10^{-8}											
264.4 m	7.49×10^{-4}	9.41×10^{-6}	0.17	0.7	56.0	1.56 – 197.7	D+Ex	5.6	1.103	0.335	0.771	1.838	0.6 [0.37, 1.9]
							M	37.3	1.53	0.2	0.66	1.89	
							G	54	1.893	0.158	0.739	1.994	
							H	3	2.25	0.335	1	2	
269.0 m	5.70×10^{-4}	7.16×10^{-6}	0.17	0.53	57.9	1.56 – 197.7	D+Ex	4.9	1.118	0.335	0.771	1.838	1 [0.31, 2]
							M	35.1	1.53	0.2	0.66	1.89	
							G	56	1.9	0.172	0.739	1.994	
							H	3.9	2.25	0.335	1	2	
272.7 m	1.81×10^{-4}	2.27×10^{-6}	0.17	0.62	66.3	1.56 – 197.7	D+Ex	10.1	1.346	0.335	0.771	1.838	0.44 [0.34, 1.9]
							M	22.2	1.53	0.2	0.66	1.89	
							G	62.7	1.923	0.165	0.739	1.994	
							H	5	2.25	0.335	1	2	
275.1 m	5.04×10^{-6}	6.33×10^{-8}											
277.9 m	4.46×10^{-6}	5.61×10^{-8}											
							[5]Average *ARM* D+Ex (*n*=28)		1.346±0.072	0.335 ± 0.042	0.771±0.144	1.838±0.105	
							[6]Average *ARM* M (*n*=10)		1.53± 0.034	0.20± 0.026	0.66± 0.048	1.89± 0.11	
							[7]Average *ARM* G (*n*=26)		1.838±0.046	0.122± 0.037	0.739±0.132	1.994±0.066	
							[8]H		2.2	0.2	1	2	

[1]Acquired with AF_{max}=200 mT, *DC*=0.1 mT
[2]Median field (*MF*) calculated by CODICA after accepting the software suggested exponent for the scale transformation power function, removal of outliers, and correlation length of residual
[3]The range of field considered significant and used for the analyses by GECA
[4]Analyses in GECA initiated by the parameters for D+Ex, M, G, and H listed at the bottom of this table with their amplitude (a) adjusted such that the linear combination of all four components approximately matches the overall *ARM* coercivity distribution for each sample. Optimization performed in one iteration by fixing all parameters (20 in total) except for a and μ for component D-Ex, and a, μ , *and* σ for component G.
[5]Average ± standard deviation of component D-D+Ex (abbreviated here as D+Ex) from Egli, 2004
[6]Average ± standard deviation from Chapter 2
[7]Average ± standard deviation of component BH-BI (renamed here as G) from Egli, 2004
[8]Taken from Egli, 2004

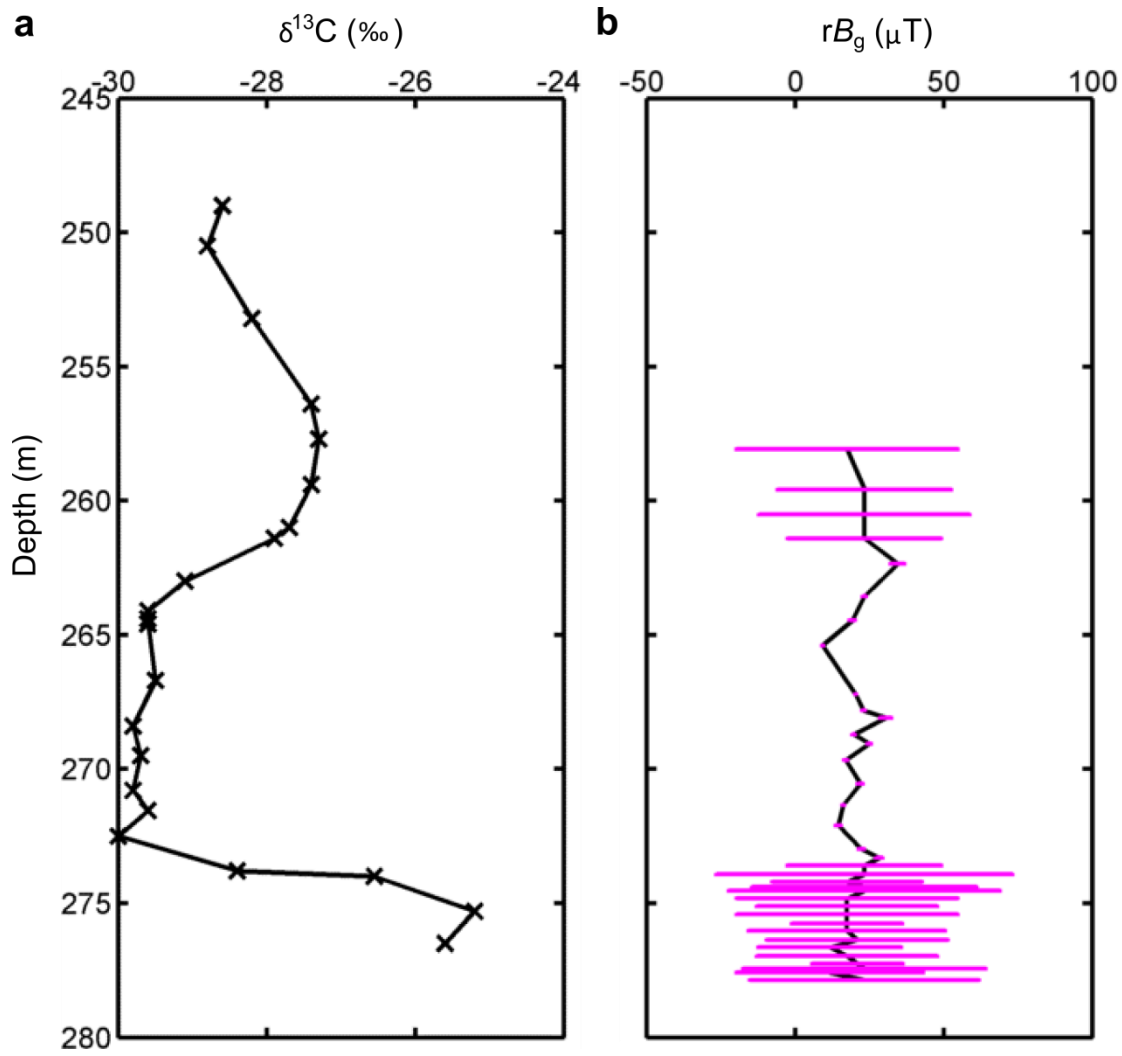

Figure 4-3: Effective gyrofield as a function of depth. (**a**) carbon isotope stratigraphy (redrawn after Kopp *et al*., 2009). (**b**) effective gyrofield as a function of depth with propagated error in magenta.

Figure 4-3 shows the effective gyrofield as a function of depth. The weak magnetization of Millville samples outside of the CIE interval contribute to the large error in rB_g. Within the CIE interval, both RRM and rARM signal are well above the spinner magnetometer instrument limit, and hence the resultant rB_g values, ranging between 9 to 30 μT, have markedly smaller errors.

4.4.2 Inorganic geochemistry

Figure 4-4 summarizes the results for sequential iron extraction performed on Millville samples. Hydroxylamine-HCl and dithionite extractable iron both show concomitant large increases in concentration at the onset of the CIE, whereas the other iron species (extractable by Na Acetate, oxalate, and boiling HCl and pyritic Fe) do not. Fe_{HR}/Fe_T increases to >0.38 at the onset of CIE and remains elevated syn-CIE, suggestive of a transition toward a deoxygenated environment (Figure 4-5; Wijsman *et al*., 2001; Poulton and Canfield, 2011). In contrast to both V/Al (Figure 4-6, normalized to aluminum to account for variable carbonate and opal content, Tribovillard *et al*., 2006) and Fe_{HR}/Fe_T (Figure 4-5), DOP (Figure 4-5) and Mo/Al depth profiles do not show an increase at the onset of CIE. The enrichment in vanadium in the absence of molybdenum enrichment is consistent with a transition toward a deoxygenated environment (Tribovillard *et al*., 2006). While the invariant DOP may at first suggest little change in Fe_{PY} relative to Fe_{HR}, it is possible that pyrite has subsequently oxidized to form part of the labile and crystalline Fe oxide pools that were extracted in steps 2 and 3 during sequential Fe extraction. At the same time, while part of the observed increase in Fe_{HR} relative to Fe_T can be attributed to deoxygenation, the effect of pyrite oxidation post-deposition may also play a role.

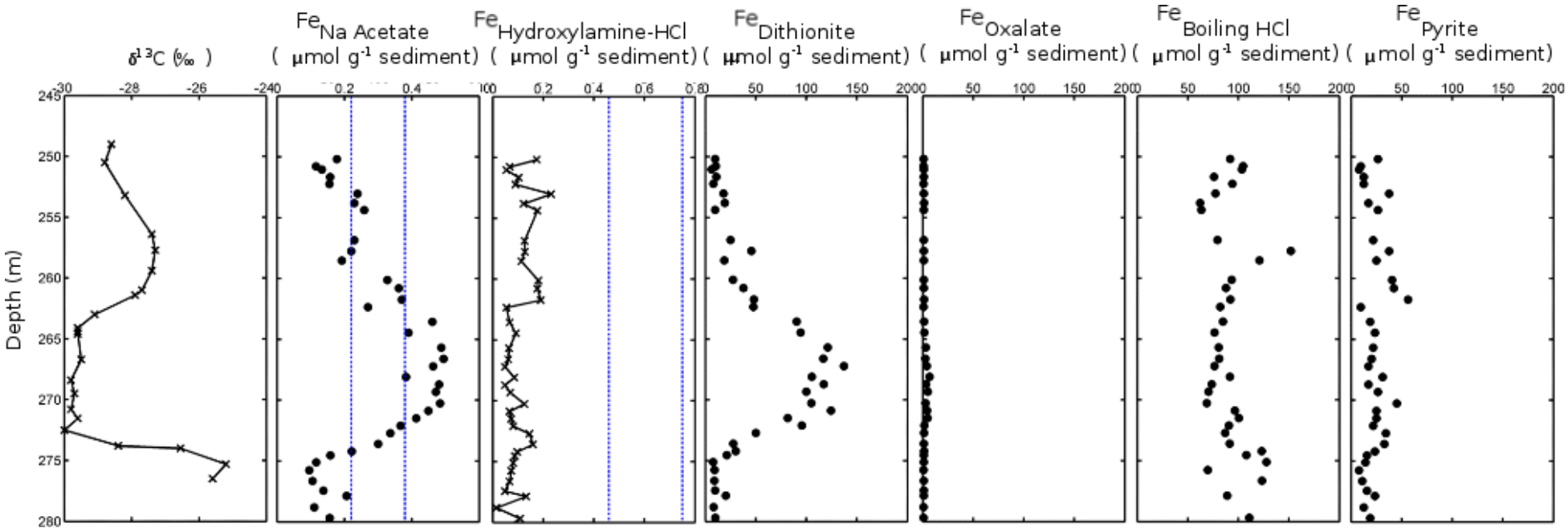

Figure 4-4: Fe concentration determined from sequential Fe extraction. Carbon isotope stratigraphy (redrawn after Kopp *et al.*, 2009).

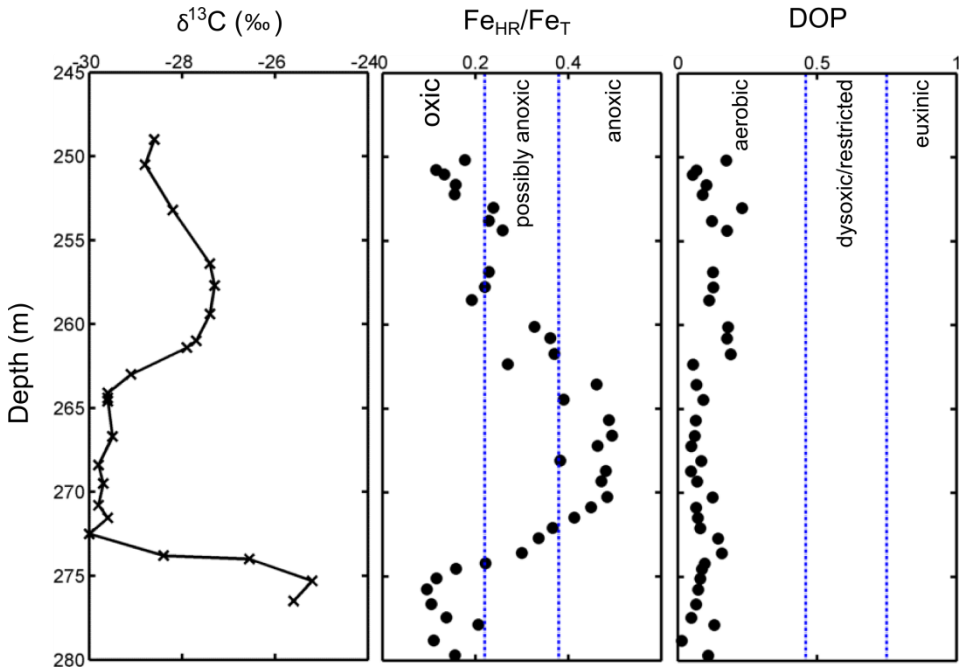

Figure 4-5: Redox-sensitive Fe parameters. Carbon isotope stratigraphy redrawn after Kopp *et al*., 2009.

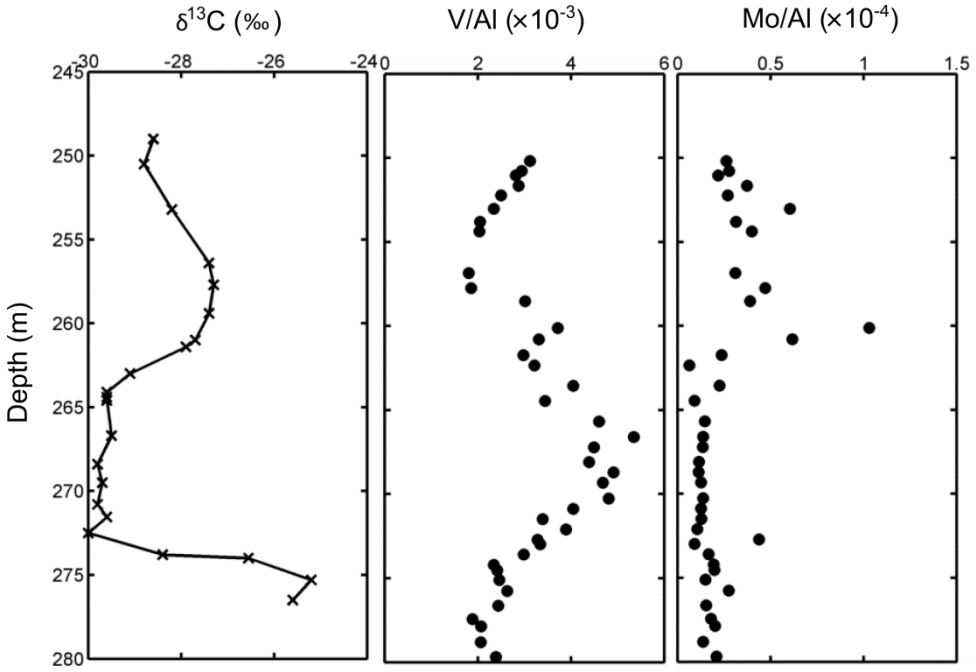

Figure 4-6: Trace metal depth profile. Carbon isotope stratigraphy (redrawn after Kopp *et al*., 2009).

4.4.3 Gammacerane index and pristane to phytane ratio

The gammacerane index does not display significant changes across the CIE transition (Figure 4-7). This lack of change is either indicative of the lack of change in the population of bacteriovorous cilates typically found in the chemocline of stratified water column, or may suggest the lack of diagenetic conversion from tetrahymanol, the parent compound of the above mentioned cilates, to gammacerane (ten Haven *et al*., 1989; Sinninghe Damsté *et al*., 1995). Another redox sensitive proxy, the pristane to phytane ratio, Pr/Ph, predicated on the preferential conversion of chlorophyll phytyl produced by photoautotrophs to phytane under reducing condition and to pristane under oxic conditions (Peters *et al*., 2005), indicates a switch toward a more reducing condition at the onset of CIE (Figure 4-7). However, this change is not sustained within the CIE interval.

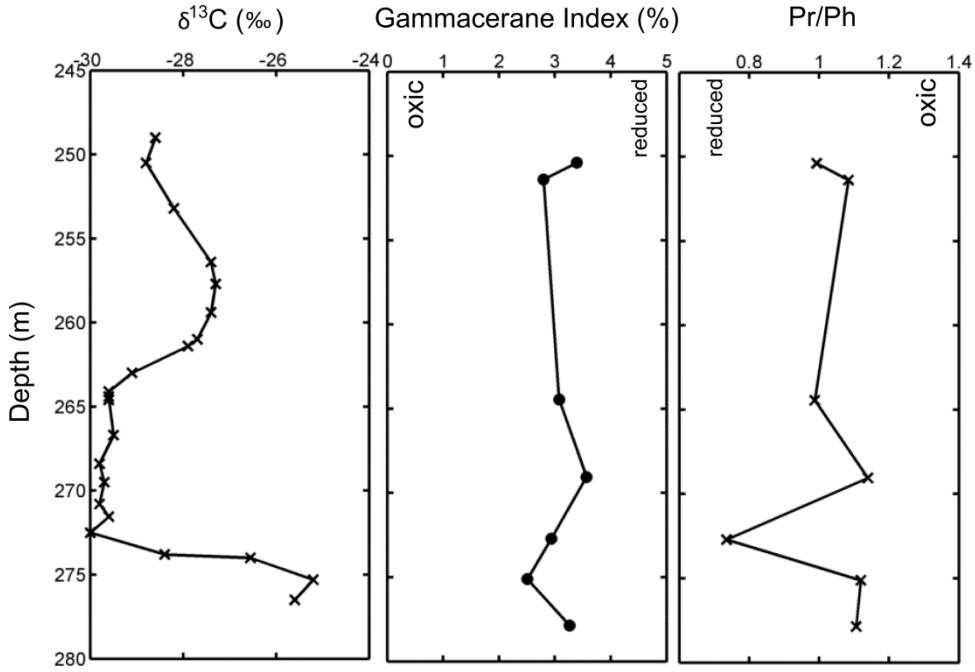

Figure 4-7: Gammacerane index and pristane to phytane ratio. Carbon isotope stratigraphy redrawn after Kopp *et al*., 2009.

4.4.4 Iron sulphide framboids/clusters

Figure 4-8 shows SEM BSE images of framboids and clusters in syn-CIE Millville clay. In addition to framboids and clusters found in clay matrix (representative examples shown in Figure 4-8a-e), multiple foraminifera tests containing iron- and sulfur-rich framboids and clusters were found in the magnetically extracted fraction (an example is shown in Figure 4-8f). EDS point analyses performed on 134 nearly all independent framboids and clusters

revealed that the framboids and clusters are rich in iron and sulfur, though minor amounts of other elements were also detected, likely from the surrounding clay and/or foraminifera tests. Excluding Fe, S, and C, the latter of the three being the coating material during sample preparation, the contribution from other elements contributed between 1.3% to 55.1% of the x-ray signal (the minimum and maximum of the scale bar in Figure 4-9, respectively). Fe and S atomic percent contribution results, summarized in Figure 4-9, suggest that some of the analysed framboids and clusters can be greigite (Fe_3S_4) in composition.

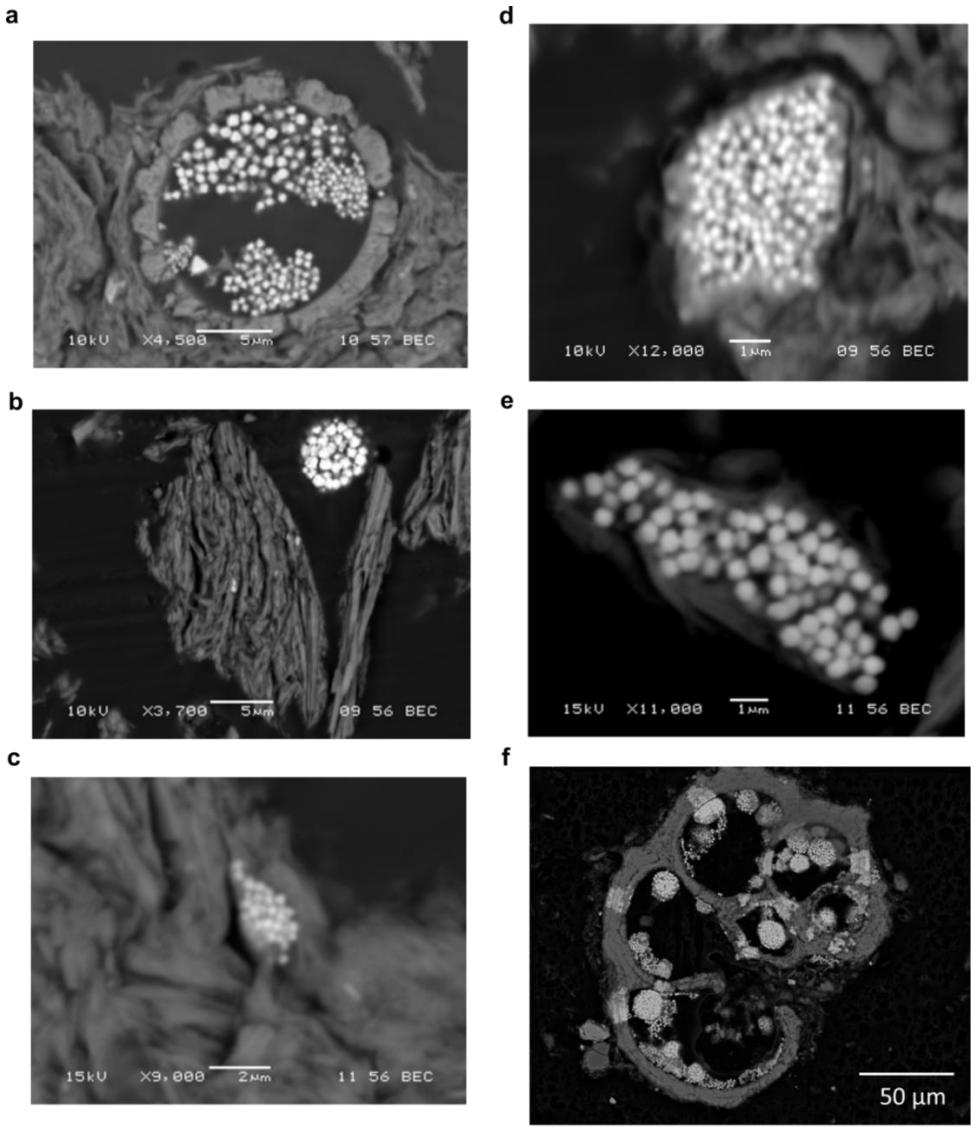

Figure 4-8: SEM BSE images. (**a**) to (**e**) BSE images of ~2 µm thick sections of syn-CIE Millville clay. (**f**) An BSE image of magnetically extracted fraction from a syn-CIE sample. In all pictures, backscattered electrons show differences in composition. Bright colour regions are enriched in Fe and S.

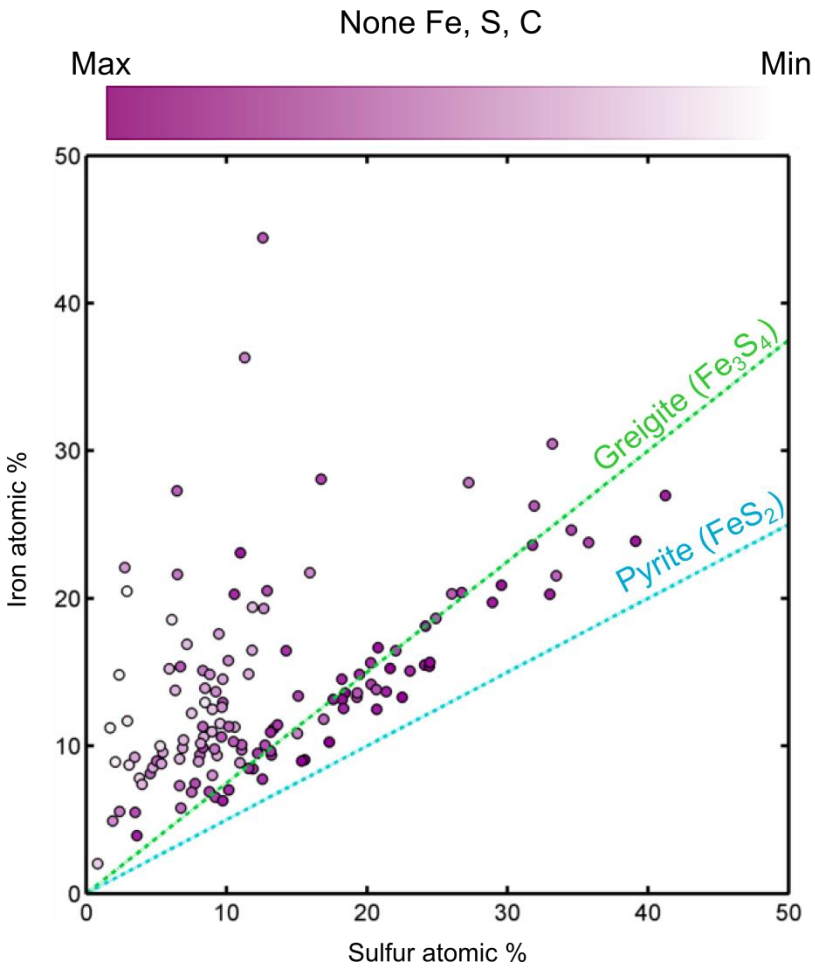

Figure 4-9: Fe and S content of framboids and clusters determined by EDS. Data were collected from 134 non-overlapping point analyses from nearly all independent framboids and clusters (representative images shown in Figure 4-8). Green and blue dashed lines indicate stoichiometric greigite and pyrite compositions, respectively. The purple shading within the dots indicate the proportion of non-Fe, S, and C content of the point analysis features as indicated by the scale bar on the top of the graph (Min = 1.3%; Max = 55.1%).

4.5 Discussion

As a whole, results from this study suggest that greigite is a heretofore overlooked magnetic signal carrier in syn-CIE Marlboro Clay. While the number of analyzed framboids/clusters matching the expected greigite composition may seem few (Figure 4-9), the EDS results need to be interpreted in the context of necessary magnetic particle concentration required to give rise to the observed anomaly. Syn-CIE Marlboro Clay typically has a mass normalized saturation magnetization (Ms) of ~15×10^{-3} Am^2 kg^{-1} (Kent *et al.*, 2003; Kopp *et al.*, 2007; Lippert and Zachos, 2007), which translates to a mass concentration of 254 ppm (Ms of greigite = 59 Am^2 kg^{-1}, Chang *et al.*, 2008) or a volume concentration of 87 ppm (Marlboro Clay density = 1.38 g cm^{-3}, Scott, 2005; greigite density

= 4.049 g cm^{-3}) if all of the magnetic particles in the clay are assumed to be greigite in a simple approximation.

The presence of greigite in Marlboro Clay is corroborated by a number of characterizations independent from the EDS results mentioned above. In terms of ARM coercivity distribution analyses, component G (accounting for between 54 to 62.7% of the overall ARM signal, Figure 4-2 and Table 1) can be taken to be suggestive of authigenic greigite framboids. While this particular component has been linked to particles synthesized via biological control (*e.g.* Egli, 2004, Lascu *et al.*, 2010; Kodoma *et al.*, 2013), it was recently pointed out that the small dispersion factor associated with this component can be due to authigenic greigite framboids/clusters and/or elongated magnetofossils with aspect ratio (width/length) ~<0.4 (Chapter 2). The latter has been shown to constitute a comparatively minor fraction of the imaged (by TEM) putative magnetofossil assemblage (see Figure 5 in Kopp *et al.*, 2007 and Figure 4 in Lippert and Zachos, 2007). As such, component G can be reasonably attributed to framboidal/cluster greigite particles formed by organoclastic sulfate reduction (Rowan and Roberts, 2006). The presence of greigite in the NJ shelf sediments dating to Plio-Pleistocene (Oda and Torii, 2004) and Micene (Nilsson et al., 2013) have been inferred by two previous studies and in both a component similar to G were linked to greigite with supporting mineral magnetic results. The lithological transition from silty-clay to kaolinite, thought to reflect increased exhumation and erosion of Cretaceous laterites (John *et al.*, 2006), is likely to be conducive to framboidal greigite formation since the kaolinite provides an environment with low advection (Rickard, 2012). In terms of RRM, the measured rB_g in the range of 9 to 30 μT for Marlboro Clay is consistent with having a mixture of magnetofossils (magnetosomes from uncultivated MTB have $0<rB_g<7.3$ μT, Chapter 3) and greigite framboids/clusters (variable rB_g, though framboidal/cluster-bearing sediments have rB_g in the range of 77 μT (Hu *et al.*, 2002) to ~1100 μT (Stephenson and Snowball, 2001)) as suggested by the ARM coercivity distribution analyses (Figure 4-2 and Table 1). Two previous studies

A number of prior studies have provided insight into the paleoenvironmental changes that took place at the Paleocene-Eocene boundary on the New Jersey Coastal Plain. Highly diverse mesotrophic nanofossils increased in abundance at the onset of the CIE and persisted through the carbon isotopic excursion interval in contrast to lowered oligotrophic nanofossil abundance (Gibbs *et al.*, 2006). In the foraminifera records, the major change at the Paleocene-Eocene boundary is the replacement of a benthic foraminifera assemblage typically associated with oxic and outer neritic settings by opportunistic benthic foraminifera

associated with stratification and dysoxia (Stassen *et al*., 2012). At the same time, heterotrophic and low-salinity-tolerant dinocysts was found to have flourished (Sluijs *et al*., 2007; Stassen *et al*., 2012). The results in this study are in general agreement with the paleoenvironmental changes suggested by the above biotic responses. At the Millville site, while the magnetofossil abundance could not be determined pre-CIE and post-CIE due to the weak signal, 22.2% to 37.3% of the overall ARM signal can be accounted for by magnetofossils syn-CIE. Since MTB that produce the magnetofossils thrive at the boundary of oxic-anoxic-transition both in the water column and in the sediment (Lefévre and Bazylinski, 2013), and suboxia generally favors magnetofossil preservation, the presence of magnetofossils supports increased stratification either due to increased nutrient supply and eutrophication, increased freshwater input, and/or warming and reduced dissolved oxygen solubility. In corroboration, the enhanced vanadium, reactive Fe, and pristane concentration suggest a transition toward deoxygenation. Furthermore, the lack of concomitant enrichment in molybdenum as well as the low DOP value (< 0.3) suggest euxinia was not established, which is in agreement with abundant opportunistic benthic foraminifera (Stassen *et al*., 2012).

4.6 Conclusions

A multiproxy approach was employed to assess the paleoenvironmental change at the New Jersey Coastal Plain at the Paleocene-Eocene boundary. Magnetofossil abundance, vanadium enrichment, reactive iron concentration, and, to a more limited extent, pristane concentration from this study are in agreement with a transition toward increased stratification and dysoxia coincident with the abrupt warming indicated by previously published nanofossil, foraminifera, and dinocyst records. Furthermore, the lack of concomitant molybdenum enrichment and an overall DOP of less than 0.3 indicate the lack of euxinia establishment. Importantly, we provide strong evidences for framboidal/cluster greigite particles as carrier of the anonymous magnetic signal by analytical microscopy, RRM, and ARM coercivity spectra unmixing for the first time.

Acknowledgements

This work was supported by the Post-cruise Special Analytical Funding from the Australian-New Zealand IODP Consortium and Post Graduate Research Fund from Macquarie

University. The authors gratefully acknowledge Jim Browning, Ken Miller, and Marie-Pierre Aubry for assistance at the Rutgers Core Repository and helpful discussions.

References

Canfield, D. E., R. Raiswell, J. T. Westrich, C. M. Reaves, and R. A. Berner (1986), The use of chromium reduction in the analysis of reduced inorganic sulfur in sediments and shales, *Chem. Geol.*, *54*(1-2), 149–155, doi:10.1016/0009-2541(86)90078-1.

Chang, L., A. P. Roberts, Y. Tang, B. D. Rainford, A. R. Muxworthy, and Q. Chen (2008), Fundamental magnetic parameters from pure synthetic greigite (Fe_3S_4), *J. Geophys. Res.*, *113*(B6), doi:10.1029/2007JB005502.

Cramer, B. S., and D. V. Kent (2005), Bolide summer: The Paleocene/Eocene thermal maximum as a response to an extraterrestrial trigger, *Palaeogeogr. Palaeoclimatol. Palaeoecol.*, *224*(1-3), 144–166, doi:10.1016/j.palaeo.2005.03.040.

DeConto, R. M., S. Galeotti, M. Pagani, D. Tracy, K. Schaefer, T. Zhang, D. Pollard, and D. J. Beerling (2012), Past extreme warming events linked to massive carbon release from thawing permafrost, *Nature*, *484*(7392), 87–91, doi:10.1038/nature10929.

Dickens, G. R., J. R. O'Neil, D. K. Rea, and R. M. Owen (1995), Dissociation of oceanic methane hydrate as a cause of the carbon isotope excursion at the end of the Paleocene, *Paleoceanography*, *10*(6), 965–971, doi:10.1029/95PA02087.

Dickens, G. R. (2008), Palaeoclimate: The riddle of the clays, *Nat. Geosci.*, *1*(2), 86–88, doi:10.1038/ngeo118.

Dickens, G. R. (2011), Down the Rabbit Hole: toward appropriate discussion of methane release from gas hydrate systems during the Paleocene-Eocene thermal maximum and other past hyperthermal events, *Clim. Past*, *7*(3), 831–846, doi:10.5194/cp-7-831-2011.

Egli, R. (2003), Analysis of the field dependence of remanent magnetization curves, *J. Geophys. Res.*, *108*(B2), doi:10.1029/2002JB002023.

Gibbs, S. J., T. J. Bralower, P. R. Bown, J. C. Zachos, and L. M. Bybell (2006), Shelf and open-ocean calcareous phytoplankton assemblages across the Paleocene-Eocene Thermal Maximum: Implications for global productivity gradients, *Geology*, *34*(4), 233, doi:10.1130/G22381.1.

Gu, G., G. R. Dickens, G. Bhatnagar, F. S. Colwell, G. J. Hirasaki, and W. G. Chapman (2011), Abundant Early Palaeogene marine gas hydrates despite warm deep-ocean temperatures, *Nat. Geosci.*, *4*(12), 848–851, doi:10.1038/ngeo1301.

Harris, A. (2010), Integrated sequence stratigraphy of the Paleocene-Lowermost Eocene, New Jersey coastal plain: implications for eustatic and paleoceanographic change, Rutgers, The State University of New Jersey, New Brunswick.

Handley, L., P. N. Pearson, I. K. McMillan, and R. D. Pancost (2008), Large terrestrial and marine carbon and hydrogen isotope excursions in a new Paleocene/Eocene boundary section from Tanzania, *Earth Planet. Sci. Lett.*, *275*(1-2), 17–25, doi:10.1016/j.epsl.2008.07.030.

Higgins, J. A., and D. P. Schrag (2006), Beyond methane: Towards a theory for the Paleocene–Eocene Thermal Maximum, *Earth Planet. Sci. Lett.*, *245*(3-4), 523–537, doi:10.1016/j.epsl.2006.03.009.

Hu, S., A. Stephenson, and E. Appel (2002), A study of gyroremanent magnetisation (GRM) and rotational remanent magnetisation (RRM) carried by greigite from lake sediments, *Geophys. J. Int.*, *151*(2), 469–474, doi:10.1046/j.1365-246X.2002.01793.x.

John, C. M., N. R. Banerjee, F. J. Longstaffe, C. Sica, K. R. Law, and J. C. Zachos (2012), Clay assemblage and oxygen isotopic constraints on the weathering response to the Paleocene-Eocene thermal maximum, east coast of North America, *Geology*, *40*(7), 591–594, doi:10.1130/G32785.1.

Katz, M. E., B. S. Cramer, G. S. Mountain, S. Katz, and K. G. Miller (2001), Uncorking the bottle: What triggered the Paleocene/Eocene thermal maximum methane release?, *Paleoceanography*, *16*(6), 549–562, doi:10.1029/2000PA000615.

Kennett, J. P., and L. D. Stott (1991), Abrupt deep-sea warming, palaeoceanographic changes and benthic extinctions at the end of the Palaeocene, *Nature*, *353*(6341), 225–229, doi:10.1038/353225a0.

Kent, D. V., B. S. Cramer, L. Lanci, D. Wang, J. D. Wright, and R. Van der Voo (2003), A case for a comet impact trigger for the Paleocene/Eocene thermal maximum and carbon isotope excursion, *Earth Planet. Sci. Lett.*, *211*(1-2), 13–26, doi:10.1016/S0012-821X(03)00188-2.

Koch, P. L., J. C. Zachos, and P. D. Gingerich (1992), Correlation between isotope records in marine and continental carbon reservoirs near the Palaeocene/Eocene boundary, *Nature*, *358*(6384), 319–322, doi:10.1038/358319a0.

Kopp, R. E., T. D. Raub, D. Schumann, H. Vali, A. V. Smirnov, and J. L. Kirschvink (2007), Magnetofossil spike during the Paleocene-Eocene thermal maximum: Ferromagnetic resonance, rock magnetic, and electron microscopy evidence from Ancora, New Jersey, United States, *Paleoceanography*, *22*(4), doi:10.1029/2007PA001473.

Kopp, R. E., D. Schumann, T. D. Raub, D. S. Powars, L. V. Godfrey, N. L. Swanson-Hysell, A. C. Maloof, and H. Vali (2009), An Appalachian Amazon? Magnetofossil evidence for the development of a tropical river-like system in the mid-Atlantic United States during the Paleocene-Eocene thermal maximum? *Paleoceanography*, *24*(4), doi:10.1029/2009PA001783.

Kurtz, A. C., L. R. Kump, M. A. Arthur, J. C. Zachos, and A. Paytan (2003), Early Cenozoic decoupling of the global carbon and sulfur cycles: PALEOGENE C AND S CYCLES, *Paleoceanography*, *18*(4), doi:10.1029/2003PA000908.

Lanci, L. (2002), Detection of Late Cretaceous and Cenozoic sequence boundaries on the Atlantic coastal plain using core log integration of magnetic susceptibility and natural gamma ray measurements at Ancora, New Jersey, *J. Geophys. Res.*, *107*(B10), doi:10.1029/2000JB000026.

Lascu, I., S. K. Banerjee, and T. S. Berquó (2010), Quantifying the concentration of ferrimagnetic particles in sediments using rock magnetic methods, *Geochem. Geophys. Geosyst.*, *11*(8), doi:10.1029/2010GC003182.

Lefèvre, C. T., and D. A. Bazylinski (2013), Ecology, Diversity, and Evolution of Magnetotactic Bacteria, *Microbiol. Mol. Biol. Rev.*, *77*(3), 497–526, doi:10.1128/MMBR.00021-13.

Lippert, P. C., and J. C. Zachos (2007), A biogenic origin for anomalous fine-grained magnetic material at the Paleocene-Eocene boundary at Wilson Lake, New Jersey, *Paleoceanography*, *22*(4), doi:10.1029/2007PA001471.

Lourens, L. J., A. Sluijs, D. Kroon, J. C. Zachos, E. Thomas, U. Röhl, J. Bowles, and I. Raffi (2005), Astronomical pacing of late Palaeocene to early Eocene global warming events, *Nature*, *435*(7045), 1083–1087, doi:10.1038/nature03814.

Nicolo, M. J., G. R. Dickens, C. J. Hollis, and J. C. Zachos (2007), Multiple early Eocene hyperthermals: Their sedimentary expression on the New Zealand continental margin and in the deep sea, *Geology*, *35*(8), 699, doi:10.1130/G23648A.1.

Nilsson, A., Y.S. Lee, I. Snowball, M. Hill, (2013), Magnetostratigraphic importance of secondary chemical remanent magnetizations carried by greigite (Fe3S4) in Miocene sediments, New Jersey shelf (IODP Expedition 313). *Geosphere 9*, 510–520. doi:10.1130/GES00854.1

Nisbet, E. G., S. M. Jones, J. Maclennan, G. Eagles, J. Moed, N. Warwick, S. Bekki, P. Braesicke, J. A. Pyle, and C. M. R. Fowler (2009), Kick-starting ancient warming, *Nat. Geosci.*, *2*(3), 156–159, doi:10.1038/ngeo454.

Maclennan, J., and S. Jones (2006), Regional uplift, gas hydrate dissociation and the origins of the Paleocene–Eocene Thermal Maximum, *Earth Planet. Sci. Lett.*, *245*(1-2), 65–80, doi:10.1016/j.epsl.2006.01.069.

McCarren, H., E. Thomas, T. Hasegawa, U. Röhl, and J. C. Zachos (2008), Depth McCarren, H., E. Thomas, T. Hasegawa, U. Röhl, and J. C. Zachos (2008), Depth dependency of the Paleocene-Eocene carbon isotope excursion: Paired benthic and terrestrial biomarker records (Ocean Drilling Program Leg 208, Walvis Ridge), *Geochem. Geophys. Geosyst.*, *9*(10), doi:10.1029/2008GC002116.

Miller, K. G. (1997), Coastal plain drilling and the New Jersey sea-level transect,Proc. Ocean Drill. Program Sci. Results, 150X, 3 – 12.

Murphy, B. H., K. A. Farley, and J. C. Zachos (2010), An extraterrestrial 3He-based timescale for the Paleocene–Eocene thermal maximum (PETM) from Walvis Ridge, IODP Site 1266, *Geochim. Cosmochim. Acta*, *74*(17), 5098–5108, doi:10.1016/j.gca.2010.03.039.

Oda, H., M. Torii (2004), Sea-level change and remagnetization of continental shelf sediments off New Jersey (ODP Leg 174A): magnetite and greigite diagenesis. *Geophys. J. Int. 156*, 443–458. doi:10.1111/j.1365-246X.2004.02162.x

Pancost, R. D., D. S. Steart, L. Handley, M. E. Collinson, J. J. Hooker, A. C. Scott, N. V. Grassineau, and I. J. Glasspool (2007), Increased terrestrial methane cycling at the Palaeocene–Eocene thermal maximum, *Nature*, *449*(7160), 332–335, doi:10.1038/nature06012.

Peters, K. E., Waters, C. C., and Moldowan, J. M (2005), The Biomarker Guide: Biomarkers and Isotopes in Petroleum Systems and Earth History, 2nd ed. Cambridge University Press.

Poulton, S. W., and D. E. Canfield (2011), Ferruginous Conditions: A Dominant Feature of the Ocean through Earth's History, *Elements*, *7*(2), 107–112, doi:10.2113/gselements.7.2.107.

Reynolds,, R. L., D. S. Sweetkind, and Y. Axford (2001), An inexpensive magnetic mineral separator for fine grained sediment, *U.S. Geological Survey open-file report 01-281*, 7.

Rickard, D. Sulfidic sediments and sedimentary rocks, (2012), p. 272-275, Elsevier, Amsterdam, The Netherlands.

Röhl, U., T. Westerhold, T. J. Bralower, and J. C. Zachos (2007), On the duration of the Paleocene-Eocene thermal maximum (PETM): PALEOCENE-EOCENE THERMAL MAXIMUM, *Geochemistry, Geophysics, Geosystems*, *8*(12), doi:10.1029/2007GC001784.

Rowan, C. J., and A. P. Roberts (2006), Magnetite dissolution, diachronous greigite formation, and secondary magnetizations from pyrite oxidation: Unravelling complex magnetizations in Neogene marine sediments from New Zealand, *Earth Planet. Sci. Lett.*, *241*(1-2), 119–137, doi:10.1016/j.epsl.2005.10.017.

Schmitz, B., and V. Pujalte (2003), Sea-level, humidity, and land-erosion records across the initial Eocene thermal maximum from a continental-marine transect in northern Spain, *Geology*, *31*(8), 689, doi:10.1130/G19527.1.

Schumann, D. et al. (2008), Gigantism in unique biogenic magnetite at the Paleocene-Eocene Thermal Maximum, *Proc. Natl. Acad. Sci.*, *105*(46), 17648–17653, doi:10.1073/pnas.0803634105.

Scott, M. L. (2005), Mapping and characterization of the Marlboro clay formation, University of Maryland, College Park.

Shackleton, N. J. (1986), Paleogene stable isotope events, *Palaeogeogr. Palaeoclimatol. Palaeoecol.*, *57*(1), 91–102, doi:10.1016/0031-0182(86)90008-8.

Sluijs, A., H. Brinkhuis, S. Schouten, S. M. Bohaty, C. M. John, J. C. Zachos, G.-J. Reichart, J. S. Sinninghe Damsté, E. M. Crouch, and G. R. Dickens (2007), Environmental precursors to rapid light carbon injection at the Palaeocene/Eocene boundary, *Nature*, *450*(7173), 1218–1221, doi:10.1038/nature06400.

Stassen, P., E. Thomas, and R. P. Speijer (2012), The progression of environmental changes during the onset of the Paleocene-Eocene Thermal Maximum (New Jersey Coastal Plain), *Austrian J. Earth Sci.*, *105*(1), 169–178.

Stephenson, A., and L. Molyneux (1987), The rapid determination of rotational remanent magnetization and the effective field which produces it, *Geophys. J. R. astr. Soc.*, *90*, 467–471.

Stephenson, A., and I. F. Snowball (2001), A large gyromagnetic effect in greigite, *Geophys. J. Int.*, *145*(2), 570–575, doi:10.1046/j.0956-540x.2001.01434.x.

Storey, M., R. A. Duncan, and C. C. Swisher (2007), Paleocene-Eocene Thermal Maximum and the Opening of the Northeast Atlantic, *Science*, *316*(5824), 587–589, doi:10.1126/science.1135274.

Svensen, H., S. Planke, A. Malthe-Sørenssen, B. Jamtveit, R. Myklebust, T. Rasmussen Eidem, and S. S. Rey (2004), Release of methane from a volcanic basin as a mechanism for initial Eocene global warming, *Nature*, *429*(6991), 542–545, doi:10.1038/nature02566.

ten Haven, H. L. T., M. Rohmer, J. Rullkötter, and P. Bisseret (1989), Tetrahymanol, the most likely precursor of gammacerane, occurs ubiquitously in marine sediments, *Geochim. Cosmochim. Acta*, *53*(11), 3073–3079, doi:10.1016/0016-7037(89)90186-5.

Thomas, D. J., J. C. Zachos, T. J. Bralower, E. Thomas, and S. Bohaty (2002), Warming the fuel for the fire: Evidence for the thermal dissociation of methane hydrate during the Paleocene-Eocene thermal maximum, *Geology*, *30*(12), 1067, doi:10.1130/0091-7613(2002)030<1067:WTFFTF>2.0.CO;2.

Tribovillard, N., T. J. Algeo, T. Lyons, and A. Riboulleau (2006), Trace metals as paleoredox and paleoproductivity proxies: An update, *Chem. Geol.*, *232*(1-2), 12–32, doi:10.1016/j.chemgeo.2006.02.012.

Wang, H., D. V. Kent, and M. J. Jackson (2012), Evidence for abundant isolated magnetic nanoparticles at the Paleocene-Eocene boundary, *Proc. Natl. Acad. Sci.*, *110*(2), 425–430, doi:10.1073/pnas.1205308110.

Wijsman, J. W. ., J. J. Middelburg, P. M. . Herman, M. E. Böttcher, and C. H. . Heip (2001), Sulfur and iron speciation in surface sediments along the northwestern margin of the Black Sea, *Mar. Chem.*, *74*(4), 261–278, doi:10.1016/S0304-4203(01)00019-6.

Wright, J. D., and M. F. Schaller (2013), Evidence for a rapid release of carbon at the Paleocene-Eocene thermal maximum, *Proc. Natl. Acad. Sci.*, *110*(40), 15908–15913, doi:10.1073/pnas.1309188110.

Chapter 5

Outlook

Curiosity-driven and accidental discoveries of magnetotactic bacteria (MTB) in the 1960's (by S. Bellini) and 1970's (by R.P. Blakemore) initiated a generation of research on these awe-inspiring prokaryotes. These microorganisms perfected the art of locating their environmental niche of choice, typically near the oxic-anoxic interface (OAI) in aquatic settings. This behavior, called magnetotaxis (R. Blakemore, 1975), magnetosensitivity (S. Bellini, 2009a,b), or magneto-aerotaxis (Frankel et al. 1997), is made possible by the biologically-controlled synthesis of specialized organelles, termed magnetosomes, consisting of membrane-bound nanocrystals of magnetite (Fe_3O_4) and/or greigite (Fe_3S_4).

Once MTB die, magnetosomes can be preserved in the geological records provided that they escape the microbially mediated Fe^{3+} reduction and/or alteration by H_2S generated from SO_4^{2-} reduction. Motivations for determing the concentration of fossilized magnetosomes (or, magnetofossils) in geological specimens vary, ranging from establishing a linkage to paleoenvironmental conditions (e.g. Chang and Kirschvink, 1989; Hesse, 1994; Snowball et al., 2002; Egli 2004a,b; Kopp et al., 2007, 2009; Lippert and Zachos, 2007; Kodama et al., 2013; Lascu and Plank, 2013; Abrajevitch and Kodama, 2011; Roberts et al., 2011; Larrasoaña et al., 2012; Kind et al., 2012; Reinholdsson et al., 2013; Chang et al. 2014; R. G. Hatfield, 2014), assessing the carrier and fidelity of paleomagnetic signal (e.g. Schwartz et al., 1997; Housen and Moskowitz, 2006; Maloof et al., 2007; Roberts et al., 2012; Heslop et al., 2013; Mao et al., 2014; Larrasoaña et al., 2014), to establishing the presence of life in deep time on earth (e.g. Chang et al. 1989) and on Mars (McKay et al., 1996; Thomas-Keptra et al., 2000, Friedman et al., 2001, Weiss et al., 2004). Short of a time machine and convienent space exploration options, properties of modern MTB on earth provide the only guide for fingerprinting their existence in the past. Among the known diversity of MTB with remarkably different physiology, morphology, and phylogeny, a small subset of cultivable MTB strains spurred developments of magnetism-based magnetofossil detection methods in the past decade. While axenic cultures provide samples that readily meet instrument sensitivity, challenges in isolating and cultivating MTB found in nature meant that available cultured strains, as well as their magnetic characterization, severely underrepresent diverse MTB in nature. For example, unlike cultured and characterized magnetite magnetosomes arranged in simple linear chains, the only greigite-producing MTB recently cultivated in the laboratory, strain BW-1, biosynthesizes either single or double

chains of magnetite and/or greigite depending on hydrogen sulfide concentration and/or redox potential in the growth medium (Lefèvre et al., 2011). BW-1 represents just one of the two known greigite-producing MTB morphotypes and has never been characterized by any of the magnetofossil detection methods in use today. The work presented in Chapter 2 evaluates the applicability of existing methods for detecting generally uncultivated MTB inhabiting the water column of a stratified euxinic estuary. The ferromagnetic resonance results show that uncultivated MTB, consisting of at least seven morphopytes with diverse physiologies and magnetosome mineralogies, from the Pettaquamscutt River Estuary are characterized by a wider range of empirical spectral parameters compared to the five cultured magnetite-producing MTB strains (AMB-1, MS-1, MV-1, MC-1, MRS-1) that have been characterized by FMR to-date. These findings provide a new metric for magnetofossil identification based on FMR as well as new data for future modeling efforts.

Besides FMR, additional cases were made for culture-independent approaches to the magnetic characterization of MTB. Coercivity distribution measured from uncultivated MTB from Pettaquamscutt River Estuary (Chapter 2) and Little Sippewissett marsh (Chapter 3) show strong similarity to BS-BM, one of two magnetic components previously associated with magnetofossils (Egli, 2004a; Vasiliev et al., 2008; Maloof et al., 2007; Roberts et al., 2012; Kodama et al., 2013; Mao et al., 2014). This component came about originally from non-unique numerical inversion of magnetization curves measured from sediment samples with different provenances (Egli, 2004a). The coercivity distributions from uncultivated MTB therefore lend a strong independent support for the connection between BS-BM and magnetofossils. This magnetosome mineralogy-independent result was further invoked to elucidate the origin of the other proposed magnetofossil component, BH-BI. Having ruled out its specific association with greigite magnetosomes, elongated magnetosomes, diagenesis of magnetosomes, and/or framboidal greigite were instead hypothesized to give rise to BH-BI (Chapter 2). The set of uncultivated MTB also made it possible to investigate rotational and gyro-remanent magnetization, RRM and GRM, respectively. The discovery of a large effective gyrofield, rB_g, in a sediment sample containing clusters (framboids) of octahedral greigite (Stephenson and Snowball, 2001) prompted the usage of RRM and GRM as specific markers for framboidal greigite. However, what specific property of framboidal greigite promotes the acquisition of RRM and GRM remained a mystry. The first set of high rotation rate RRM measurements from uncultivated greigite MTB from the sulfidic hypolimnion in Pettaquamscutt River Estuary and Little Sippewissett marsh significantly advanced our understanding (Chapter 3). The results demonstrate that the greigite mineralogy alone does

not explain RRM and GRM acquisition, since greigite magnetosomes have a much smaller gyrofield than framboidal greigite (Chapter 3). Instead, the small gyrofield of magnetosome chain and chain bundles lend independent support to Potter and Stephenson's (2006) notion that the amount of RRM acquired depends on particle elongation (Chapter 3). In addition to not being in chains, framboidal greigite are under the influence of large dipolar interation (e.g. Roberts et al., 2011) and can have fewer crystallographic structural defects compared to magnetosomes (e.g. Pósfai et al., 2001), both of which were hypothesized to affect gyromagnetism (Chapter 3), though further investigation is warranted.

Insights obtained from the characterizations of modern uncultivated MTB was leveraged to better understand the Marlboro Clay at the New Jersey Coastal Plain dating to the Paleocene-Eocene boundary. The onset of highly magnetic clay coincides with a large negative carbon isotopic excursion (CIE), though the carrier of the magnetic signal was far from clear (Wang et al., 2012). Analyses presented in Chapter 4 revealed that while a component similar to BS-BM can account for between 22 to 37% of the anhysteretic remanent magnetization (ARM) for syn-CIE sediment, 54 to 63% can be accounted for by a component similar to BH-BI. Among the three sources (elongated magnetosomes, diagenesis of magnetosomes, and/or framboidal greigite) of BH-BI hypothesized in Chapter 2, framboidal greigite was favored in light of complimentary microscopy observations of abundant framboidal iron sulfide and gyrofield with intermediate values between magnetofossils (magnetosomes from uncultivated MTB have $0<rB_g<7.3$ μT, Chapter 3) and framboidal greigite (variable rB_g, though framboidal/cluster-bearing sediments have rB_g in the range of 77 μT (Hu et al., 2002) to ~1100 μT (Stephenson and Snowball, 2001). As illustrated by this example, an improved understanding of rB_g mixing behavior between different magnetic components is a promising way forward.

The geomicrobiology of MTB was investigated in the stratified euxinic Pettaquamscutt River Estuary with a focus on estimating the amount of MTB-associated Fe in the biogeochemical cycle. Various observations suggest MTB are involved in the cycling of carbon, nitrogen, sulfur, phosphorus, and iron in the aquatic environment they live in. Magnetospirillum strain AMB-1, for example, seems to be able to fix N_2, evident by acetylene reduction as well as N_2-dependent growth under microaerobic laboratory conditions (Bazylinski et al. 2000). Large elemental sulfur inclusions and phosphorus-rich inclusions have been found in magnetotactic cocci, with the former lending strong support for their ability to store S for use as electron donors (Cox et al. 2002). MTB can incorporate orders of magnitude more iron compared to non-MTB cells (Heyen and Schüler, 2003) as

well as being a sizable portion of the biomass (30%; Spring et al., 1993). The fate of magnetosome-Fe varies, ranging from ingestion and digestion by protozoans (Lin et al., 2013; Martin et al., 2007), dissolution with or without the involvement of iron-chelating siderophores MTB produce themselves (Simmons and Edwards, 2006; Canfield and Berner, 1987, Vali and Kirschvink, 1989), to incorporation into the sedimentary matrix. While the above processes are difficult to tease apart, the work presented in Chapter 2 gave an estimate of the balance between them. This was achieved by determining the MTB population turnover rate and the amount of MTB Fe exported out of the chemocline came out to be nearly half of the pyritic Fe flux in an open euxinic basin like the Black Sea (Chapter 2). Such estimate assumes a similar MTB cell density and dynamic in open euxinic basins, both of which should be further investigated.

There are numerous ways in which the study of MTB geomicrobiology can move forward. In addition to what have been mentioned above, two broadly related opportunities can be explored. The first is related to the search for MTB in deep time on earth especially at major atmospheric oxygen transitions, while the second concerns the development of new MTB detection methods. As reviewed recently by Lyon et al. (2014), available biogeochemical data paint a rich and complex history of oxygenation on Earth. As opposed to the classical two-step increases in atmospheric oxygen to its present day value, new data suggest O_2 production begun long before the Great Oxidation Event (GOE) as defined by the disappearance of non-mass-dependent sulfur isotope fractionations that took place between 2.4 to 2.3 Gyr ago (as reviewed and compiled in Lyon et al., 2014). Given that MTB are gradient organisms who prefer to live around the OAI (e.g. Chapter 2), could they have been present near photosynthetic cyanobacteria colonies, thought of as the earliest O_2 producers? Chang et al. (1989) looked for magnetofossils in two Archean stromatolite samples but did not find signs of magnetofossils. However, given the propensity of magnetofossil to undergo diagenesis (e.g. Chapter 2), perhaps more Archean samples can be analyzed or MTB markers other than magnetofossils can be developed and used. An argument could be made from recent advancements in our understanding of the genetic evolution of magnetotaxis that the oldest MTB record is yet to be found. Lefèvre et al. (2013) put forward an idea that bullet-shaped magnetite magnetosomes could be the most ancient magnetosome morphology by observing that such morphology is strongly linked to the most deeply branching phylogenetic MTB groups. On the other hand, the oldest putative magnetofossil dating to 2.0 Gyr found in a stromatolitic chert by Chang et al. (1989) is cuboidal in shape. Many opportunities also abound in the Proterozoic as biogeochemical data continues to modify and refine the

structure of the "Canfield Ocean", a proposed widespread euxinica in the deep ocean (Canfield, 1998). While the anoxia as proposed in the deep ocean is agreed upon in the Proterozoic atmosphere still depleted in O_2 compared to the present day value, ferruginous condition prevailed except for areas adjecent continental margin where the primary productivity is high (Lyons et al., 2004). An understanding of MTB ecology in stratified ferruginous settings may be helpful in defining the dynamic and areal extent of ferruginous versus euxinic conditions. In stark contrast to our increased knowledge on MTB geobiology in stratified euxinic settings (e.g. Chapter 2), the existence of MTB in stratified ferruginous aquatic environment that can serve as analog to early ferruginous ocean has not been investigated. Lastly, as highlighted by the differences in FMR empirical parameters between magnetosomes from cultivated and uncultivated MTB, a better detection method than what is currently available is desirable. This new method would ideally remove the imposition of the single-chain geometry, given the rich variety of non-single-chain magnetosome arrangements continuing to be uncovered (e.g. Chapter 2) and the artifact that can come from the magnetic extraction process. One possibility is to look for specific molecular fossils from cultivated and uncultivated MTB cells.

References

Abrajevitch, A., Kodama, K., 2011. Diagenetic sensitivity of paleoenvironmental proxies: A rock magnetic study of Australian continental margin sediments. Geochem. Geophys. Geosyst. 12. doi:10.1029/2010GC003481

Bazylinski, D.A., Dean, A.J., Schuler, D., Phillips, E.J.P., Lovley, D.R., 2000. N2-dependent growth and nitrogenase activity in the metal-metabolizing bacteria, Geobacter and Magnetospirillum species. Environ. Microb. 2, 266–273. doi:10.1046/j.1462-2920.2000.00096.x

Bellini, S., 2009a. On a unique behavior of freshwater bacteria. Chin. J. Oceanol. Limnol. 27, 3–5. doi:10.1007/s00343-009-0003-5

Bellini, S., 2009b. Further studies on "magnetosensitive bacteria." Chin. J. Oceanol. Limnol. 27, 6–12. doi:10.1007/s00343-009-0006-2

Blakemore, R., 1975. Magnetotactic bacteria. Science 190, 377–379. doi:10.1126/science.170679

Canfield, D.E., Berner, R.A., 1987. Dissolution and pyritization of magnetite in anoxie marine sediments. Geochimica et Cosmochimica Acta 51, 645–659. doi:10.1016/0016-7037(87)90076-7

Canfield, D.E., 1998. A new model for Proterozoic ocean chemistry. Nature 396, 450–453.

Chang, S.B.R., Kirschvink, J.L., 1989. Magnetofossils, the Magnetization of Sediments, and the Evolution of Magnetite Biomineralization. Ann. Rev. Earth Planet. Sci. 17, 169–195. doi:10.1146/annurev.ea.17.050189.001125

Chang, S.-B.R., Stolz, J.F., Kirschvink, J.L., Awramik, S.M., 1989. Biogenic magnetite in stromatolites. II. Occurrence in ancient sedimentary environments. Precambrian Res. 43, 305–315. doi:10.1016/0301-9268(89)90062-4

Chang, L., Vasiliev, I., van Baak, C., Krijgsman, W., Dekkers, M.J., Roberts, A.P., Gerald, J.D.F., van Hoesel, A., Winklhofer, M., 2014. Identification and environmental interpretation of diagenetic and biogenic greigite in sediments: A lesson from the Messinian Black Sea. Geochem. Geophys. Geosyst. 15, 3612–3627. doi:10.1002/2014GC005411

Cox, B.L., Popa, R., Bazylinski, D.A., Lanoil, B., Douglas, S., Belz, A., Engler, D.L., Nealson, K.H., 2002. Organization and Elemental Analysis of P-, S-, and Fe-rich Inclusions in a Population of Freshwater Magnetococci. Geomicrobl. J. 19, 387–406. doi:10.1080/01490450290098504

Egli, R., 2004a. Characterization of Individual Rock Magnetic Components by Analysis of Remanence Curves, 1. Unmixing Natural Sediments. Stud. Geophys. Geod. 48, 391–446. doi:10.1023/B:SGEG.0000020839.45304.6d

Egli, R., 2004b. Characterization of individual rock magnetic components by analysis of remanence curves. 3. Bacterial magnetite and natural processes in lakes. Phys. Chem. Earth 29, 869–884. doi:10.1016/j.pce.2004.03.010

Farquhar, J., Bao, H., Thiemens, M., 2000. Atmospheric Influence of Earth's Earliest Sulfur Cycle. Science 289, 756–758. doi:10.1126/science.289.5480.756

Frankel, R.B., Bazylinski, D.A., Johnson, M.S., Taylor, B.L., 1997. Magneto-aerotaxis in marine, coccoid bacteria. Biophys. J. 73, 994–1000.

Friedmann, E.I., Wierzchos, J., Ascaso, C., Winklhofer, M., 2001. Chains of magnetite crystals in the meteorite ALH84001: Evidence of biological origin. Proc. Natl. Acad. Sci. USA. 98, 2176–2181. doi:10.1073/pnas.051514698

Hatfield, R., 2014. Particle Size-Specific Magnetic Measurements as a Tool for Enhancing Our Understanding of the Bulk Magnetic Properties of Sediments. Minerals 4, 758–787. doi:10.3390/min4040758

Heslop, D., Roberts, A.P., Chang, L., Davies, M., Abrajevitch, A., De Deckker, P., 2013. Quantifying magnetite magnetofossil contributions to sedimentary magnetizations. Earth Planet. Sci. Lett. 382, 58–65. doi:10.1016/j.epsl.2013.09.011

Hesse, P.P., 1994. Evidence for bacterial palaeoecological origin of mineral magnetic cycles in oxic and sub-oxic Tasman Sea sediments. Mar. Geol. 117, 1–17. doi:10.1016/0025-3227(94)90003-5

Heyen, U., Schüler, D., 2003. Growth and magnetosome formation by microaerophilic Magnetospirillum strains in an oxygen-controlled fermentor. Appl. Biochem. Biotechnol. 61, 536–544. doi:10.1007/s00253-002-1219-x

Housen, B.A., Moskowitz, B.M., 2006. Depth distribution of magnetofossils in near-surface sediments from the Blake/Bahama Outer Ridge, western North Atlantic Ocean, determined by low-temperature magnetism. J. Geophys. Res. 111. doi:10.1029/2005JG000068

Hu, S., Stephenson, A., Appel, E., 2002. A study of gyroremanent magnetisation (GRM) and rotational remanent magnetisation (RRM) carried by greigite from lake sediments. Geophys. J. Int. 151, 469–474. doi:10.1046/j.1365-246X.2002.01793.x

Kind, J., Raden, U.J. van, García-Rubio, I., Gehring, A.U., 2012. Rock magnetic techniques complemented by ferromagnetic resonance spectroscopy to analyse a sediment record. Geophys. J. Int. 191, 51–63. doi:10.1111/j.1365-246X.2012.05620.x

Kodama, K.P., Moeller, R.E., Bazylinski, D.A., Kopp, R.E., Chen, A.P., 2013. The mineral magnetic record of magnetofossils in recent lake sediments of Lake Ely, PA. Global. Planet. Change. doi:10.1016/j.gloplacha.2013.03.012

Kopp, R.E., Raub, T.D., Schumann, D., Vali, H., Smirnov, A.V., Kirschvink, J.L., 2007. Magnetofossil spike during the Paleocene-Eocene thermal maximum: Ferromagnetic resonance, rock magnetic, and electron microscopy evidence from Ancora, New Jersey, United States. Paleoceanography 22, doi:10.1029/2007PA001473

Kopp, R.E., Schumann, D., Raub, T.D., Powars, D.S., Godfrey, L.V., Swanson-Hysell, N.L., Maloof, A.C., Vali, H., 2009. An Appalachian Amazon? Magnetofossil evidence for the development of a tropical river-like system in the mid-Atlantic United States during the Paleocene-Eocene thermal maximum. Paleoceanography 24, doi:10.1029/2009PA001783

Larrasoaña, J.C., Roberts, A.P., Chang, L., Schellenberg, S.A., Fitz Gerald, J.D., Norris, R.D., Zachos, J.C., 2012. Magnetotactic bacterial response to Antarctic dust supply during the Palaeocene–Eocene thermal maximum. Earth Planet. Sci. Lett. 333-334, 122–133. doi:10.1016/j.epsl.2012.04.003

Larrasoaña, J.C., Liu, Q., Hu, P., Roberts, A.P., Mata, P., Civis, J., Sierro, F.J., PÃ©rez-Asensio, J.N., 2014. Paleomagnetic and paleoenvironmental implications of magnetofossil occurrences in late Miocene marine sediments from the Guadalquivir Basin, SW Spain. Front. Microbiol. 5. doi:10.3389/fmicb.2014.00071

Lascu, I., Plank, C., 2013. A new dimension to sediment magnetism: Charting the spatial variability of magnetic properties across lake basins. Global. Planet. Change 110, 340–349. doi:10.1016/j.gloplacha.2013.03.013

Lefèvre, C.T., Menguy, N., Abreu, F., Lins, U., Posfai, M., Prozorov, T., Pignol, D., Frankel, R.B., Bazylinski, D.A., 2011. A Cultured Greigite-Producing Magnetotactic Bacterium in a Novel Group of Sulfate-Reducing Bacteria. Science 334, 1720–1723. doi:10.1126/science.1212596

Lefèvre, C.T., Trubitsyn, D., Abreu, F., Kolinko, S., de Almeida, L.G.P., de Vasconcelos, A.T.R., Lins, U., Schüler, D., Ginet, N., Pignol, D., Bazylinski, D.A., 2013. Monophyletic origin of magnetotaxis and the first magnetosomes: Monophyletic origin of magnetotaxis. Environ. Microb. 15, 2267–2274. doi:10.1111/1462-2920.12097

Lin, W., Bazylinski, D.A., Xiao, T., Wu, L.-F., Pan, Y., 2013. Life with compass: diversity and biogeography of magnetotactic bacteria: Magnetotactic bacterial diversity and biogeography. Environ. Microb. doi:10.1111/1462-2920.12313

Lippert, P.C., Zachos, J.C., 2007. A biogenic origin for anomalous fine-grained magnetic material at the Paleocene-Eocene boundary at Wilson Lake, New Jersey. Paleoceanography 22. doi:10.1029/2007PA001471

Lyons, T.W., Reinhard, C.T., Planavsky, N.J., 2014. The rise of oxygen in Earth's early ocean and atmosphere. Nat. Rev. 506, 307–315. doi:10.1038/nature13068

Martins, J.L., Silveira, T.S., Abreu, F., Silva, K.T., da Silva-Neto, I.D., Lins, U., 2007. Grazing protozoa and magnetosome dissolution in magnetotactic bacteria. Environ. Microbiol. 9, 2775–2781. doi:10.1111/j.1462-2920.2007.01389.x

McKay, D.S., Gibson, E.K., Thomas-Keprta, K.L., Vali, H., Romanek, C.S., Clemett, S.J., Chillier, X.D.F., Maechling, C.R., Zare, R.N., 1996. Search for Past Life on Mars: Possible Relic Biogenic Activity in Martian Meteorite ALH84001. Science 273, 924–930. doi:10.1126/science.273.5277.924

Maloof, A.C., Kopp, R.E., Grotzinger, J.P., Fike, D.A., Bosak, T., Vali, H., Poussart, P.M., Weiss, B.P., Kirschvink, J.L., 2007. Sedimentary iron cycling and the origin and preservation of magnetization in platform carbonate muds, Andros Island, Bahamas. Earth Planet. Sci. Lett. 259, 581–598. doi:10.1016/j.epsl.2007.05.021

Mao, X., Egli, R., Petersen, N., Hanzlik, M., Zhao, X., 2014. Magnetotaxis and acquisition of detrital remanent magnetization by magnetotactic bacteria in natural sediment: First experimental results and theory: MAGETOTAXIS AND MAGNETOFOSSIL NRM. Geochemistry, Geophysics, Geosystems 15, 255–283. doi:10.1002/2013GC005034

Pósfai, M., Cziner, K., Márton, E., Márton, P., Buseck, P.R., Frankel, R.R.B., Bazylinski, D.A., 2001. Crystal-size distributions and possible biogenic origin of Fe sulfides. Eur. J. Mineral. 13, 691–703. doi:10.1127/0935-1221/2001/0013-0691

Potter, D.K., Stephenson, A., 2006. The stable orientations of the net magnetic moment within single-domain particles: Experimental evidence for a range of stable states and implications for rock magnetism and palaeomagnetism. Phys. Earth Planet. In. 154, 337–349. doi:10.1016/j.pepi.2005.06.018

Reinholdsson, M., Snowball, I., Zillén, L., Lenz, C., Conley, D.J., 2013. Magnetic enhancement of Baltic Sea sapropels by greigite magnetofossils. Earth Planet. Sci. Lett. 366, 137–150. doi:10.1016/j.epsl.2013.01.029

Roberts, A.P., Florindo, F., Villa, G., Chang, L., Jovane, L., Bohaty, S.M., Larrasoaña, J.C., Heslop, D., Fitz Gerald, J.D., 2011. Magnetotactic bacterial abundance in pelagic marine environments is limited by organic carbon flux and availability of dissolved iron. Earth Planet. Sci. Lett. 310, 441–452. doi:10.1016/j.epsl.2011.08.011

Roberts, A.P., Chang, L., Rowan, C.J., Horng, C.-S., Florindo, F., 2011. Magnetic properties of sedimentary greigite (Fe_3S_4): An update. Rev. Geophys. 49. doi:10.1029/2010RG000336

Roberts, A.P., Chang, L., Heslop, D., Florindo, F., Larrasoaña, J.C., 2012. Searching for single domain magnetite in the "pseudo-single-domain" sedimentary haystack: Implications of biogenic magnetite preservation for sediment magnetism and relative paleointensity determinations. J. Geophys. Res. 117. doi:10.1029/2012JB009412

Schwartz, M., Lund, S.P., Hammond, D.E., Schwartz, R., Wong, K., 1997. Early sediment diagenesis on the Blake/Bahama Outer Ridge, North Atlantic Ocean, and its effects on sediment magnetism. J. Geophys. Res. 102, 7903. doi:10.1029/96JB03218

Simmons, S.L., Edwards, K.J., n.d. Geobiology of Magnetotactic Bacteria, 2006. in: Schüler, D. (Ed.), Magnetoreception and Magnetosomes in Bacteria. Springer Berlin Heidelberg, pp. 77–102.

Snowball, I., Zillén, L., Sandgren, P., 2002. Bacterial magnetite in Swedish varved lake-sediments: a potential bio-marker of environmental change. Quatern. Int. 88, 13–19. doi:10.1016/S1040-6182(01)00069-6

Spring, S., Amann, R., Ludwig, W., Schleifer, K.-H., van Gemerden, H., Petersen, N., 1993. Dominating Role of an Unusual Magnetotactic Bacterium in the Microaerobic Zone of a Freshwater Sediment. Appl Environ Microbiol. 59, 2397–2403.

Stephenson, A., Snowball, I.F., 2001. A large gyromagnetic effect in greigite. Geophys. J. Int. 145, 570–575. doi:10.1046/j.0956-540x.2001.01434.x

Thomas-Keprta, K.L., Bazylinski, D.A., Kirschvink, J.L., Clemett, S.J., McKay, D.S., Wentworth, S.J., Vali, H., Gibson, E.K., Romanek, C.S., 2000. Elongated prismatic magnetite crystals in ALH84001 carbonate globules: Geochim. Cosmochim. Acta. 64, 4049–4081. doi:10.1016/S0016-7037(00)00481-6

Vali, H., Kirschvink, J.L., 1989. Magnetofossil dissolution in a palaeomagnetically unstable deep-sea sediment. Nature 339, 203–206. doi:10.1038/339203a0

Vasiliev, I., Franke, C., Meeldijk, J.D., Dekkers, M.J., Langereis, C.G., Krijgsman, W., 2008. Putative greigite magnetofossils from the Pliocene epoch. Nat. Geosci. 1, 782–786. doi:10.1038/ngeo335

Wang, H., Kent, D.V., Jackson, M.J., 2012. Evidence for abundant isolated magnetic nanoparticles at the Paleocene-Eocene boundary. Proc. Natl. Acad. Sci. 110, 425–430. doi:10.1073/pnas.1205308110

Weiss, B.P., Kim, S.S., Kirschvink, J.L., Kopp, R.E., Sankaran, M., Kobayashi, A., Komeili, A., 2004. Magnetic tests for magnetosome chains in Martian meteorite ALH84001. Proc. Natl. Acad. Sci. USA. 101, 8281–8284. doi:10.1073/pnas.0402292101